

Master Thesis in Reservoir Physics

**A Visual Study of CO₂ Injection at the Pore Scale
using Micromodels**



Nicolai-Ivar Majlaton

University of Bergen

Department of Physics and Technology

December 2012

Acknowledgment

First I would like to thank Prof. Arne Graue for the support, teachings and opportunity to take part in new research at the Department of Physics and Technology at the University of Bergen.

Next I would to thank Dr. Martin Fernø for the guidance and support during the process of working with and completing my thesis.

Thanks to my lab partner PhD. Jarand Gauteplass, for supporting me in the laboratory throughout countless hours of experimental work.

A special thanks to Håvard Nakken Follesø for the excellent work he did both before me and together with me. His work has been essential for my findings.

Thanks to all my fellow students for the discussions, laughs, sharing of knowledge, and for taking part on this journey.

Lastly, I would like to thank my family and all my friends for keeping me sane and supporting me throughout my studies. You all made it possible for me to succeed. A special thanks to my loving parents Maurice and Magni, for raising me and supporting me all my life.

Thank you all for your contribution

Nicolai-Ivar Majlaton

Summary

Increasing the oil recovery on the Norwegian Continental Shelf has been given much attention in later years, and CO₂ injection is a method with great potential for enhancing the recovery. The distinct advantage with CO₂ is that it achieves miscibility at relatively low pressures compared to other gas injection techniques for EOR[4]. The miscible CO₂ promotes oil swelling, increases the oil density, reduces the oil viscosity and increases the mobility. This thesis is the first at the Department of Physics and Technology where miscible oil/CO₂ is visualized at the pore scale by using micromodels. The experimental work includes fundamental two-phase processes of water imbibition, primary drainage, secondary water injection, and more advanced processes with three-phase CO₂ injection. The main objectives were to identify displacement mechanisms, study controlling forces including capillary and viscous forces, and study gaseous and liquid CO₂ injection at immiscible and miscible conditions.

Fluid displacements were visualized in low and high pressure silicon wafer micromodels at constant temperature and different pressure intervals. The micromodels were modelled after real Berea sandstones and manufactured with real rock properties. Visualizations were obtained through an inverted microscope, connected to a camera that enabled images to be captured and stored on the computer. Fluorescent additives mixed in the water and oil made it possible to distinguish between the fluids during multiple-phase flow by applying light filters to the microscope. Porosity, saturations and the recoveries were estimated using image software on the computer.

Two flow regimes were observed during two-phase flow; stable and unstable flow. Stable, capillary controlled flow was observed during water imbibition at low injection rates and low differential pressure (Δp), and during primary (oil/water) drainage at high injection rates and high Δp . Unstable, viscously controlled flow was observed at opposite flow conditions, represented by viscous fingering. Capillary forces controlled the displacement mechanisms at low pressures and injection rates, while the influence of viscous forces increased with increased rate. Unstable flow conditions developed during three-phase gas injection proportionally with the increase in differential pressure. Diffusion contributed to an improved CO₂ sweep in the fractured micromodels even after CO₂ breakthrough in the production port. Stable piston-like displacement, unstable piston displacement (Haines' jumps), double/multiple displacement, film flow of spreading oil layers, and snap-off events were observed during three-phase CO₂ gas injections.

CO₂ was observed to condensate into liquid at 61.4 bars \pm 0.5 bar. More favourable mobility ratios reduced the effect of viscous forces, and the diffusion increased with the increased pressure[5]. Miscibility events were observed at 82.0 bars \pm 0.5 bar. Oil swelling was observed to increase the volume of oil, and the miscible phase displaced fluids through piston and multiple displacement. During depressurization, vaporizing CO₂ and gas expansion from swelled oil were observed to displace oil through solution gas drive. High recoveries were achieved for both gaseous and liquid CO₂; however the production were observed to be more stable and efficient during liquid CO₂ injection.

Table of Contents

Acknowledgment	3
Summary	4
Table of Contents	5
Introduction	7
I. Theory	8
1. Fundamentals	8
1.1 Porosity	8
1.2 Absolut Permeability	9
1.3 Saturation	9
1.4 Capillary Pressure	10
1.5 Relative Permeability	13
1.6 Wettability	14
1.7 Mobility	15
1.8 Flow and Displacement at Pore Scale	16
1.9 Recovery Factor	17
2. Enhanced Oil Recovery and CO ₂	18
2.1 EOR	18
2.2 Gas Injection	18
2.3 Miscibility	19
2.4 CO ₂	20
II. Experimental Equipment and Procedures	21
3. Experimental Equipment	21
3.1 Experimental Setup and Equipment	21
3.2 Fluorescent	27
3.3 Micromodels	28
4. Experimental Procedure	31
4.1 Boundary Conditions	31

4.2 Water Imbibition and Water Filling	32
4.3 Permeability Measurements	32
4.4 Porosity and Saturation Measurements	33
4.5 Primary Drainage.....	34
4.6 CO ₂ Gas Injection.....	34
4.7 Liquid CO ₂ Injection	35
III. Results and Discussion.....	36
5. Low Pressure Silicon Wafer Micromodel.....	37
5.1 Porosity and Permeability.....	37
5.2 Spontaneous Imbibition.....	38
5.3 Primary Drainage.....	44
5.4 Secondary Water Injection	49
5.5 Three-Phase CO ₂ Gas Injection.....	50
5.6 Contact Angle Measurements.....	55
6. High Pressure Silicon Wafer Micromodels.....	56
6.1 Permeability and Porosity.....	56
6.2 Primary Drainage.....	58
6.3 Three-Phase CO ₂ Gas Injection.....	61
6.4 Three-Phase Liquid CO ₂ Injection	66
6.5 Experimental Challenges	76
6.6 Summarized Discussion CO ₂ Injection	78
IV. Conclusions and Future Work.....	81
7. Conclusions	81
8. Future Works.....	83
9. Notations	84
10. References	85
Appendix I – Uncertainty Estimations	87

Introduction

The peak of the worldwide oil production is closing in, some say we have already past it. The population is growing, and energy demands are increasing rapidly. As less new oilfields are discovered, and most of the “easy” oil has been produced[6], maximizing the recovery from existing fields has become more and more important.

Water injection has been the method of choose for increasing the oil recovery on the Norwegian Continental Shelf. The injected water provides pressure support to the reservoir and displaces the oil towards the production wells. On the NCS the estimated recoveries range between 15 and 65%, with an average of 44% of the STOIIP [7]. These estimates assume water injection as the main drive mechanism. The residual oil after waterflooding is then over 50% and gives a great potential for other, more effective EOR techniques [7].

One method for EOR that lately has received much attention is the injection of CO₂ for EOR. The environmental benefits during CO₂ injection could be great, as the injected CO₂ may be stored in the reservoir during and after oil production. Onshore fields in the US have provided an increase in recovery in the range of 7 to 15% form CO₂ injection [7]. Successfully implementing injection of CO₂ on the NCS could result in an increase in revenue for Norway and the operating oil companies, and also help met the increasing energy demands.

Before implementing CO₂ injection, a series of simulations, calculations, test and experiments must be conducted to predict and fully understand the CO₂-water/oil displacement mechanisms. Knowledge of the displacement mechanisms in the reservoir is obtained from experiments conducted on core samples in the laboratory. The results provide a good understanding of the displacement and the forces present on the laboratory scale, where the flow to a large degree is controlled by capillary forces when using small core plugs, whereas displacement on the field scale is determined by viscous forces. Although oil displacement on the field scale is controlled by viscous forces, displacement within each pore, where the liquid is located, is controlled by capillary forces. To fully understand CO₂ injection at the field scale, it is therefore necessary to also study the displacement at the pore scale.

Micromodels provide the opportunity to study flow mechanisms visually on the pore scale. Realistic, 2D properties are etched in silicon wafers, based on thin sections of the reservoir rocks, and closed by transparent glass plates. During experiments the displacement is viewed through an inverted microscope, and images are captured by a camera to visualize the flow mechanisms. Flow is mainly controlled by capillary forces, and by understanding the flow on a pore scale, and combining results from both experiments on core samples and micromodels, the production process can be optimized, resulting in an increase in the total recovery of oil.

In this thesis, displacement is studied on the pore scale using micromodels. Basic properties for the models are calculated, and displacement is studied for water injection and for both liquid and gaseous CO₂ injection at different pressure intervals. These experiments are fundamental for understanding the displacement when using CO₂ as a method of Enhanced Oil Recovery.

I. Theory

Fundamental properties in reservoir physics are presented in the first chapter; from porosity and permeability to displacement mechanisms. The second chapter include a short introduction of EOR, and basic properties of CO₂ injection and miscibility.

1. Fundamentals

1.1 Porosity

Reservoir rocks contain cemented mineral grains of different size and shape, with cavities and pores. The volume of these pores determines the porosity of the rock. The porosity is given by equation 1.1, where V_p is the pore volume, V_t the total volume of the rock and φ the porosity:

$$\varphi = \frac{V_p}{V_t} \quad (1.1)$$

The porosity is one of the most important properties, because it provides an estimate of the oil volume present in reservoirs. In reservoir engineering we are interested in the connected pores. For the oil to initially migrate and later be displaced, a connected pathway is essential. The porosity is therefore divided in to residual (φ_{res}) and effective porosity (φ_{eff}). **Figure 1.1** gives an illustration of the different porosities, and distinguishes between catenary (open), Cul-de-sac- and closed pores.

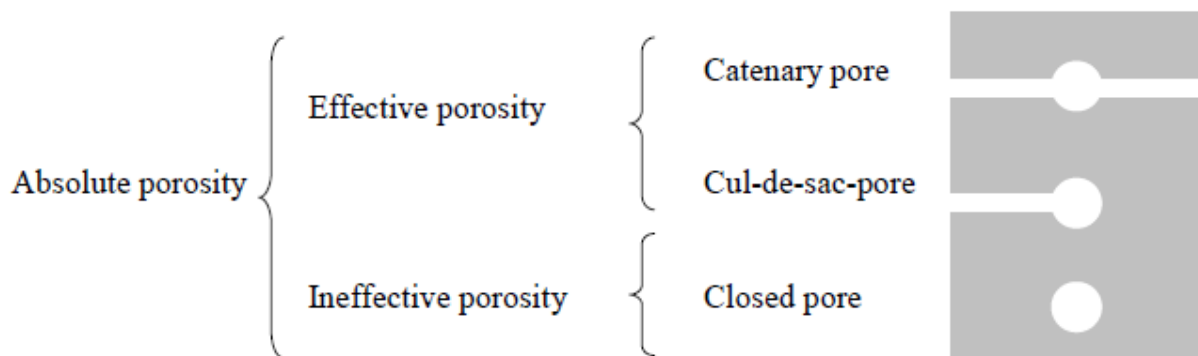


Figure 1.1 – Three different kinds of pores representing ineffective and effective porosity[8]

The volume of the fluids given by the effective porosity is the producible volume. The residual porosity is the volume of non-connected pores. The porosity is usually measured in the laboratory, using core samples from the reservoir. On the pore scale porosity measurements are obtained from image analyses (chapter 4.4).

1.2 Absolut Permeability

The absolute permeability (K) is a measure of the rocks capability to conduct fluid flow through the connected pores given by the effective porosity[9]. The absolute permeability is calculated using Darcy's law given by equation 1.2. The equation shows that the fluid flow is proportional to the pressure difference[10].

$$q = \frac{KA \Delta p}{\mu L} \quad (1.2)$$

From the equation we have the fluid flow rate (q), the absolute permeability (K), the cross section area (A), the pressure difference (Δp), the viscosity of the fluid (μ) and the length of the medium (L). By measuring the pressure drop, while injecting a fluid through a porous medium, we are able to calculate the absolute permeability. For these calculations to be valid, the following criteria must be satisfied when conducting the experiment:

- Laminar flow
- 100% saturated with on fluid
- Horizontal flow
- Incompressible fluid
- No chemical reactions between the fluid and the rock

1.3 Saturation

Consider a reservoir that is partially saturated with each of the fluid phases; oil, water and gas. The saturation is the fraction of the reservoirs pore volume, which each fluid occupies. We divide the saturations in to S_o , S_w , and S_g , for oil, water and gas respectively. The sum of these fractions is equal to 1. The saturation for each fraction is given by equation 1.3, where S_i is the saturation for fluid i , V_i the volume of fluid i and V_p the total pore volume:

$$S_i \stackrel{\text{def}}{=} \frac{V_i}{V_p}, i = 1, \dots, n \quad (1.3)$$

The irreducible water saturation (S_{iw}) is the lowest possible value for the water saturation (see Figure 1.4.2). Water is capillary trapped in the smaller pores, and in water-wet reservoirs the water will lay as a film on the pore wall. The water saturation in a reservoir affects the relative permeability and sweep. High water saturation will cause the water to film flow along the pore wall and trap discontinuous oil, leading to a poor sweep. Two mechanisms may then occur, pore-doublet or snap-off. Pore doublet is when the water passes the oil phase, and snap-off is when the film flowing increases and traps the oil (see chapter 1.8.1).

1.4 Capillary Pressure

The capillary pressure is defined as the difference in pressure across the interface between two immiscible fluids[9]. The interface between the fluids will be curved if one of the fluids is more wetting, and the fluids are then divided into a wetting and non-wetting phase. The molecular pressure of the wetting (P_w) and the non-wetting (P_{nw}) phase, gives the capillary pressure (P_c) from equation 1.4.1:

$$P_c = P_{nw} - P_w \quad (1.4.1)$$

In **Figure 1.4.1** a drop of water is surrounded by oil, with the interfacial tension causing the circular form. The capillary pressure is then given by equation 1.4.2:

$$P_c = p_w - p_o = \frac{2\sigma}{r} \quad (1.4.2)$$

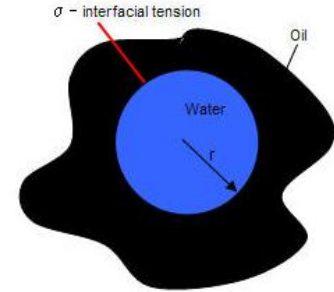


Figure 1.4.1: Interfacial tension for a drop of water in oil

On a lab scale we can calculate the capillary pressure, by confining two fluids in a cylinder, measuring the interfacial tension, and applying the result to equation 1.4.3:

$$P_c = \frac{2\sigma \cos \theta}{r} \quad (1.4.3)$$

where σ is the interfacial tension between the fluids, θ is the wetting-angle and r is the radius of the cylinder.

The capillary pressure is commonly plotted against the saturation of the wetting phase. During a primary drainage process the pressure and the saturation of the non-wetting fluid increases, while the capillary pressure increases. For an imbibition process the saturation for the wetting fluid will increase and the capillary pressure decrease. **Figure 1.4.2** displays a capillary pressure curve plotted against the saturation of water (wetting) and oil (non-wetting) for an imbibition and a primary drainage process.

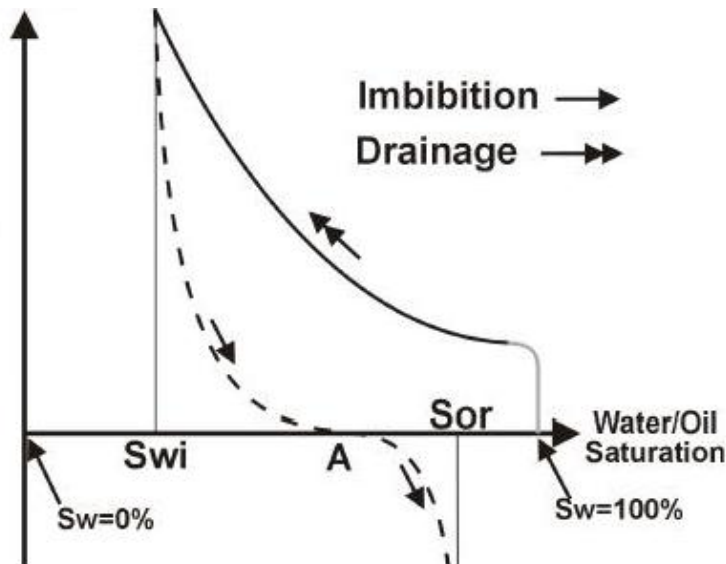


Figure 1.4.2: Capillary pressure curve for a drainage and imbibition process[11] with water saturation as a function of capillary pressure

The shape of the curve depends on fluid properties and both the pore size and size distribution. In addition the permeability will affect the shape of the curve. Low permeability is caused by the good packed grains and narrow pore throats. This will result in a higher capillary pressure, thereby giving us a connection between pore size and capillary pressure. From Figure 1.4.2 it is observed that the initial capillary pressure is high for an imbibition process and low for a drainage process. During an imbibition process the wetting phase enters the smaller pores and most narrow pore throats first, while the non-wetting phase enters the largest pores first during a drainage process. For a fluid to displace another fluid in a pore, the phase pressure has to be increased to be equal to the capillary pressure (see equation 1.4.1). The “entry” pressure needed to enter a pore is referred to as the threshold pressure. The threshold pressure increases as the diameter of the pore throats are reduced. During a drainage process the initial phase pressure of the non-wetting phase will be low thereby limiting flow to larger pores where the capillary pressure is low. As the phase pressure increases with the increased saturation the flow of the non-wetting phase will enter smaller pores and pore throats. This will be reversed during an imbibition process, where the wetting phase first will enter smaller pores when the capillary pressure is high, and enter larger pores as the capillary pressure decreases.

On the microscopic scale capillary forces will be dominating, while viscous forces will be more dominating on a larger scale. Capillary pressure is defined at the pore scale by Laplace’s law, stating that capillary pressure is a function of surface tension, contact angle and curvature[12].

1.4.1 Capillary Number

The capillary number is the ratio between the capillary and viscous forces. Studies have shown a correlation between the capillary number and the residual oil saturation[13]. The capillary forces vary according to the interfacial tension, while the viscous forces are affected by the differential pressure and the permeability. Equation 1.4.4 is an equation for the capillary number, where v and μ is the velocity and viscosity of the displacing fluid, σ is the interfacial tension between the fluids and θ is the contact angle.

$$N_c = \frac{\text{viscous forces}}{\text{capillary forces}} = \frac{v\mu}{\sigma \cos\theta} \quad (1.4.4)$$

High values for the capillary number indicates that the viscous forces are high compared to the interfacial tension and vice versa. During oil production a high capillary number is preferable as lower residual oil saturation is obtained. Reducing the interfacial tension can be done by injecting a fluid that is miscible with the oil. This will increase the microscopic displacement. The capillary number is often displayed as a function of the oil saturation (Figure 1.4.3).

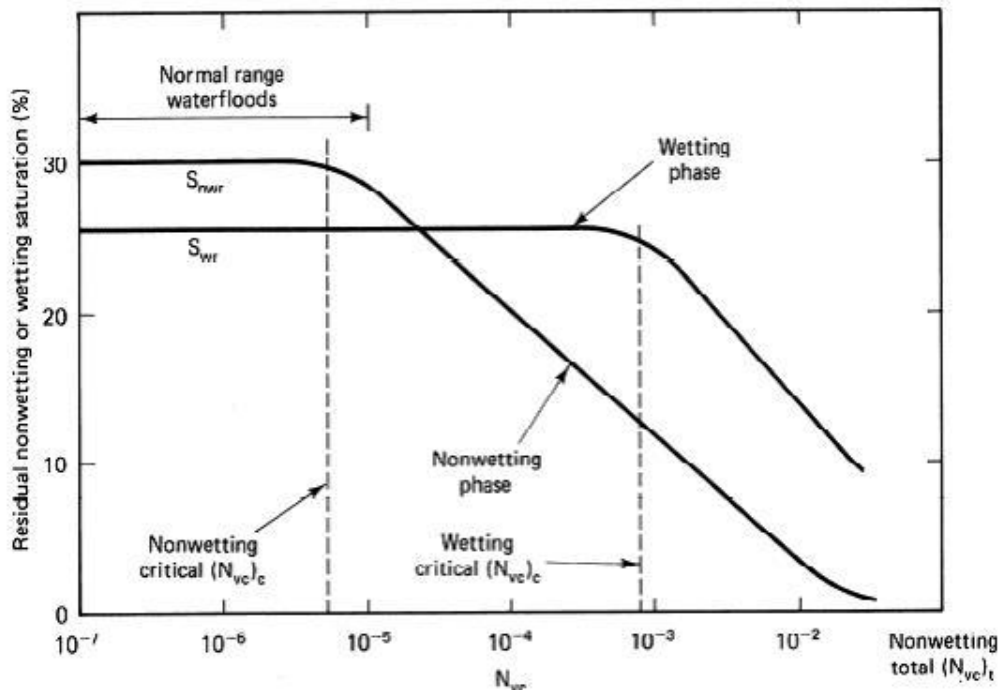


Figure 1.4.3: The capillary number as a function of the residual non-wetting or wetting saturation[13]

From the Figure 1.4.3 the saturation is observed to change after the critical capillary number is reached. After the critical value is reached the residual non-wetting saturation is reduced. Increasing the capillary number is therefore of great importance when the goal is to increase the total recovery.

1.4.2 Haines' Jump

Haines' jump is an interfacial instability studied by and named after William Haines. It occurs when there exist an unstable interface between two fluids, and a rapid change in capillary pressure causes a jump. During a drainage process this happens when a stable interface, becomes unstable by a curved pore geometry and the local capillary pressure is rapidly reduced [14]. During an imbibition process Haines' jump occur when an increased capillary pressure affect an unstable interface. The instability makes the interface jump until a stable interface is achieved and the fluids are redistributed. Haines' jump is similar to a piston-like displacement (see section 1.8.1), where a sharp interface completely displaces a fluid. The main difference is that a Haines' jump is a spontaneous mechanism and therefore irreversible[15]. Haines' jump was observed as a displacement mechanism on the pore scale during the experiments on the micromodels, and contributed to increased displacement efficiency.

1.5 Relative Permeability

The relative permeability describes each fluid's permeability when more than one immiscible fluid is present. Equation 1.5 describes the relative permeability for phase i :

$$k_{rel} = \frac{k_{effi}}{K} \quad , \quad i = w, o, g \quad (1.5)$$

From the equation the relative permeability for phase i , is given by the ratio between the effective permeability to phase i , and the absolute permeability to the porous medium. The value is in the range between 0 and 1, and depends on the fluids saturation, pressure, temperature, and fluid and rock properties. The relative permeability is normally plotted against saturation (**Figure 1.5**), and the highest saturation value gives the maximum relative permeability value. This point is defined as end-point relative permeability.

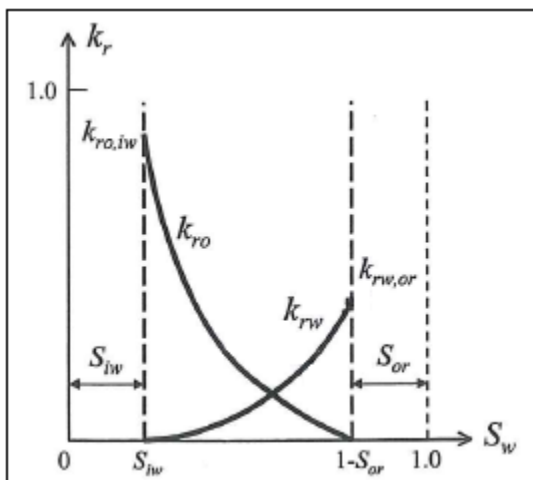


Figure 1.5: Two-phase relative permeability for oil and water plotted as a function of water saturation[16].

From Figure 1.5 the relative permeability is observed to change as the saturation changes. The endpoints are at the residual oil saturation (S_{or}) and at the irreducible water saturation (S_{iw}). At S_{iw} no more water is displaced and only oil is flowing, indicated by a high relative permeability value for oil and a relative permeability value of zero for water. The relative permeability values are opposite at S_{or} as no more oil is being displaced.

1.6 Wettability

Wettability is defined as the tendency a fluid has to spread on the surface of the grains, when another immiscible fluid is present[17]. There will exist a cohesive force between the fluids molecules and the molecules of the surface, where the fluid with the greatest cohesive force will be the wetting phase. If a reservoir is water-wet, the water will spread along the surface of the grains. The wettability of a reservoir has an effect on properties like capillary pressure, relative permeability, dispersion and the reservoirs capability to be water flooded. There are three methods for measuring the wettability; contact angle measurements, the USBM method and the Amott-Harvey method.

1.6.1 Contact Angle Measurement

The contact angle method is the most accurate method for wettability measurements. Measurements are done by measuring the contact angle between the fluid and the surface. This angle is called the wetting angle, and its value gives us the wettability. A surface is consider water-wet when the wetting angle is in the range of 0-90°, oil-wet in the range of 90-180°, and neutral when 90°. Close to 0° indicates a strongly water-wet surface, while close to 180° gives a strongly oil-wet surface. In reality the range between 75-105° is considered intermediate wet, where the surface has no strong cohesive preference to either water or oil.

1.6.2 USBM Method

The USBM method is used to calculate the average wettability, by looking at the work required to displace a volume of oil during a forced imbibition process. During this process a negative capillary pressure is obtained while the water saturation increases. By combining the area above the forced imbibition curve with the area under the drainage curve, a method of wettability calculations can be utilized[18]. Equation 1.6.2 gives the USBM index (W):

$$W = \log\left(\frac{A_1}{A_2}\right) \quad (1.6.2)$$

where A_1 is the area under the drainage curve and over the x-axis, and A_2 the area over the forced imbibition curve and under the x-axis. The index of the USBM index determines the wettability. A positive index indicates a water-wet surface, and a negative index an oil-wet surface.

1.6.3 Amott-Harvey Method

The Amott-Harvey method measures the average wettability during imbibition process on a core sample[19]. During primary drainage the water is displaced until irreducible water saturation (S_{iw}) is reached. The core sample is placed in an imbibition cell with water, and the volume of expelled oil is measured over time. The same experiment is done for oil. Equation 1.6.3 gives the Amott-Harvey index (I):

$$I = \left(\frac{V_{os}}{V_{ot}} \right) - \left(\frac{V_{ws}}{V_{wt}} \right) \quad (1.6.3)$$

where V_{os} is the volume of oil displaced spontaneously and V_{ot} the total volume of displaced oil, and similar for the spontaneously (V_{ws}) and total volume(V_{wt}) of water displaced. The range of the Amott-Harvey index is between -1 and 1, where -1 is strongly oil-wet and 1 strongly water-wet. All the methods for wettability estimation are summarized in Table 1.6

Table 1.6: Methods and the classification values for wettability

Wettability	Contact Angle[θ]	USBM	Amott-Harvey Index [I]
Water-wet	0-90°	+	0,3-1
Neutral	90°	0	-0,6
Oil-wet	90-180°	-	-0,7

At the pore scale contact angle measurements are the ideal method for determining the wettability. The visualization of the interface between two fluids enables the wetting angle to be measured.

1.7 Mobility

Mobility is a parameter that describes how one phase flows in a multiphase flow[20]. The phase with the greatest mobility will be more mobile and dominate the flow. The mobility is the ratio of the phase relative permeability and its viscosity, as seen from equation 1.7.1:

$$\lambda_i = \frac{k_i}{\mu_i} \quad (1.7.1)$$

where λ_i is the mobility of phase i , k_i is the relative permeability and μ_i the fluid viscosity. The mobility ratio M , is a ratio between the mobility of two immiscible phases (oil and water), as can be seen from equation 1.7.2:

$$M = \frac{\lambda_w}{\lambda_o} = \frac{k_{rw} \mu_o}{k_{ro} \mu_w} \quad (1.7.2)$$

End-point relative permeabilities are often used when calculating the mobility ratio, and then called M^0 . A mobility ratio equal to or less than one is ideal[20], providing a piston like displacement (Figure 1.8.1). Ideal mobility ratio between oil and water can be achieved by reducing the relative permeability of the water, increase the viscosity of water or decrease the oil viscosity. Water is often used as the injection fluid and the most commonly mobility ratio during waterflood in reservoirs is usually in the range of 0.02-2.00[21]. Gas has a much lower viscosity than water and the mobility is therefore higher. This can cause an unstable front when using gas as the injection fluid in a reservoir. Fingering can occur when fluids with higher mobility displace fluids with lower mobility.

1.8 Flow and Displacement at Pore Scale

The purpose of studying flow at the pore scale is to describe and interpret flow at reservoir scale. Up scaling is the main challenge when attempting to correlate between pore level and reservoir level. With micromodels the scale is approximately 10^{-6} m, while core and blocks at lab scale are in the range of 10^{-1} - 10^1 m. Typical oil reservoir is in the range of 10^3 - 10^5 m, and laws and forces dominating at pore scale might only have a small effect on the reservoir scale. When up scaling properties are averaged over REV, a representative elementary volume[22]. The pore network therefore has to be within the range of REV to fit the scaling requirements.

Using micromodels, pattern of flow and displacement can be studied at the pore scale by using an inverted microscope. The microscope provides an excellent tool for visualizing flow and displacement at the pore scale. Pore scale events are observed, and relations between pore scale and larger scale events can be drawn. Viscous forces will contribute to displacement on a large scale, while on the pore scale the capillary forces will be dominating. Visually the viscous fingering will be seen in the direction of the flow and pressure drop, while the capillary fingering will be developed normal to the direction of flow.

The micromodels and equipment used in this thesis is described in chapter 3. Micromodels can be used to visualize flow for most displacement process in reservoir engineering. Experiment conducted in this thesis include: spontaneous imbibition, primary drainage, secondary water injection and secondary CO₂ injection both liquid and gaseous.

1.8.1 Displacement Mechanisms

During the experiments displacement mechanisms were studied and identified. The advancing interface between the fluids was studied to determine the type of displacement. Piston-like displacement is consider being the ideal displacement in oil production, and is displayed in **Figure 1.8.1c**. During a drainage process the non-wetting phase displace the wetting phase with a piston-shaped front (thereby the name). The front advances in a stable manner as the phase pressure increases towards the capillary pressure (chapter 1.4). The displacement is reversed during an imbibition process. In a water/oil system the water displaces most of the oil, where only the immobile residual oil (S_{or}) is passed by the stable water front.

During a Haines' jump (chapter 1.4.2) the interface between two fluids jumps from a stable condition to an unstable condition before stabilizing again. Haines' jump is considered to be similar to piston displacement and is distinguished by the sudden unstable, advancing front and being irreversible. Double or multiple displacements are caused by several piston events, where a fluid phase displaces a fluid which in turn displaces another fluid. In **Figure 1.8.1a** a double displacement in a three-phase system with oil, water and gas is displayed. Snap off is displayed in **Figure 1.8.1b**. The wetting phase on the pore wall swells and separates two pores filled with the non-wetting phase, leading to a discontinuous non-wetting phase.

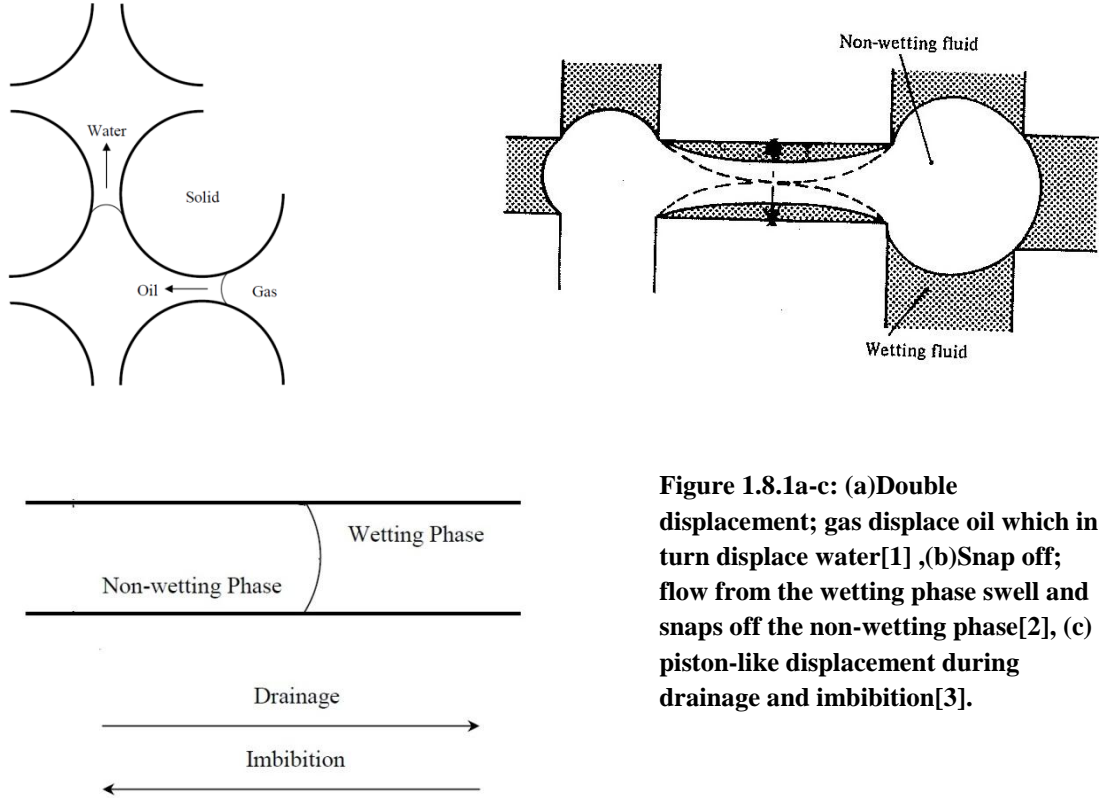


Figure 1.8.1a-c: (a) Double displacement; gas displace oil which in turn displace water [1], (b) Snap off; flow from the wetting phase swell and snaps off the non-wetting phase [2], (c) piston-like displacement during drainage and imbibition [3].

1.9 Recovery Factor

The recovery factor (E_R) is a measure of the fraction of oil produced from the total oil reserve. Equation 1.9 gives the recovery factor:

$$E_R = \frac{N_p}{N} \tag{1.9}$$

where N_p is the produced oil and N the total reserve. Increasing the recovery is the main focus on the Norwegian Continental Shelf today, and EOR techniques are used to improve the oil recovery.

2. Enhanced Oil Recovery and CO₂

2.1 EOR

Enhanced Oil Recovery (*EOR*) is a term often used for oil production during tertiary recovery. Another definition is oil recovery by the injection of materials not normally present in the reservoir[20]. Injection of CO₂ and water alternating gas (WAG) are not covered by this definition, but are still considered as EOR methods. The average recovery on the Norwegian Continental Shelf is as mention in the introduction, 44% of STOOIP. The remaining oil is the target for enhanced oil recovery projects. High oil prices influence the oil companies to invest more in research and development, and some methods that previously was consider too expensive, might be cost-efficient given today's marked.

The main targets for EOR are to improve both the volumetric and the microscopic displacement efficiency. Improving the volumetric displacement efficiency can be achieved with mobility control. By either increasing or decreasing the viscosity of one of the fluids, ideal mobility ratios close to 1 can be obtained. Increasing the microscopic displacement efficiency targets the capillary trapped oil. By reducing the interfacial tension between the displacing and displaced fluid, the capillary trapped oil can be produced. EOR consist of difference technologies, and are often divided into; chemical flooding, biological (MIOR-Microbial Improver Oil Recovery), thermal, and gas injection. In this thesis CO₂ gas and liquid CO₂ injection will be studied at the pore scale.

2.2 Gas Injection

Injection of gas is a commonly used EOR method. The injection provides pressure maintenance to the reservoir and can improve the sweep, thereby contribute to a higher oil recovery. Experiments based on hydrocarbon gas-displacement in Oseberg core samples at reservoir conditions, have produced residual oil saturations of approximately 10% [23]. Gas injection is commonly used in production and is one of the oldest injection processes in oil production. The gases normally used are Nitrogen, CO₂ and a range of Hydrocarbon gases. Gas injection is divided into two subcategories, immiscible and miscible gas injection. Immiscible gas injection is mostly used for pressure support, but might also increase the capillary number so more favourable mobility ratios can be achieved. Injected CO₂ can be both miscible and immiscible.

2.3 Miscibility

The molecules in a solution are driven by electrostatic forces, and if two different molecules are attracted to each other by a force stronger than between two similar molecules, miscibility is made possible[10]. In the oil industry miscible flooding is one of the most promising enhanced oil recovery methods due to its potential for recovering all the oil flushed by a solvent[4]. Miscible displacement improves the oil recovery by the following mechanisms; swelling of the oil phase, displacing oil with miscible solvent (reducing the interfacial tension and achieving a high capillary number), and reducing the viscosity of the oil[24].

To achieve miscibility the gas must be injected at or above minimum miscibility pressure (MMP). The MMP is the lowest pressure at which first- or multiple contact miscibility can be achieved[25]. In the oil industry the miscible processes are divided in to four subcategories: vaporizing gas drive, CO₂ flooding, condensing gas drive and first contact miscibility processes. In this thesis CO₂ flooding is studied both as an immiscible and a miscible process. A ternary diagram (**Figure 2.3**) is often used to explain miscibility.

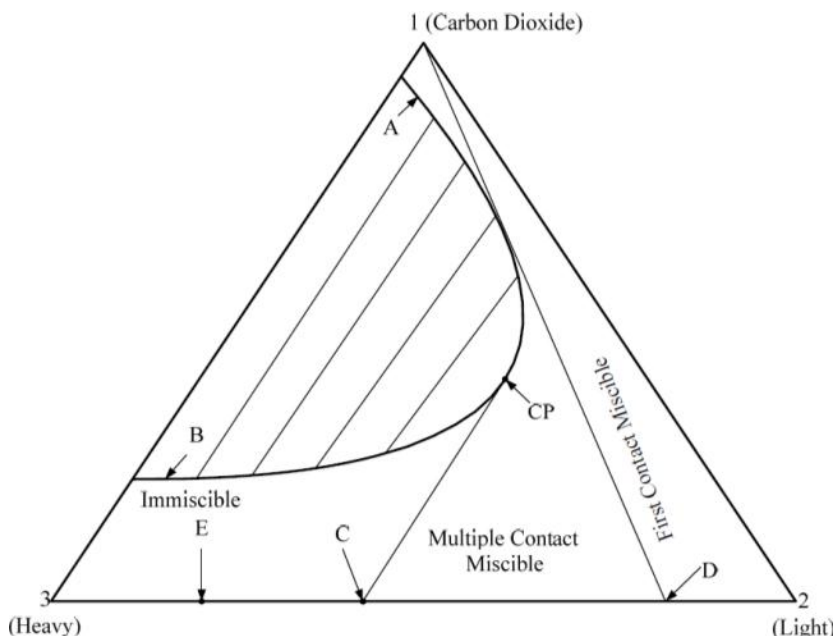


Figure 2.3: Ternary Diagram CO₂ and Oil [26]

Figure 2.3 is a ternary diagram for CO₂ and oil, where pure CO₂ is on the top corner(1), and heavy and light oil components in respectively the left(3) and right(2) corner. The striped area represents the two-phase region. The oil composition will determine if the oil is immiscible, multiple or first contact miscible with CO₂. If the oil and CO₂ is multiple contact miscible, they will be immiscible at first contact and later establish miscibility. In addition miscibility is controlled by pressure and temperature, and the two-phase area will shrink with increased pressure. This means that a process can be immiscible at first, and then evolve miscibility as the pressure is increased.

2.4 CO₂

Carbon dioxide is an atmospheric gas and is daily used in multiple processes, from the photosynthetic process to the food industry. CO₂ is mostly a bi-product of combustion, and the increasing worldwide pollution has made capture and storage of CO₂ a topic of interest. The petroleum industry is interested in CO₂ both for increasing the oil recovery and capturing for storage and/or use. CO₂ can be in solid, gas and liquid state, depending on the combination of pressure and temperature. **Figure 2.4** is a phase diagram, displaying how the state of CO₂ is connected to temperature and pressure.

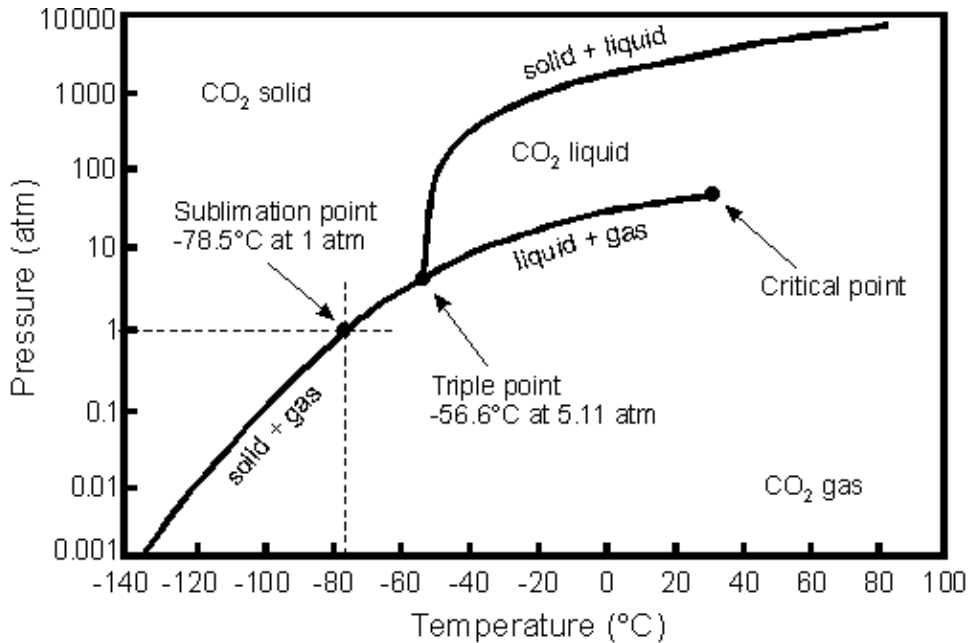


Figure 2.4: CO₂ Phase diagram[27] displaying areas for solid, liquid and gas phase as a function of pressure and temperature

The lines represent equilibrium between two phases, and they meet in a triple point where all the three phases are in equilibrium. With temperatures and pressures higher than the critical point, the CO₂ is supercritical. Supercritical CO₂ is both gaseous and liquid, where it is not possible to distinguish between the two phases. The density is equal to liquid CO₂ and the viscosity is similar to the viscosity of gaseous CO₂. Immiscible CO₂ increases the oil recovery by reducing the oil viscosity and swells the oil. This can result in improved recovery as trapped, residual oil can be mobilized. In a miscible displacement multi contact miscibility is achieved, and intermediate and heavier oil components are extracted. The CO₂ will cause the oil to swell, reduce the viscosity of the oil and increase the density of the oil, as the oils becomes saturated with CO₂ at increased pressure[4]. CO₂ is beneficial compared to other gases due to the low MMP. In this thesis CO₂ is used both in gaseous and in liquid state. Gaseous CO₂ is used in the low pressure silicon wafer micromodels while both liquid and gaseous CO₂ is injected in the high pressure micromodels.

II. Experimental Equipment and Procedures

The experiments conducted in this thesis include experiments on both low pressure and high pressure silicon wafer micromodel. The experimental setups for the two types of micromodels are displayed in chapter 3.1, and the experimental equipment is described in detail from section 3.3.1 to 3.3.2. Water imbibition, primary drainage and three-phase CO₂ experiments were conducted on the micromodels. The experimental procedure and calculation methods are described in detail in chapter 4.

3. Experimental Equipment

3.1 Experimental Setup and Equipment

Figure 3.1a shows the experimental setup used for the experiments on the low pressure silicon wafer micromodels. The low pressure micromodels were placed in a micromodel holder and connected to syringe pumps or to a CO₂-tank. The connection was made with tubings from the micromodel holder, and secured with Swagelok. The flow lines were connected to pressure transducers to measure differential- and gauge pressure. The micromodel holder was placed on an inverted microscope. The microscope was connected to a light source and a camera. Lastly the camera was connected to a computer, where image software allowed us to study the fluid displacement through time-lapse images.

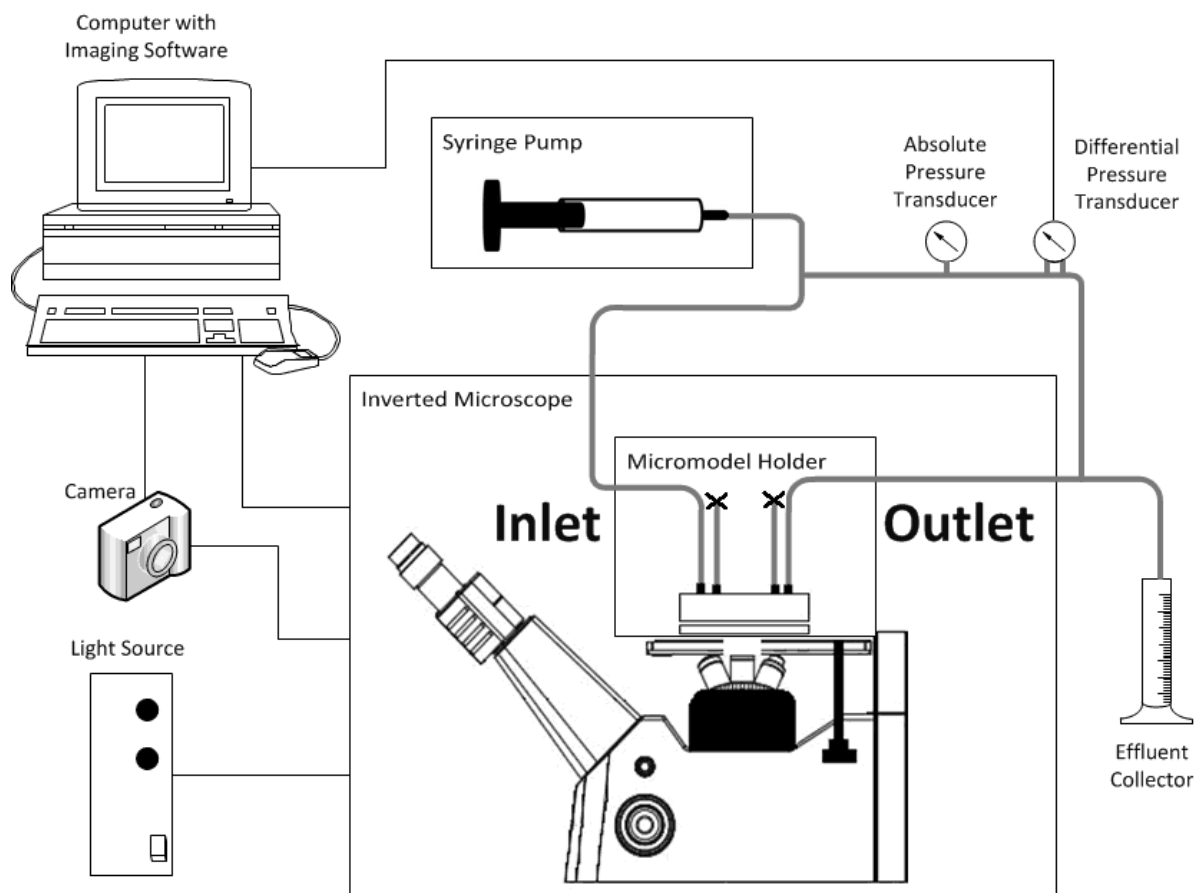


Figure 3.1a: Experiment setup for experiments with low pressure micromodels[28]

For the experiments on the high pressure silicon wafer micromodels, the setup from Figure 3.1a was altered. The syringe pump was substituted with a Quizix SP-5200 pump system, equipped with two pump cylinders. The pump system was connected to the PC, and pressure measurements were sent directly from the pump to the software on the computer. For the experiments with high pressure micromodels a different micromodel holder was used, specially designed for the high pressure micromodels. During the water saturation and drainage process the twin cylinder pump injected fluid at a constant rate through the inlet and fluids were produced through the outlet.

During the experiments with three-phase liquid and gaseous CO₂ on the high pressure micromodels, both the inlet and the outlet ports on the micromodel were connected to the twin cylinder pump system. Cylinder A was connected to a CO₂ tank and the inlet port on the micromodel, while cylinder B was connected to the outlet port on one side and closed on the other side. The entire setup is displayed in **Figure 3.1b**. The CO₂ tank delivered a pressure of 50bars. Calculation indicates liquid CO₂ state at pressures above 61.44bars at 23 °C[29]. The CO₂ tank was connected to Quizix QX-1500 twin cylinder pump to increase the pressure towards liquid conditions. Water was injected from the QX pump and into the CO₂ tank and the pressure increased over time as fluids were produced and accumulated in cylinder B.

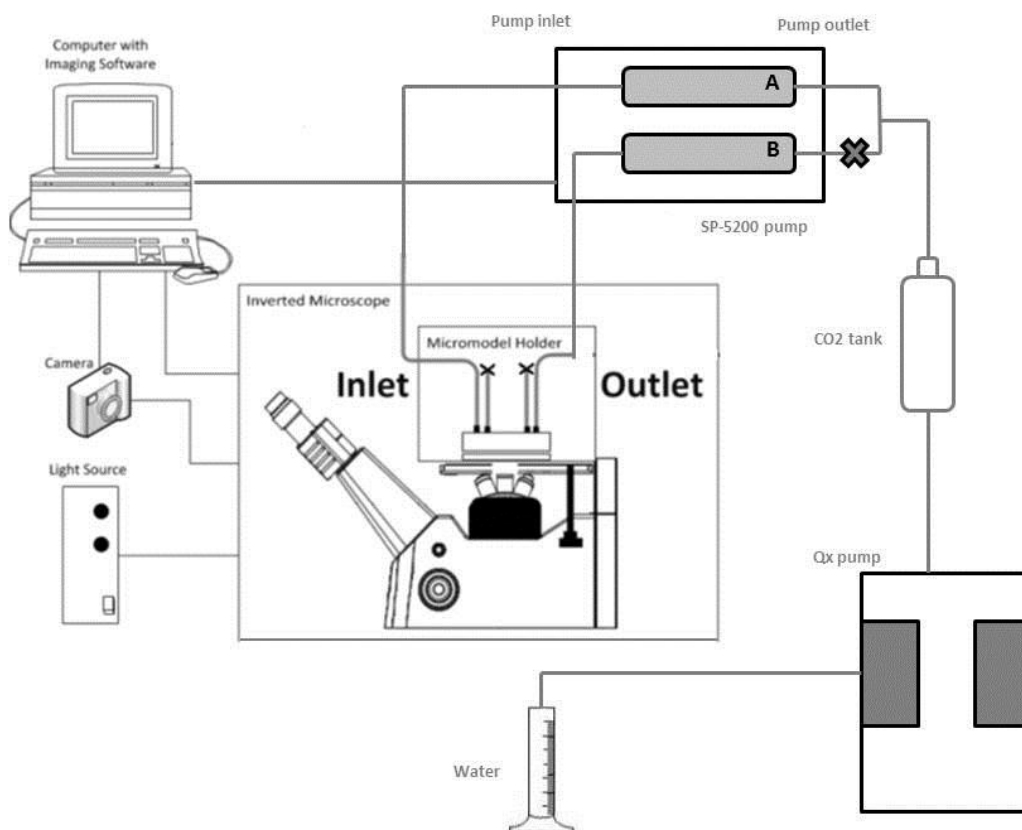


Figure 3.1b: Experimental setup for three-phase CO₂ injection for the high pressure micromodels

3.1.1 Micromodel Holders

Two types of micromodel holders were used during the experimental part of this thesis. High pressure micromodel with a customized micromodel holder produced by Micronite Microfluidics[30] were used for experiments above 2bars. Low pressure experiments below 2bars were performed in low pressure micromodels with an in-house holder designed and manufactured at the Department of Physics and Technology at University of Bergen. **Figure 3.1.1a and b** shows the two micromodel holders.



Figure 3.1.1a & b: (a) Micromodel holder for the high pressure micromodel (b) micromodel holder for the low pressure micromodels

The high pressure micromodel holder (Figure 3.1.1a) was produced in stainless steel with 8 ports for 1/16 inch tubings to be fitted (depending on the type of micromodel you have). For the experiments in this thesis 4 ports with tubings were used, 2 inlet and 2 outlet. The holder was designed for the micromodel in a polymer cartridge to be slide in and viewed in the microscope through the “window” in the holder. The specifications given by the factory permits pressure up to 100 bars and temperatures in the range of 50-80°, depending on the micromodel used[30].

The low pressure micromodel holder (Figure 3.1.1b) has two plates, one made by aluminium and the other by Plexiglas. The models was placed in-between the two plates, and then the plates were fasten to each other. The holder has 4 ports, 2 for injection and 2 for production, with fitted tubings. O-rings were used between the tubing and hole to ensure no leakage.

3.1.2 Pressure Transducers

For the experiments on the low pressure micromodels, two different types of pressure transducers were used; two gauge transducer separated by their range of measurement. The first one could measure up to 2 bars with an uncertainty of 0.02 bars, and the second one up to 15 bars with an uncertainty of 0.015 bars. The second pressure transducer was also used for differential pressure measurements. The transducer was connected to a digital interface board, which further was connected to the computer, where the pressures were logged. For the experiments with the high pressure micromodel the pump had built-in pressure transducers, directly connected to the computer.

3.1.3 Low Pressure Syringe Pumps

Two types of syringe pumps were used during the experiments on the low pressure micromodels, a Nexus 3000 KR Analytical syringe pump(**Figure 3.1.3a**) and a Pharmacia LKB P-500 pump(**Figure 3.1.3b**). The Pharmacia pump has a minimum injection rate of 1 ml/h, and is equipped with two syringes making continuous injection possible. The Nexus pump had to be manually refilled, and was mainly used for injection rates below 1 ml/h.



Figure 3.1.3a & 3.1.3b: Two syringe pumps; (a) Nexus 3000 KR Analytical and (b) Pharmacia LKB P-500

3.1.4 High Pressure Pump

The liquid CO₂ experiments required higher pressures and injection rates than the syringe pumps described in section 3.1.3 could deliver. A Quizix SP-5200 pump system was used for these experiments. The pump system was connected to and operated by the computer. The pumps features include the following: injection of fluids at high pressure and rates, precise built-in measurement equipment, allows high temperatures (160°C), logging and controls through Quizix Pump Works©, and the pump system could be operated at either constant pressure or constant rate[31]. For the experiments with liquid CO₂ a Quizix QX-1500 pump system was used in addition to the SP-pump. The QX pump system has two cylinders with a large volumes (49.0mL) compared to the SP-pump (9.3mL), and is able to deliver a higher rate of injection (12.0L/h for QX and 0.9 L/h for SP). Both pumps were operated with Pump Works. The QX pump was used to pressurize an additional CO₂ tank with water, to achieve a greater pressure increase. **Figure 3.1.4a & b** are images taken of the SP-5200 pump and the QX-1500 pump.

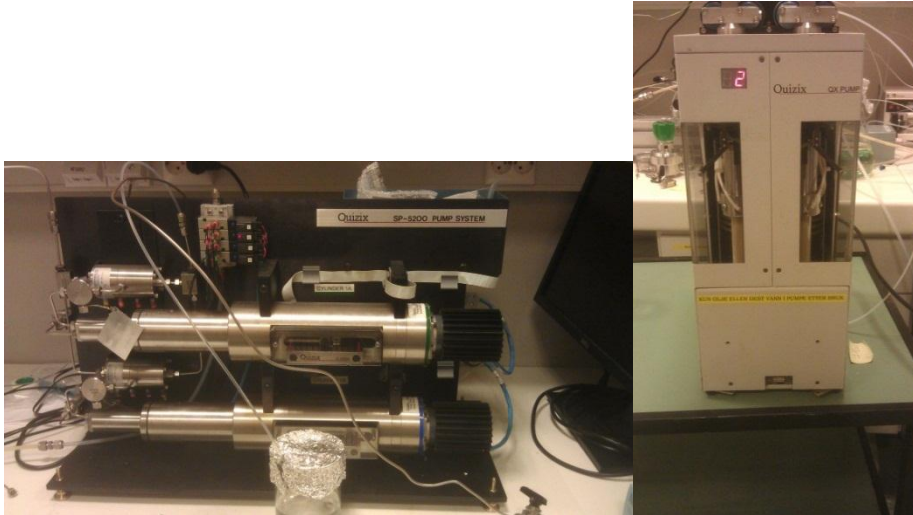


Figure 3.1.4a & 3.1.4b: Quizix Sp-5200 pump system and Quizix QX-1500 pump system

3.1.5 Nikon Eclipse TI-FI Inverted Microscope and External Light Source

Visualizations of the fluid flow in both the high and low pressure micromodels were enabled by using an inverted microscope. A Nikon Eclipse TI-FI Inverted Microscope was used throughout the experimental part of this thesis, and allowed equipment and the holders to be placed above the objective lens, instead of below as with a regular microscope. The microscope was equipped with 4 different objective lenses with different magnifications. In addition the microscope has a built-in zoom of 1.5X. The additional objective lenses enabled magnification of 2X, 5X, 10X and 20X zoom. An external light source was used to deliver light to the microscope through an optical cable.

The external light source was a Nikon Intensilight, and enabled a broad spectrum of light with different intensities and wavelengths to be used in the visualization process. The light source had 6 levels of intensities, which was adjusted depending on the magnification and fluids used. High intensities were required at low magnifications, while high magnifications and usage of Fluorescence required less intensive light. The ability to alter the intensities of light from the light source is crucial when working with Fluorescence.

3.1.6 Camera and Software

A Nikon Digital Sight DS-Fi1 high-definition colour camera was connected to the inverted microscope, and used to capture images of the flow during the experiments. The camera was a 5 megapixel CDC camera, and could captures images up to 2560 x 1920 pixels[32].

Operating the camera required a connection to a computer, with Nikon NIS-Elements imaging software installed on it. The software enabled capturing time-laps images, captured at a rate of one frame per second. Capturing images during the experiments allow further analyses of flow and displacement to be conducted at a later time.

3.1.7 Fluorescence Filters

Viewing the different Fluorescence mixed at different concentrations in both water and oil, required special Fluorescence filters to be mounted on the inverted microscope. The different Fluorescence filters adjusted the wavelength of the light from the external light source, in a matter that allowed only the fluid of interest to be visualized. Fluorescence reflects light at different wavelengths and by combining different light filters and Fluorescence, distinguishing between the different fluids during the experiments was possible. A bright light filter came with the microscope, and two additional filters were installed. The additional filters were labelled as blue and green, since the colour of the light were change to the respective colours when passing through the filters. The oil phase reflected red light from the green light filter and yellow light from the blue filter, while the water reflected green light from the blue filter.

The entire setup for the experiments with low pressure micromodels is displayed in **Figure 3.1.7**.

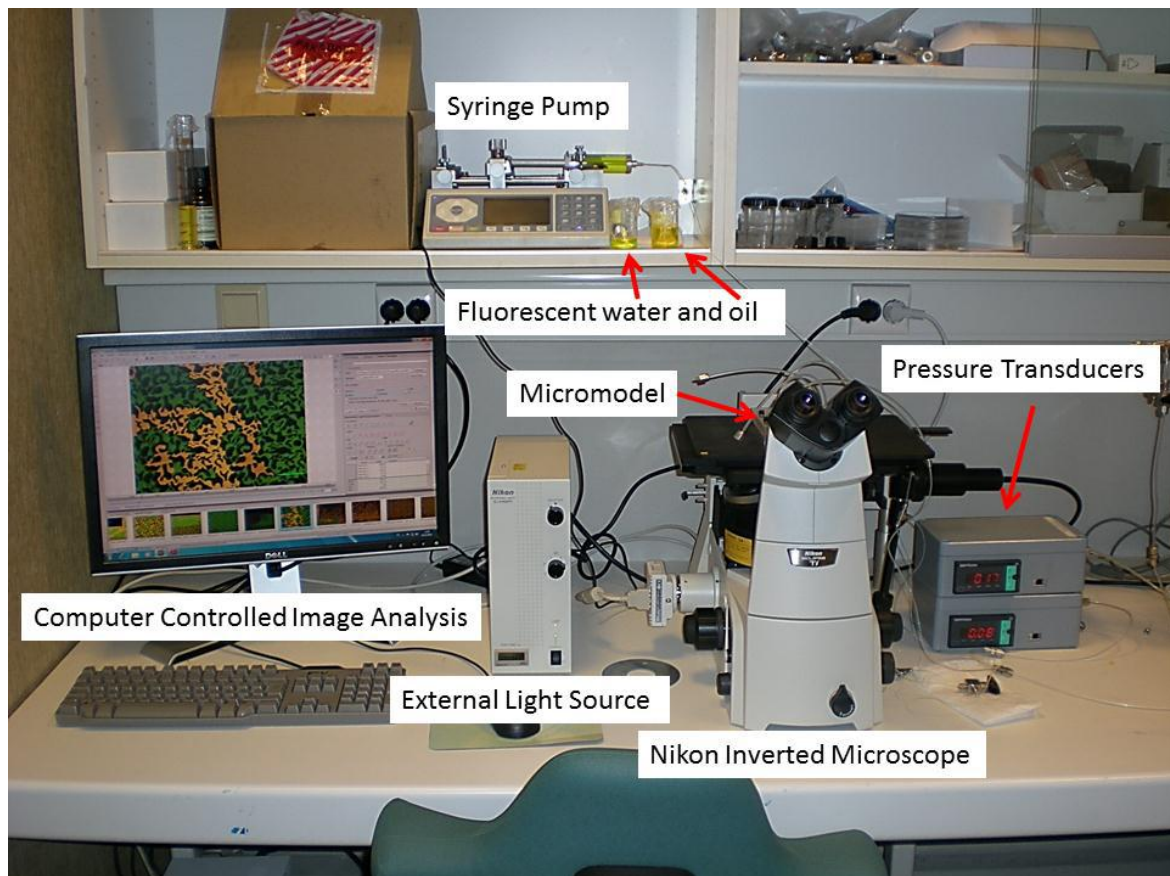


Figure 3.1.7: Photo of laboratory setup for experiments with micromodels[28]

3.2 Fluorescent

During the experimental part of this thesis distilled water, oil (n-decane), air and CO₂ were applied to the models. For the experiments with low pressure micromodels CO₂ was in gaseous state, while for the experiments with the high pressure micromodel CO₂ were in both liquid and gaseous state. The main reason for using micromodels is to visualize flow and displacement at pore scale. Being able to distinguish between the different fluids is therefore of great importance. Fluorescents additives were mixed with the oil and water, and made visualization with both 2- and 3-phase flow possible. Distilled water was mixed with either Fluorescein or FT175, while the oil was mixed with Nile Red.

3.2.1 Fluorescein

Fluorescein was mixed with the distilled water, and made it easy to distinguish the water from the other fluids. The blue filter on the Nikon Eclipse Microscope was used for viewing water with Fluorescein, and gave the phase a bright green colour. The Fluorescein is originally a powder that is soluble in both water and alcohol. Fluorescein is visible in concentrations down to 0.005ppm, and the intensity of the solution increases with increasing concentrations [33].

Photo bleaching and retentions are the main disadvantages when using Fluorescein. High concentrations made retention of Fluorescein accumulate on pore walls and in pore throats. The accumulated Fluorescein could only be removed when injecting CO₂ gas into the model. Photo bleaching made the visualization time limited, when studying a model with Fluorescein. The intensity of the colour and visibility, faded when the models were exposed to illumination over a period of time. Experiments have shown that the ideal mixing ratio of Fluorescein and water was 1:800 000[28]. At this ratio photo bleaching and retention were limited.

3.2.2 FT175

FT175 is a tracer used in water and is produced by the American Gas and Chemical Company. As with Fluorescein the FT175 appear green when view through the blue filter on the microscope. The F175 used in these experiments had an unknown concentration. The ideal mixing ratio was tested out with basic rubber-like micromodels (PDMS-Polydimethylsiloxane). Preliminary experiments proved that a solution with FT175 and water was less affected by photo bleaching compared to Fluorescein. During initially primary drainage experiments it was discovered that the FT175 accumulated in water. It was suspected that the accumulation affected the interfacial tension [28]. This accumulation restricted the use of FT175, and Fluorescein was used for most of the experiments with oil where flow and displacement was studied.

3.2.3 Nile Red

For the oil (n-decane) Nile Red was used as the Fluorescent additive. When viewed through the green filter on the microscope, the oil phase appeared with an intense, red colour. Nile Red is soluble in organic solvents and can vary in colours depending on the concentration, the solvent used, and the intensity of the light [34]. During the experiments the Nile Red and oil solution could be viewed with both the green and blue light filter. The blue filter gave the solution a yellow/brownish colour. During experiment with oil and water, the blue filter was the preferable filter, since both phases visually could be distinguished. **Figure 3.2.3** displays an image taken through the blue filter, where the black colour represents the matrix, and the pore is filled with oil (brown/orange) and water (green).

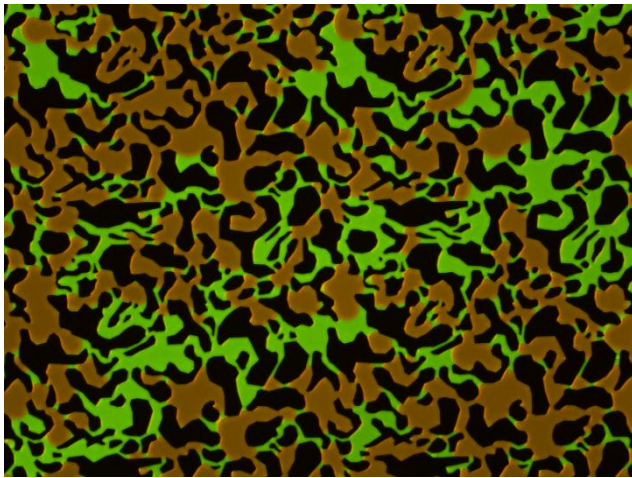


Figure 3.2.3: Oil and water with Nile Red and Fluorescein in a micromodel

3.3 Micromodels

For the experimental part of this thesis two different micromodels were used; low pressure silicon wafer micromodels and high pressure silicon wafer micromodels. The low pressure micromodels were used for the first experimental part (chapter 5), and for the second part (chapter 6) the high pressure micromodels were used. Both models had a pore network modelled after Berea sandstone, providing a realistic tool for visualization of displacement in an actual reservoir rock.

3.3.1 Low Pressure Silicon Wafer Micromodels

The low pressure micromodels were dry etched in silicon wafer, and fabricated at Stanford University in California. The pore network was modelled after a magnified 2D image of Berea sandstone thin sections. Based on the image, the pore network was dry etched in silicon wafer, and all flow paths were made continuous. After constructing the pore network, the silicon wafer was enclosed and anodic bounded with a transparent glass plate.

The construction was developed by Hornbrook[35], and his recipe was used at Stanford University when manufacturing the models. The scale of the network was 1:1 compared with the pore network of typical Berea sandstone, with grains in the range of 50-250 μm (see **Figure 3.3.1a**). The models were constructed with an idealized sandstone pattern, where the grains were rounded and all the pores continuous. The Department of Physics at University of Bergen received 8 models constructed by the University of Stanford. The model were named Berea A to H, where model B-H were designed after the original recipe. Model A were based on a new design with an improved pore design and a more details. Both designs had a repeating pattern of 500 x 500 μm , and had a total of 600 x 600 pores in a 5 x 5 cm square (**Figure 3.3.1b**).

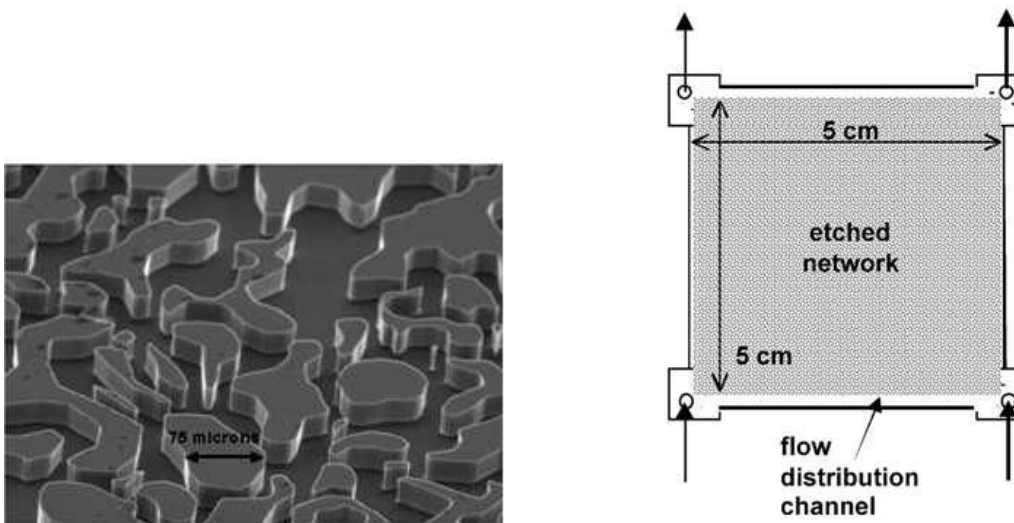


Figure 3.3.1a: Sketch of idealized etched pore network **3.3.1b: Sketch with dimensions of a micromodel**

The models have 4 injection/production ports and 2 horizontal channels with a width of 500 μm . The etched depth of the pore network was 25 μm . The micromodels were limited to a maximum pressure of 2bar. Exceeding the pressure limitation would crack the models, and this occurred during initial experiments with Berea A. Porosity and permeability was measured in the microfluidic laboratory, and a detail explanation is given in chapter 4.

3.3.2 High Pressure Silicon Wafer Micromodels

The high pressure micromodels were constructed and delivered by Micronite Microfluidics [36]. The models were formed as chips, and were customized and design after 2D images of Berea sandstone thin sections. Twelve models were delivered, where four of the models were manufactured with a horizontal channel in the middle of the pore structure, simulating a fracture. The models were created in fused silica, and fitted with 4 injection/production channels. Unlike the low pressure micromodels each of the ports had a small, vertical channel connecting the ports with the pore network. The models were placed in polymer cartridges, designed to fit the high pressure micromodel holder, and connected with ferrules on 1/16 steel tubings.

Figure 3.3.2a displays a customized high pressure micromodel in a polymer cartridge. The scale of the pore network were smaller than in the low pressure micromodels, and the size of the models were 1.3 x 2.6 cm with a depth of 20 μ m. Porosity and permeability measurements were done in a matter similar to the measurement process for the low pressure micromodels (chapter 4.4.). The greatest benefit with the models is the ability to withstand high pressure, with a maximum pressure limitation of 90 bars. This made experiments with liquid CO₂ possible. The models has a maximum operating temperature of 50°C, and this will be useful in the future when attempting to do experiments with supercritical CO₂.



Figure 3.3.2a: High pressure micromodel in a polymer cartridge

While the low pressure models were modeled after an idealized sandstone pattern, the high pressure models were manufacture with a more realistic pattern. The grains were rougher around the edges as can be seen from **Figure 3.3.2b**.

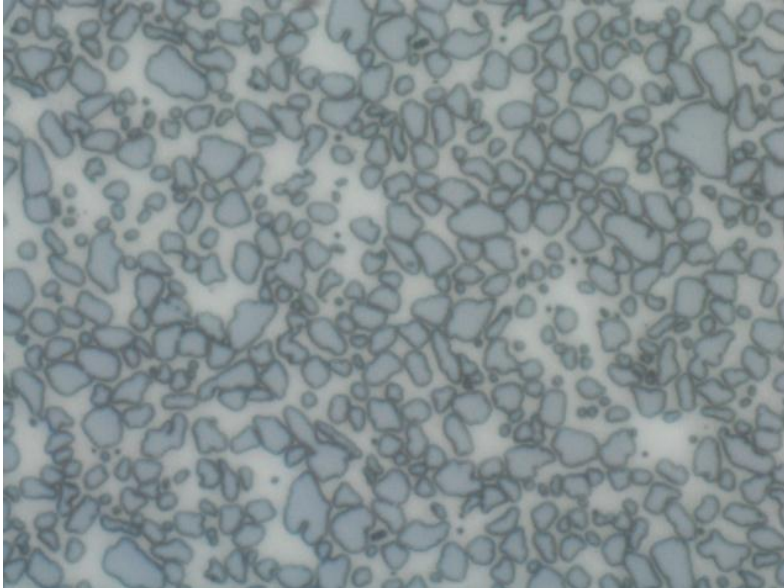


Figure 3.3.2b: Image of realistic sandstone pattern in high pressure micromodel B1

4. Experimental Procedure

The experimental procedures were similar for the experiments performed in both the low and high pressure silicon wafer micromodels. The main difference was the injection rates and the pressures applied to the models during the experiments. The customized high pressure models allowed higher pressures and injection rates to be used, which enabled experiments with liquid CO₂. The boundary conditions for the models, and the experimental procedure is explained in detail in this chapter.

4.1 Boundary Conditions

Both models had four ports where connections with tubings were possible. Boundary flow conditions were controlled directly with the ports by leaving them open or closed. The combination of this determined the direction and the boundary condition of the flow. **Figure 4.1a-c** displays the combinations used during the experimental part of this thesis using the low pressure micromodels.

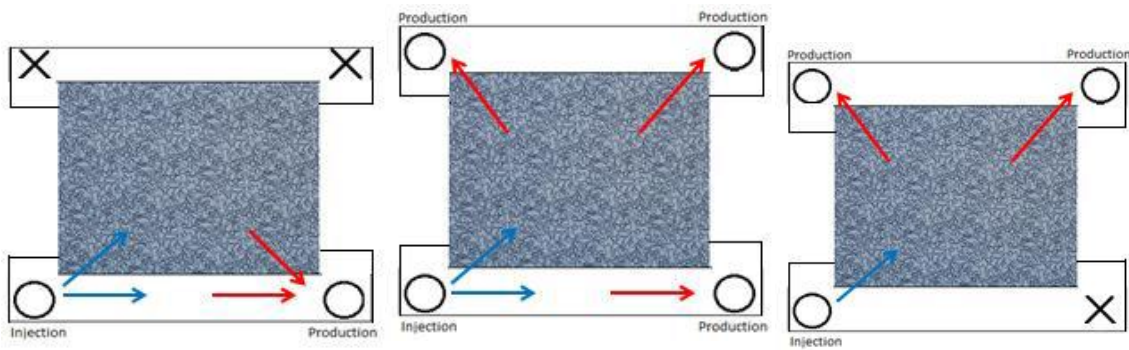


Figure 4.1a-c: Three different setups used during experiments; (a) closed opposite ports, (b) all ports open, (c) closed port in injection channel

Figure 4.1a displays a setup used where both ports in the channel opposite to the injection ports were closed. Fluids were displaced by counter-current flow, and a small pressure gradient was achieved. In the second figure (b) all ports are open, one injecting and the other three producing. Flow was co-current and the pressure drop across the model was linear to the injection pressure. The last figure (c) displays the case where one port is closed in the injection channel, one used as an injector and the last two as producers. Under this setup fluids flowed co-current while the pressure gradient was equal to the injection pressure. These setups were used for the experiments with the low micromodels. For the experiments with the high pressure micromodel one boundary condition was used; fluids were injected from the upper right side of the models, produced from the lower left side, with the two remaining ports closed.

4.2 Water Imbibition and Water Filling

The models were fully saturated with water through water imbibition processes. Before the imbibition process, the models were filled with either air or CO₂. During the imbibition process flow mechanism, the effect of wettability, and present of viscous or capillary fingering was studied. After primary drainage, imbibition was studied when the models were partially filled with oil at the irreducible water saturation. Due to the models being water-wet, we could study the water spontaneously flow through the pore network. Two setups were used during these experiments; all ports open and closed opposite ports.

Before saturating the models 100% with water, the models had to be cleaned by removing the remaining oil. This oil was not displaced by water due to the pressure limitation in the low pressure micromodels. CO₂ was injected at low rates over a period of time, to clean the model for both oil and water. After the models were cleaned water was injected while the injection rate was kept low. During early experimental work the pressure exceeded 2 bars, causing one of the low pressure micromodels to crack (chapter 6.5). This experience amplified the need for pressure monitoring and injection control during the experiment with the low pressure micromodels. Saturating the high pressure models was an easier process, and while the process with the low pressure models took a few days, the high pressure models were saturated in a few hours. Working with higher pressures enabled us to rapidly displace the gas from the model.

4.3 Permeability Measurements

After the models were 100% saturated with distilled water, the absolute permeability was measured. Water was then injected into the models with 3-4 different rates. The pressure drop was measured for each of the different rates. Calculations were done using equation 1.2, Darcy's law, where the width of the pore network multiplied with depth of the pores was used as the cross-section (A) in the equation. The absolute permeability was calculated as the average of the permeability at the different rates.

The permeability was measured both for the low pressure and the high pressure micromodel. For the low pressure micromodels the absolute permeability was measured first for the channel with all ports open, and then for the pore network by closing the port in the same channel as the injector and thereby forcing the water to be displaced through the pore network. The permeability of the low pressure micromodels was relative close to the permeability of the high pressure models, despite the high pressure micromodels ability to withstand much higher pressures. This shows accuracy in the manufacturing process, and difference in permeability is caused by the models being manufactured after different sandstone patterns. This means that even though the high pressure models are of a smaller scale, the flow will meet the same resistance in the high pressure models as in the low pressure models, reflected in similar permeability values.

4.4 Porosity and Saturation Measurements

Due to the small volumes in the micromodels, as well as the volumes of the channels and the volumes in the tubings, traditionally saturation and porosity measurements are difficult to accomplish. The porosity was measured using an image software called “*Image J*”. Images were taken from four different sections in the model, after the model was 100% saturated with Fluorescein water. The images were then analysed using *Image J*. The software converted the images into binary images (see **Figure 4.4a**), and the grains of the matrix were black while the water in the pores was turned into white. The software measures the number of pixels represented by each of the colours in the image, and by dividing the amount of white pixels on the total amount of pixels, porosity calculations were made possible. The porosity was calculated based on the average porosity of the four images.

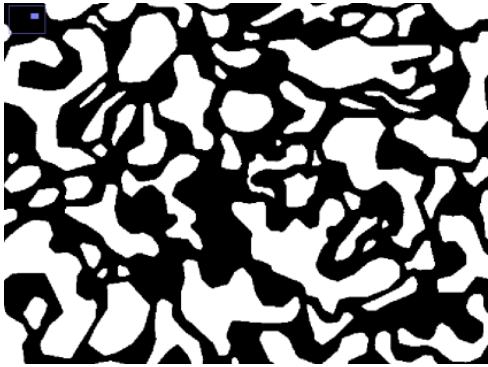


Figure 4.4a: Binary images from *Image J* used for porosity calculations

Saturation calculations were also done by using *Image J*. The present of different phases represented by different colours, made the method used for porosity calculations inadequate when calculating the saturations. Using the function “colour threshold”, the whole pore network was given the colour red. By manually selecting the range of colour that the red colour should cover, we could assign the red colour to one of the phases. **Figure 4.4b** displays an image before and after applying “colour threshold” to brownish oil phase in the image.

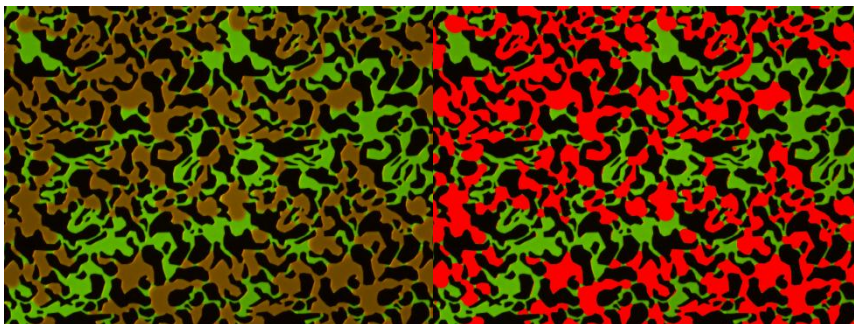


Figure 4.4b: Images of oil and water in a micromodel, before and after adding red “colour threshold” to the oil phase

After applying colour threshold to the image, "Analyze -> Tool -> Colour Histogram" was selected. The amount of red pixels was divided by the amount of pixels for the previously calculated porosity, giving the saturation of the selected phase. When three phases were present calculations were done this way for both the water and oil, since the CO₂ had a dark colour making it difficult for the image software to distinguish between the CO₂ and the matrix.

The irreducible water saturation, the residual oil saturation and the recovery factor were calculated using the image analysing software *Image J*. The recoveries were calculated by dividing the residual oil saturations with the initial oil saturation at S_{iw} . Average saturations and porosities from four different sections in the micromodels were used to account for the variation in pattern and displacement. There are some uncertainties when using image software to calculate both porosity and saturations and these are discussed in the uncertainties section in the appendix.

4.5 Primary Drainage

After saturating the models 100% with water, primary drainage with oil was performed. The models were saturated until the irreducible water saturation (S_{iw}) was reached. The oil migration and displacement of water was studied during this process. After the primary drainage contact angle measurements were done to determine the models wettability, and S_{iw} was calculated. Primary drainage of the low pressure micromodels was done both with all ports open and with closed opposite ports. The closed opposite port setup was used to study if the oil viscous forces were high enough to overcome the capillary pressure in the matrix, and displace the water. This was possible in the low pressure micromodels due to the two horizontal channels. The high pressure models were saturated with oil in a similar manner as when saturating the model with water.

4.6 CO₂ Gas Injection

CO₂ was injected both as secondary and tertiary injection. The purpose of the injection was to compare CO₂ gas injection with secondary water injection and liquid CO₂ injection, and to compare secondary and tertiary CO₂ gas injection. CO₂ in gaseous state was injected into the low pressure micromodels through connection with the syringe pump, while liquid CO₂ was used for the experiments with the high pressure micromodels. From the phase diagram (Figure 2.4) we observe that only CO₂ in gas state is achievable under the pressure limitations given by the low pressure micromodels, while the high pressure models can utilize liquid CO₂ under sufficient pressure conditions.

4.7 Liquid CO₂ Injection

Before experiments with liquid CO₂, all the valves of the SP-5200 pump were opened. The two cylinders in the pump were used as a producer and injector respectively. The cylinders were still connected, which meant we had a confined, cycled system. CO₂ gas was then injected into the system, and pressure was built up to approximately 50 bars. The CO₂ tank was then closed for one hour so the gas could come close to room temperature (thermal equilibrium), before the connection was closed between the two pumps. Equilibrium between the pumps prevents CO₂ gas to enter the high pressure micromodel. The injection pump was then set to constant injection rate, while the receiving pump was set to constant pressure. The pressure was set high enough for the CO₂ to flow in a liquid state. The experiment was observed and analysed through the inverted microscope and the connected image software.

The initial setup made it difficult to reach pressures above 59 bars, and a modified setup was required (see Figure 3.1b). In addition an experiment with the first setup resulted in a cracked micromodel (chapter 6.5). A QX pump and an additional CO₂ tank were connected to the SP-pump. Each cylinder on the SP-pump was equipped with a deliver and a fill valve. The fill valve was closed for the production cylinder and the rest of the valves were open, allowing gaseous CO₂ to flow through the micromodel as pressure was rising. Water was injected from the QX pump towards the additional CO₂ tank, causing pressure to be increased over the entire system and enabled the required pressure for liquid CO₂ injection.

The observations and findings are presented under the “result and discussion” section of this thesis.

III. Results and Discussion

The results and discussion are divided into two parts, representing the two types of micromodels used during the experiments. Chapter 5 consists of experiments done on the low pressure silicon wafer micromodel, while chapter 6 contains the results and discussion from the experiments on the high pressure silicon wafer models. The experiments are presented in the natural order of completion for each model.

Experiments performed on low pressure silicon wafer micromodels include spontaneous imbibition of water-air and water-CO₂, primary drainage, and three-phase gaseous CO₂ injection. Displacement and flow mechanisms were studied, as well as flow stability. Experiments on the high pressure silicon wafer micromodels enabled a higher injection rate and higher pressure. The experiments include primary drainage, CO₂ gas injection, liquid CO₂ injection and solution gas drive. Displacement mechanisms were studied. The liquid CO₂ experiment is compared with gaseous CO₂ injection in the last section, and the results for the two models are discussed.

5. Low Pressure Silicon Wafer Micromodel

5.1 Porosity and Permeability

The porosity of the low pressure micromodels were calculated from 100% water saturated models. The water was mixed with high a concentration of Fluorescein at 1:100 000, making it easy to distinguish between the water and the grains in the matrix. Images were captured from four different locations of the model and processed with the image software, *Image J*. From binary images the average porosities were calculated. The porosity for Berea D was calculated to be $52\% \pm 5\%$ and $50\% \pm 5\%$ for Berea A.

For the absolute permeability measurement Berea D was continuously injected with water at three different rates. Permeability measurements were performed at the rate 0.5, 1.0 and 2.0ml/h. and the absolute permeability was measured to be $0.69D \pm 0.05D$.

The methods for calculating and measuring both porosity and the permeability are equal for both the low and high pressure micromodels. The methods are explained in section 4.3 and 4.4, and are explained in more details for the high pressure silicon wafer micromodels in section 6.1.

5.2 Spontaneous Imbibition

Spontaneous Imbibition Air – Water

The Berea B micromodel was filled with air, before spontaneous imbibition was performed. Distilled water was injected at a rate of 1ml/h with opposite ports in the micromodel closed. The boundary conditions and the low flow rate contributed to a forced counter-current displacement and a low differential pressure over the matrix was expected. Water entered the matrix throughout the injection channel, and was observed to re-entered the matrix after reaching the closed opposite channel. The flow was visualized through the bright light filter and no Fluorescents were needed because water was darker than the air. The water filled the channel before entering the matrix and displacing the air. **Figure 5.2.1** displays the front of the water at 10X zoom displacing the air in the lower left corner of the micromodel, close to the injection port.

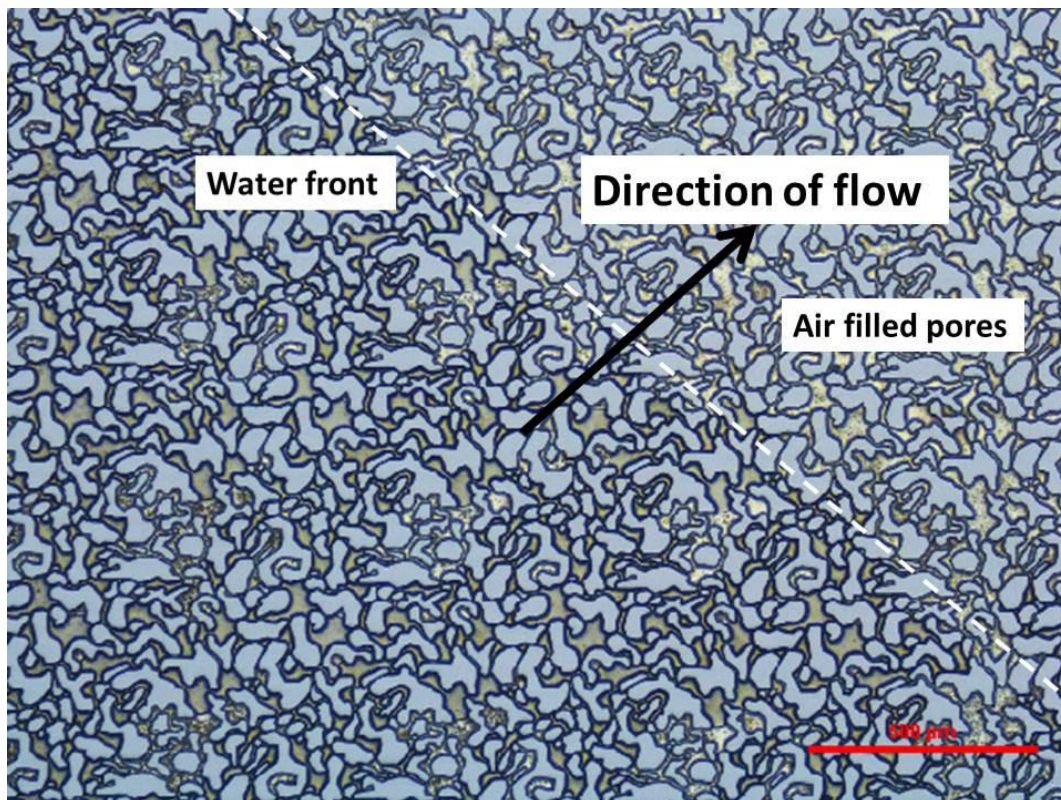


Figure 5.2.1: Stable, radial water front displacing air during spontaneous imbibition

The water displaced the air with a stable, radial front. The air was displaced by pore-to-pore filling mechanism, and the front advanced in a slow and stable manner. Water entered the matrix throughout the channel, and followed the same radial displacement pattern. No unstable front events were observed at the low injection rate, contributing to a good sweep and low residual air saturation.

The injection rate was increased to 2ml/h after 20minutes, and the focus area was moved towards the middle of the model, close to the injection channel. The magnification on the microscope was switch to 5X zoom. Fingering was observed throughout the pore network when the injection rate was increased, including from the radial front. In **Figure 5.2.2** a large finger developing close to the injection channel advances towards the opposite channel with the closed ports.



Figure 5.2.2: Large water finger advancing from the injection channel towards the opposite channel with closed production port during spontaneous imbibition at 2ml/h injection rate.

The interface between the air and water is represented by the sketched red line. A general observation was that the advancing water fingers by-passed large volumes of air and advanced rapidly towards the opposite channel, providing a poor sweep and high residual air saturation. Capillary end effects were observed as water reached the opposite channel, as seen from **Figure 5.2.3a and b**.

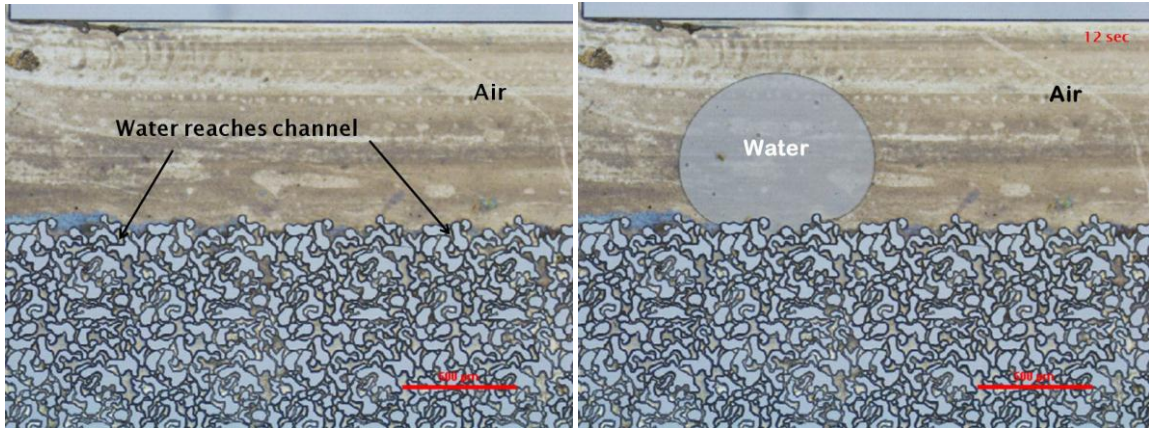


Figure 5.2.3a & b: Capillary end effect in air filled channel during spontaneous imbibition; (a) water reaches air-filled channel without entering, (b) water enters the channel after 12 seconds

Capillary end effects occur when a fluid subjected by capillary pressure reaches an area with no capillary pressure [37]. The water reached the matrix adjacent to the opposite channel, and stopped until the water pressure was equal to the capillary pressure, $P_c=0$. It was observed that water reached the air-filled channel, but did not enter the channel immediately (see Figure 5.2.3a). Water breakthrough in the channel was observed 12 seconds after the water reached the channel (Figure 5.2.3b), when the water phase pressure was increased to be equal to the air phase pressure in the channel. The water saturations increased in the matrix until the end point for spontaneous imbibitions was reached at $PC=0$. From equation 1.6.1 equal phase pressure for water and air gives $P_c=0$ and the end effects are diminished.

Spontaneous Imbibition CO₂ – Water

Two spontaneous imbibition tests were performed in the CO₂-filled model Berea D by injecting water directly into the injection channel with a constant volumetric flow rate of 0.5 ml/h, with boundary condition all ports open. The injected water was labeled with both Fluorescein and FT-175 in separate tests. The flow and displacement between CO₂ and water was studied using the blue light filter with 5X zoom magnification to distinguish between the water and CO₂. Unstable capillary fingering was observed immediately after water injection was initiated. A large capillary water finger initiated close to the injection port and advanced rapidly towards the opposite channel. **Figure 5.2.4** shows the capillary finger approximately 20 sec after water injection started. The injection channel is located directly below the image, but cannot be seen in the image.

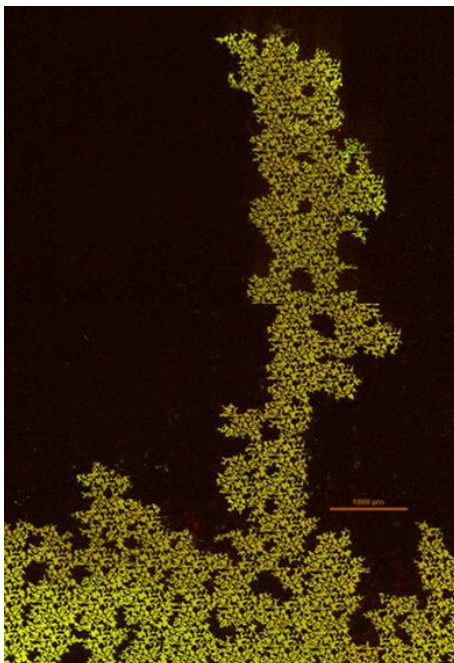


Figure 5.2.4: Capillary water finger advancing through CO₂-filled matrix during spontaneous imbibition[28]

Due to the limited field of view Figure 5.2.4 was created by combining three snap-shot photos into one large image, so the complete capillary water finger could be displayed.). Compared to the spontaneous imbibition of water in an air-filled micromodel, no stable front or radial flow was observed. Capillary fingers were only observed at high flow rate for water-air (2ml/h). This may be related to the difference in the ratio between viscous and capillary forces. To be discussed in detail below. Capillary fingers advanced throughout the pore network, leaving large volumes upswept, and contributing to high residual gas saturation.

Capillary fingers were observed both normal to and opposite to the direction of flow, often merging into clusters and trapping CO₂ behind the front. Using the same injection rate, the observed rate of CO₂ displacement was much higher compared to the rate of air displacement in identical tests. Large groups of pores were rapidly water-filled in a pulse-like manner, compressing and displacing the CO₂. Observations indicated that larger clusters were displaced with water/CO₂ compared to water-air displacement. No capillary end effects were observed when the water finger reached the gas-filled, opposite production channel. The water was produced directly to the channel, without capillary hold up, filled the channel and even re-entered the matrix where the CO₂ saturation was high. The displacement slowed down after the water breakthrough to the channel, and the saturation of trapped CO₂ in the matrix was reduced by dissolution. **Figure 5.2.5a & b** displays a trapped cluster of trapped CO₂ slowly being displaced by water.

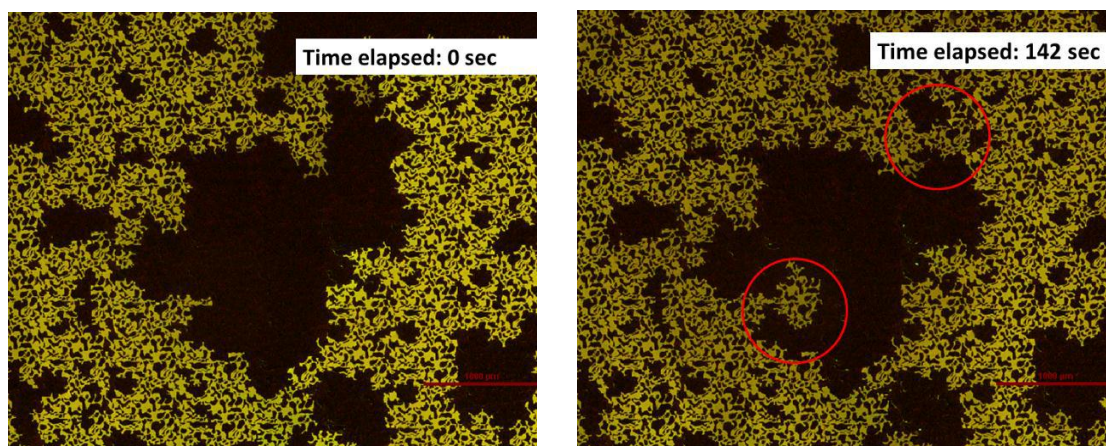


Figure 5.2.5a & b: Trapped CO₂ displaced by water[28] (a) a CO₂-filled cluster is trapped by water, (b) water slowly displaces the cluster

Dissolution is the mechanism displacing the trapped CO₂. The dissolution was studied during the experiment with Fluorescein water at a magnification of 20X zoom. **Figure 5.2.6a, b, c and d** displays CO₂ slowly dissolving into the water phase. The green colour represents the water phase, while both the CO₂ and grains are black. The CO₂ are distinguished from the grains by small water film, enabling us to identify the gas. The trapped CO₂ was compressed by water as the water saturation increased. After being sufficiently compressed the CO₂ dissolves slowly in the water phase and 100% water saturations of the entire micromodel were obtained after a few hours.

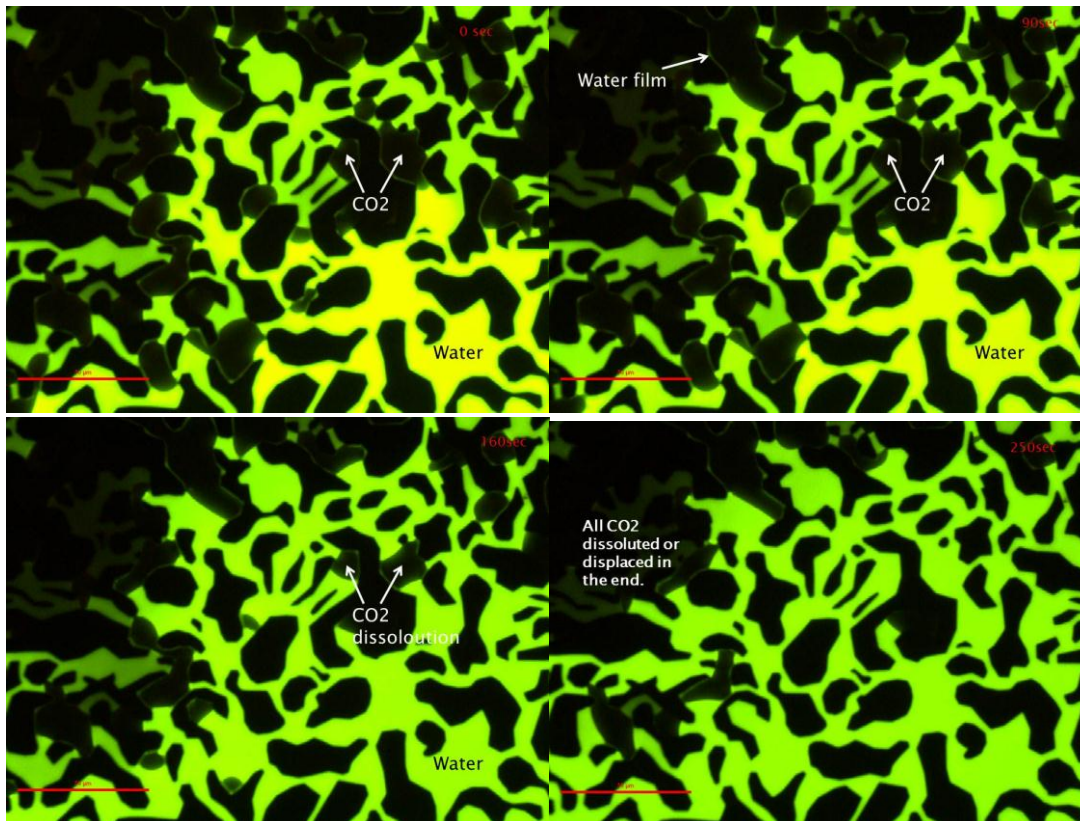


Figure 5.2.6a, b, c & d: Dissolution of CO₂ during spontaneous imbibition; (a) CO₂ is trapped in some pores, (b) water films are observed on the pore walls in the CO₂-filled pores, (c) the CO₂ is slowly being compressed by water, (d) most of the CO₂-filled pores are dissolved in the water.

Discussion Spontaneous Imbibition

Stable and unstable flow regimes were observed during the spontaneous imbibition experiments. Capillary fingering was identified and observed. Distinguishing between capillary fingering and viscous fingering was done by identifying the direction of finger relatively to the main direction of flow. Viscous fingering will normally be in the flow direction, while capillary fingering occur normal and sometimes opposite to the direction of flow. In addition mobility ratios can be calculated to distinguish between the two types of fingers. Calculations has proven to provide a mobility ratio much smaller than 1, which favours a stable displacement[28]. Further calculation of the capillary number in the same thesis provided a low estimated result. This supports the theory of capillary forces being dominating in micromodels, due to the small dimension of the pore network. High rates were required for viscous fingering to occur during the spontaneous imbibition process with both water-air and water-CO₂. The flow was observed to be both stable an unstable during the different experiments. When closing the opposite channel and keeping the differential pressure across the matrix low and the injection rate low, a stable and radial displacement was observed. The water was injected in the production channel and forced the gas to be counter-current displaced throughout the pore network. Increasing the injection rate resulted in an unstable front, represented by capillary fingering.

The observed capillary fingers supported the theory that capillary forces should dominate the flow. A spontaneous imbibition experiment was carried out to determine the effect of viscous forces. Water was injected into the injection channel of an air-filled micromodel. The injection was stopped as the water entered the matrix. The water advanced slowly in a large finger, towards the production channel, and stopped right before the production channels. For the water to enter the production channel, the capillary pressure had to be equal to the phase pressure[37]. The present of end effects will prevent the capillary fingers to enter into the air-filled channel until the pressures are in equilibrium. Water breakthrough was observed after sometime when the water saturation and phase pressure had increased (Figure 5.2.3b), thereby supporting the theory of capillary forces being dominating on the pore scale at low injection rates. During imbibition with water and CO₂ viscous forces caused the more viscous water to immediately enter the channel and displace the low viscous CO₂ gas. At low injection rates (0.5ml/h) the water front was stable in the air-filled model and unstable in the CO₂-filled model. The capillary number is greater for CO₂ than for air, and the front is therefore unstable for CO₂. The impact of viscous forciers will increase with increased injection rate[38]. The water imbibition experiments are summarized in table 5.2

Table 5.2: Summarized characteristics for water imbibition experiments

Displacement process	Model	Flow conditions	Flow regime	Characteristic features
Imbibition Air - Water	Berea B	Low flow rate and low Δp	Stable front	Good sweep => low residual air saturation Low capillary imbibition rate => stability
Imbibition CO ₂ - Water	Berea D	High flow rate and high Δp	Unstable capillary fingering	By-passing and trapping of gas => poor sweep Dissolution of trapped CO ₂

5.3 Primary Drainage

Primary drainage was performed on micromodels 100% saturated with Fluorescein or FT175 water. Oil with Nile Red was injected, thereby simulating the process of oil migrating through a reservoir rock. Flow stability and displacement mechanisms were studied. Saturation calculations were performed to calculate the irreducible water saturation, while contact angle measurements (5.6) provided an estimated wettability of the reservoir models.

Primary Drainage Berea D

Oil with Nile Red was injected with a constant low rate of 0.8ml/h, with boundary condition all ports open. The model was initially fully saturated with FT175 water. Oil was injected into the injection channel and entered the pore network after the threshold pressure was reached. Threshold pressure is defined as *the minimum pressure needed to initiate the displacement of a wetting phase by a non-wetting phase from a porous medium 100 percent saturated with the wetting phase*[39]. In previous experiments the threshold pressure for the low pressure silicon wafer micromodels was approximately 0.27 bar[28]. The threshold pressure was observed by filling the injection channel with oil, and observing at what pressure the oil entered the pore network.

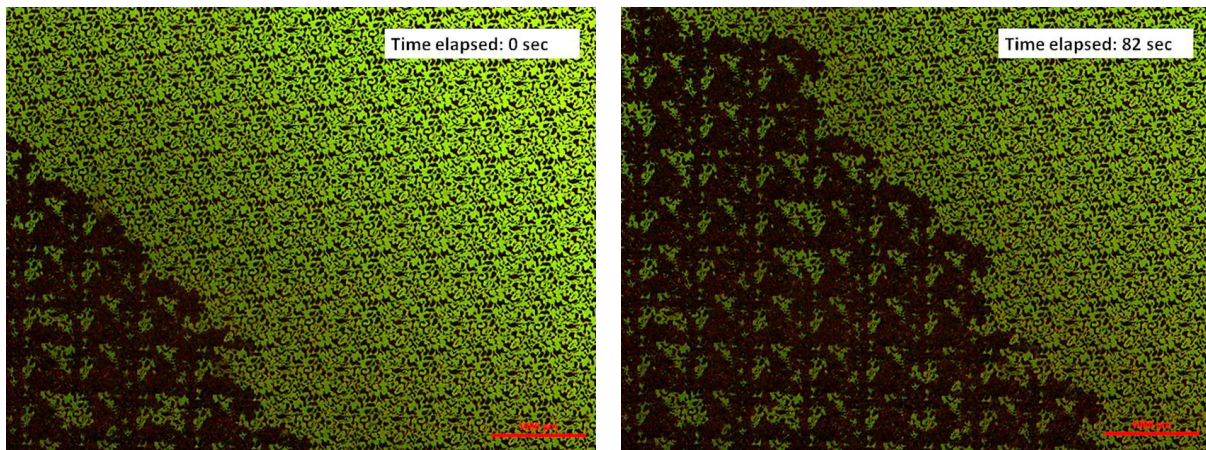


Figure 5.3.1a & b: Stable radial displacement during primary drainage leaving by-passing water filled clusters

From **Figure 5.3.1a and b** a stable radial front was observed in the lower left corner close to the injection channel at 2X zoom magnification. The oil advanced slowly and stably by filling clusters of pore and displacing the water. From Figure 5.3.1b small cluster of by-passed water was observed. Some film flow of water was observed from the by-passed clusters, reducing the water saturation towards the irreducible saturation. Oil fingers were observed from the injection channel, close the right side of the model, but did not dominate the displacement. The overall sweep efficient was observed to be good. Saturation calculations after the primary drainage process was completed, provided an estimated irreducible water saturation $S_{iw} = \underline{0.17} \pm 0.05$.

Primary Drainage Berea G - Closed Opposite Ports

The micromodel Berea G was saturated with Fluorescein water before oil with Nile Red was injected with a constant rate of 1ml/h with boundary conditions closed opposite ports. Flow stability was studied at 2X zoom magnification. Initially the flow was similar to the flow with boundary conditions all ports open, where a stable radial oil front was observed. The front advanced through cluster filling events. Fingering was observed after a while, originating from the stable front.

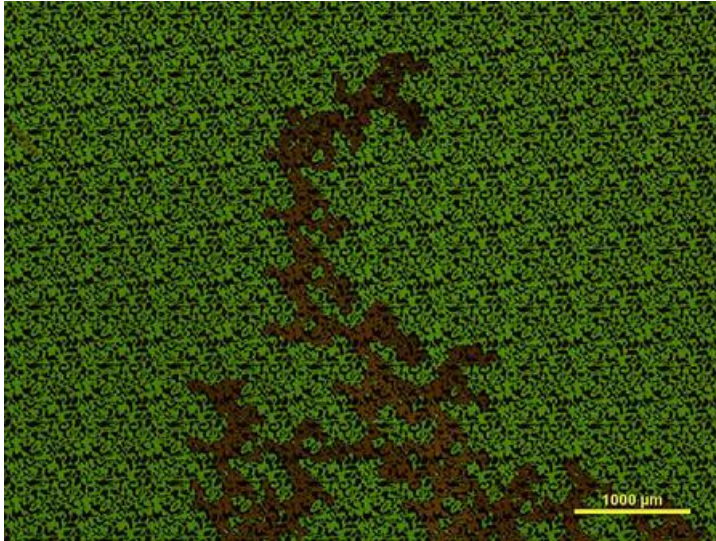


Figure 5.3.2: Capillary oil finger during primary drainage

From **Figure 5.3.2** a large capillary oil finger was observed. Clusters of water-filled pores were rapidly displaced by oil, and oil finger was formed. The oil fingering resulted in a poor sweep of the micromodel. Similar to the spontaneous imbibition process with water and CO₂, the fingers merged, by-passed and trapped clusters of water-filled pores. After oil breakthrough no further displacement was observed. High residual water saturation was calculated to $S_{iw} = 40\% \pm 5\%$.

Primary Drainage Berea G - Open Ports

The Berea G model was re-saturated with Fluorescein water after the primary drainage experiments with closed opposite ports. Primary drainage was then performed with boundary conditions all ports open with an injection rate of 1ml/h. Displacement mechanisms were observed and studied at 10X zoom magnification. Two main displacement mechanisms were observed: film flow and piston-like displacement (Figure 1.8.1). **Figure 5.3.3a-f** is a series of captured images during the experiment, where the above mentioned displacement mechanisms were observed.

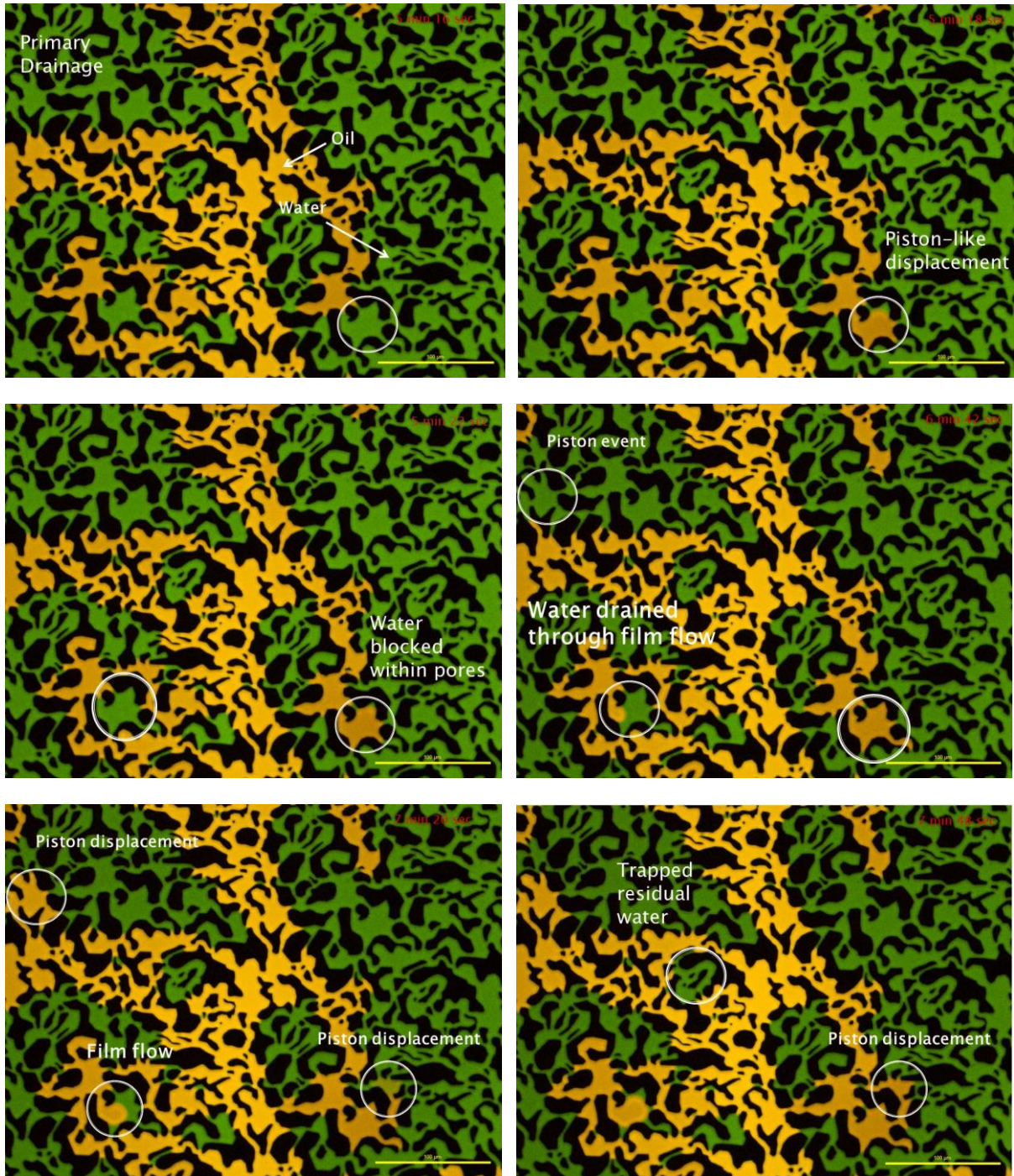


Figure 5.3.3a-f: Pore level displacement mechanisms during primary drainage; (a) the marked pore is filled with water. (b) the oil displaces the water through a piston-like displacement, (c) water is observed to be trapped in the pore marked to the left and in the pore throat of the right marked pore, (d) water trapped in the pore throat and the trapped water in the left marked pore is slowly drained through film flow, (e) piston displacement is observed in the upper marked pore as film flow continues in the lower left pore, (f) another piston event is observed to the right and trapped residual water is observed within the oil phase.

Piston-like displacement was observed from Figure 5.3.3a-b. A sharp interface between the oil and water advances and displaces the water-filled pore in a piston-like manner. The water was drained instantly through connected water-filled pores. Some water was trapped in the pore throat in the lower right marked pore, without being displaced by the piston event (Figure 5.3.3c). Two types of piston displacements were observed during these experiments, and they are distinguished by the stability of the displacement. Regular piston displacement has a stable advancing interface, while during a Haines' jump the interfaces becomes unstable and advances through a jump, before stabilizing again. Haines' jump was observed through the microscope, but not captured clearly on the computer. The displacement of water was rapid and images being captured every two seconds, made Haines' jump difficult to capture.

Film flow was observed before oil breakthrough. From Figure 5.3.3c-f film flow were observed and captured. The water-filled pore to the left was surrounded by oil and presumed trapped. The pore was slowly drained through films of water flowing along the pore wall in the water wet micromodel. After close to 2 minutes most of the water was displaced. As the water was slowly displaced by film flow in one pore, other pores are subjected to piston displacement (Figure 5.3.3e & f).

Discussion Primary Drainage

Table 5.3.1: Viscosity of injected and produced fluids[29]

Fluids	Viscosity [cP]
Water	0,9322
CO ₂ gas	0,0147
Oil(n-decane)	0,8733

The mobility ratio between oil and water were calculated from equation 1.7.2 using the values from table 5.3.1. The end-point relative permeability of oil was assumed to equal to that of water, to make simple mobility calculations possible. The viscosity values are based on an isothermal process (constant temperature), measured to be 23 °C ± 0.5 °C. The mobility ratio between oil and water is calculated to be:

$$M_{o/w} \approx \frac{\mu_{water}}{\mu_{oil}} = \frac{0.9322cP}{0.8733cP} = 1.0674$$

The mobility ratio is close to unity, thereby providing a viscously, stable displacement and stable flow. Estimations of capillary number showed that capillary forces will be dominating when oil is the non-wetting phase during primary drainage[28]. The calculations also provided an indication that the viscous forces will increase with increased rate and higher relative permeability for oil. The same flow regimes as for spontaneous permeability were observed; both stable and unstable.

Stable, radial flow was observed as the clusters of water were displaced in a pulse-like manner, when a significant differential pressure existed across the matrix. The front advanced faster during the primary drainage compared to the radial front observed during spontaneous imbibition with water and air. The higher rate was suspected to increase the viscous forces that were further balancing the effect of capillary forces and contributed to a stable front. Saturation calculations provided under stable flow conditions produced an irreducible water saturation $S_{iw} = 0.17 \pm 0.05$, while unstable flow conditions produced $S_{iw} = 0.40 \pm 0.05$. The unstable flow had an earlier oil breakthrough in the production channel than the stable flow, and a poor sweep. No water was observed to be displaced after oil breakthrough, and this resulted in a higher value for the irreducible water saturation compared to stable flow conditions.

The unstable regime was observed with closed opposite channels. The flow was initially observed to be similar to flow under stable conditions, before fingers appeared. The fingers advanced rapidly, merged and trapped water. The direction of the fingers normal and opposite to the flow, indicate the capillary forces being dominant. No water was produced after oil breakthrough, since the oil followed the easiest path through the matrix. Increasing the injection rate, thereby increasing the viscous forces, caused more water to be displaced and produced.

The irregular flow pattern for the oil finger caused water-filled pores to be displaced at different times. Some water trapped pores were slowly drained as the pressure of the oil phase increased. The water escaped the pore from film flow on the surface of the pore walls. During piston displacement events, the water-filled pore was displaced with either an unstable (Haines' jump) or stable advancing interface. After primary drainage the larger pores were oil-filled while water occupied the smaller pores and pore throats. From the capillary pressure curve (Figure 1.4.2) the initial capillary pressure is observed to be low during primary drainage. No water is displaced before the threshold pressure is reached. Oil displaces the large pores first and the smaller pores are displaced as the capillary pressure increases. AT the irreducible water saturation, water will only be found in the smallest pores with the most narrow pore throat, and on the pore wall in the water-wet model. Characteristics features, flow conditions and flow regimes for the primary drainage experiments are summarized in table 5.3.2.

Table 5.3.2: Summarized characteristics for primary drainage experiments

Displacement process	Model	Flow conditions	Flow regime	Characteristic features
Primary drainage	Berea D	High flow rate and high Δp	Stable front	Film flow and piston displacement. Good sweep=>low S_{iw}
Primary drainage	Berea G	Low flow rate and low Δp	Unstable capillary fingering	Piston displacement. Fingering=>poor sweep No production after water breakthrough

5.4 Secondary Water Injection

The low pressure silicon wafer micromodels were limited to a pressure of 2 bars and this limited the injection rate of fluids. This provided some challenges when initiating secondary water injection after primary drainage. Some oil was displaced by the injected water and the injection rate was kept low so the pressure limitation was not exceeded. Under these conditions the recovery was observed and calculated to be in the range of 2-5 % with water injection. The phase pressure was higher for the oil than the water after primary drainage. This resulted in the threshold pressure being higher and close to the pressure limitation of 2 bars. Increased recovery with secondary water injection was therefore hard to obtain.

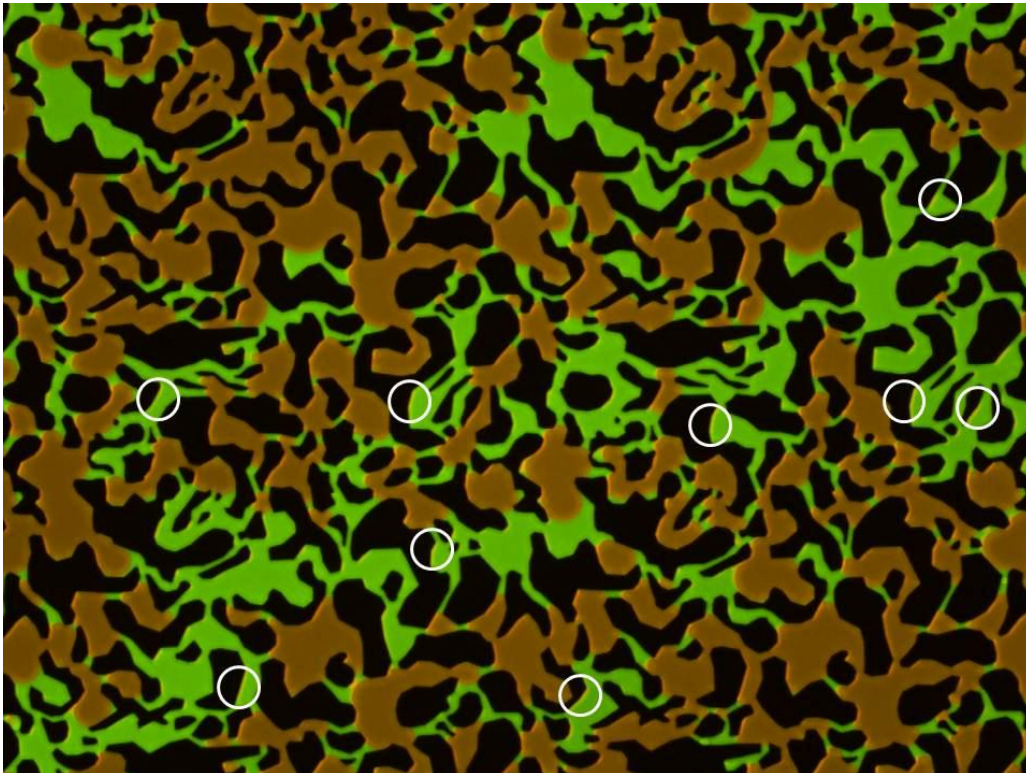


Figure 5.4: A snapshot showing water (green) and oil (brown) distributed within the pore space during secondary water injection. Retention of Nile Red on the pore wall is indicated by white circles.

From **Figure 5.4** a thin, brownish layer on some of the pore walls is observed and marked with white circles. This was retention of Nile Red from the oil phase. The models were water wet, and the influence of Nile Red might have an effect on both oil production and the wettability. Blocking of pore throats and water filming might be caused by the retention of Nile Red, and therefore reducing the recovery from water injection and changing the wettability. In addition to the Nile Red, the low pressure limitations was assumed to be the main reason for the low production and high residual oil saturation, after water injection was applied to the low pressure micromodels.

5.5 Three-Phase CO₂ Gas Injection

Tertiary Three-Phase CO₂ Gas Injection Berea B

The micromodel Berea B was initially partly filled with water and oil, enabling CO₂ injection to be studied in zones partially flooded by water. CO₂ was injected with a constant pressure of 1.5 bar with boundary condition all ports open. Initially the large pores in the model were filled by oil, while water occupied the small pores and pore throats. Flow and displacement was observed close to the injection port. The CO₂ displaced the larger oil-filled pores a few seconds after the injection was initiated, while the water initially was left untouched. The CO₂ phase appeared discontinuously while entering the pore network, and advanced rapidly before coming to a rest. This enabled visualization of all three phase in sections of the model. During the CO₂ gas injection a study of displacement mechanisms was performed. Piston displacement, snap-off, Haines' jumps and multiple displacements were observed. The injected CO₂ mobilized water through multiple displacements. The CO₂ displaced oil that in turn displaced water which again displaced oil and CO₂. From **Figure 5.5.1a-d** water displacing discontinuous CO₂ was observed. A stable interface advanced in a piston-like manner before becoming unstable and making a jump. The interface was then stabilized and the fluids were redistributed, before becoming unstable and jumping further.

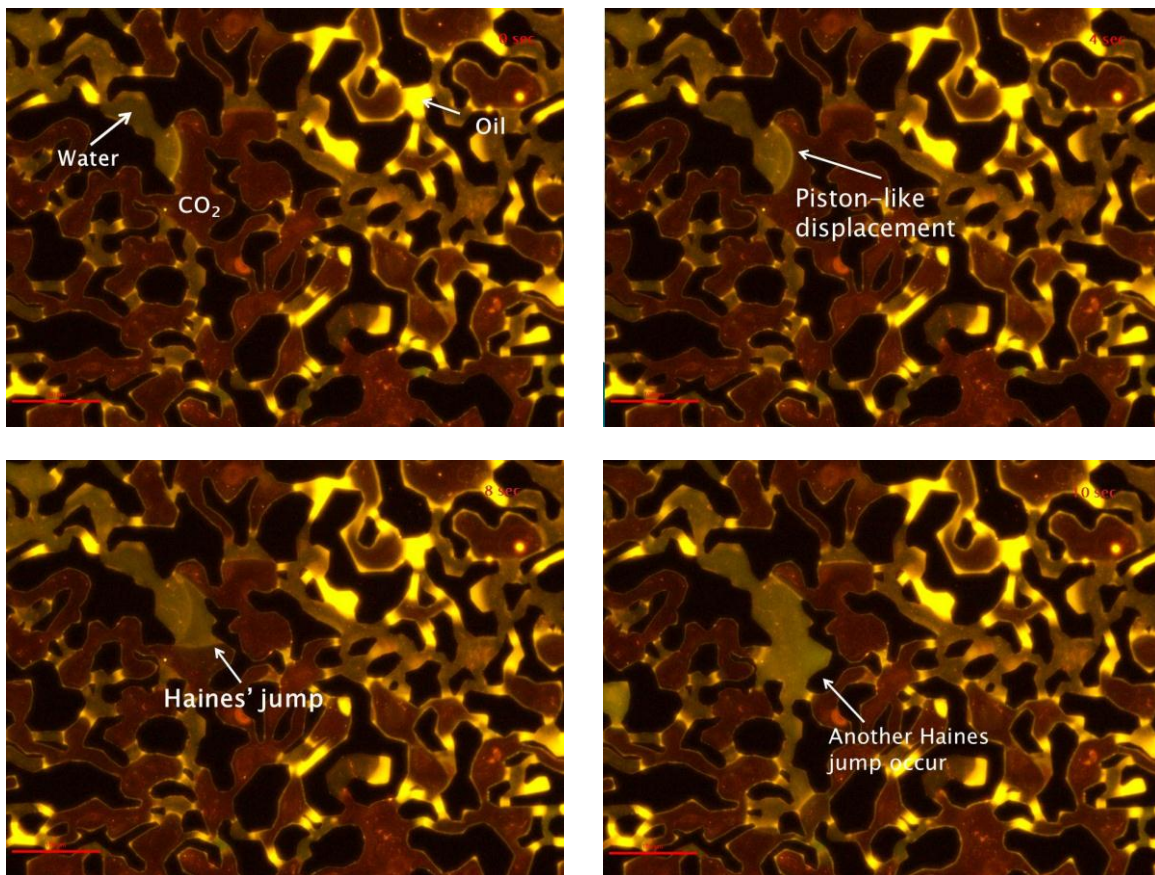


Figure 5.5.1a-d: Haines' Jump during three-phase CO₂ gas injection; (a) stable interface between water and CO₂, (b) the water advances in a piston-like manner, (c) the interface becomes unstable and a Haines' jump occur, (d) another Haines' jump is observed before the fluids are redistributed.

Tertiary Three-Phase CO₂ Gas Injection Berea G

CO₂ was injected into a partially water flooded model Berea G. The CO₂ was injected with a constant pressure of 1 bar with boundary condition all ports open. Interactions were studied between the opposite channel and the matrix through the bright light filter of the inverted microscope. The CO₂ was observed to advance fast in preferred flow paths from the injection channel towards the production channel. Bubbles of CO₂ were then observed to become capillary trapped when the flow path changed, as can be seen from **Figure 5.5.2d**. The bubbles remain trapped until either the capillary pressure decreased or the bubbles were sufficiently compressed, and escaped the pore through dissolution. Oil was observed to be displaced through piston displacement and film flow of spreading oil layers, while some water was displaced by oil through multiple displacements causing fluids to be redistributed. CO₂ flowed towards the opposite channel and was observed to be blocked by the redistributed fluids (**Figure 5.5.2b**), forcing the CO₂ to flow through new paths as the phase pressure increased (**Figure 5.5.2c**). Spreading layers of oil was observed to be displaced and flowed within the CO₂ flow path (Figure 5.5.2d).

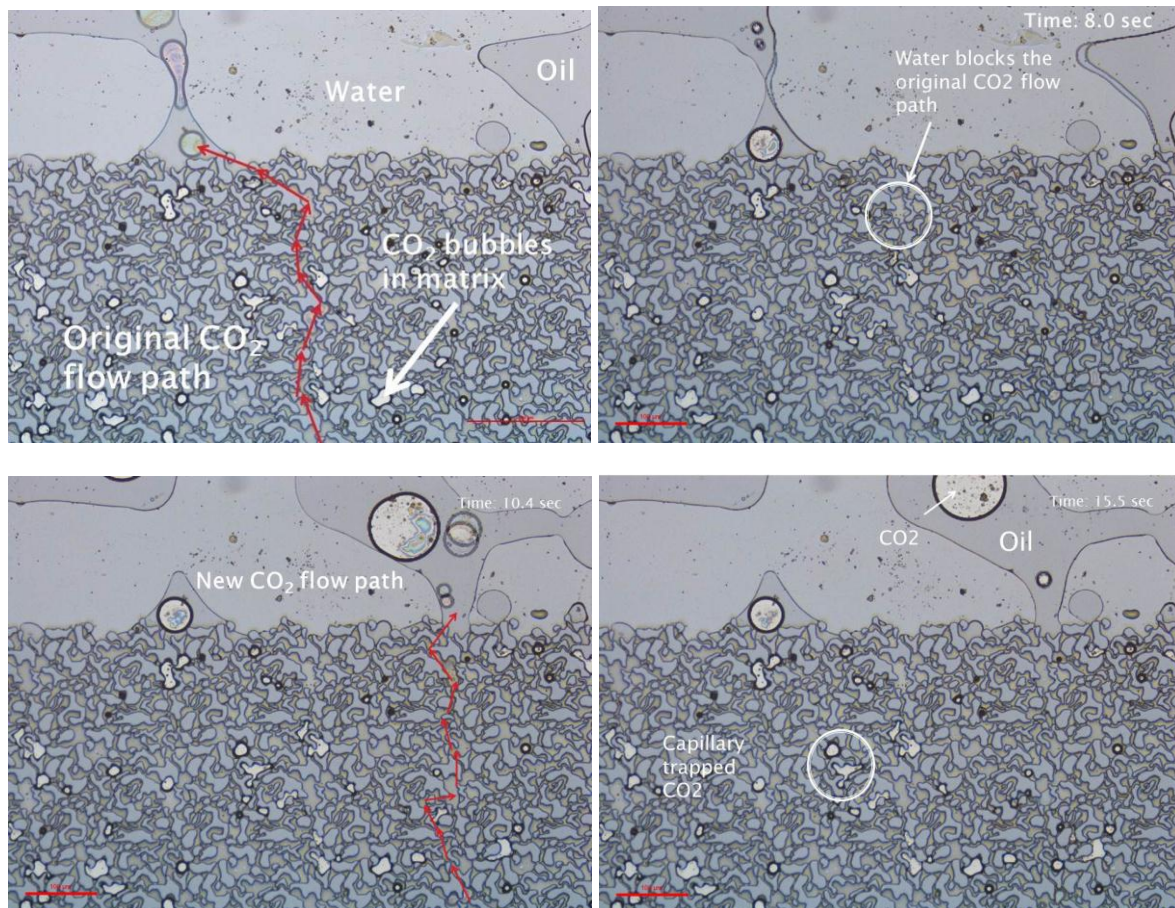


Figure 5.5.2: CO₂ changing flow path: (a) CO₂ flowing to the production channel, (b) displaced water blocks the original CO₂ path, (c) a new CO₂ path is observed, (d) CO₂ bubbles is capillary trapped to the left and displaces spreading layers of oil within the flow path

Secondary Three-Phase CO₂ Gas Injection Berea D

Model Berea D was injected with oil during primary drainage until the irreducible water saturation was reached. Secondary CO₂-gas was injected at constant pressure of 1 bar with boundary conditions all ports open. A section close to the middle of the micromodel was studied at 10X zoom magnification, as a stable advancing front could be observed. Haines' jumps and piston displacements were observed in addition to snap-off event and film flowing of both water and spreading layers of oil. Film flow and snap-off is displayed in **Figure 5.5.3a-d**.

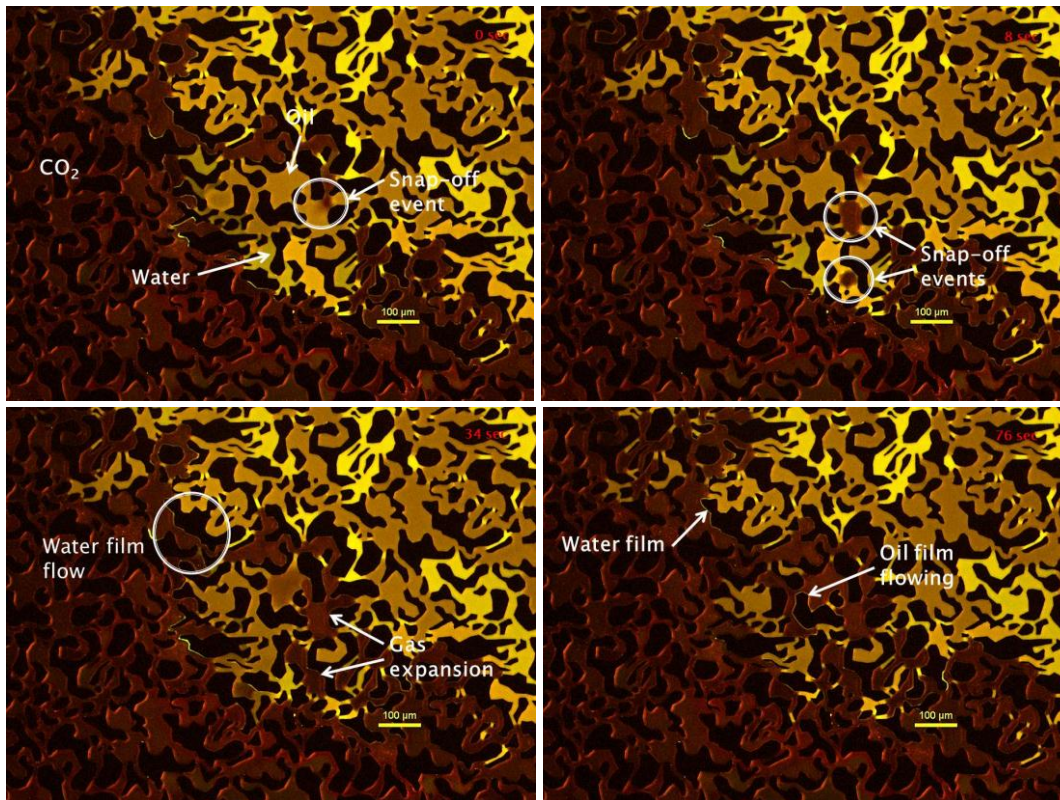


Figure 5.5.3a-d: Snap-off event leading to gas expansion and film flow; (a) CO₂ advance with a stable radial front, (b) CO₂ snaps off into the oil phase, (c) the snapped off CO₂ expands, (d) water and spreading layers of oil displaced through film flow.

The CO₂ advanced in a stable radial manner and eventually snapped off bubbles into the oil phase. The snapped off CO₂ immersed into the center of oil and water-filled pores (Figure 5.5.3b). Oil were observed to be displaced through gas expansion of the snapped off CO₂ (Figure 5.5.3c), while the water was displaced by the oil through multiple displacements and film flow. The phase pressure of the snapped-off CO₂ decreased due to the phase being discontinuous. The volume of the gas expanded as a result of the decreased pressure. Remaining water films and spreading layers of oil were gradually displaced through film flow (Figure 5.5.3d). After 16 minutes all the oil and water in the captured sections were displaced. The injection was continued for two days with a constant pressure of 1 bar. Almost all the fluids were displaced after one day and 100% was obtained after two days of injection.

Oil Recovery from Three-Phase CO₂ Gas Injection

The oil recovery from three-phase CO₂ gas injection was calculated from equation 1.9. The oil saturation after primary drainage ($S_{o,iw}$) was used as the *total reserve* (N) while the oil production (N_p) was obtained from the residual oil saturation ($S_{o,iw} - S_{or} = N_p$). Snap shots from the experiments represented by the images in Figure 5.5.3a to d, were used to calculate the recovery. During primary drainage an irreducible water saturation of $S_{iw} = 0.17 \pm 0.05$ was achieved, giving an initial oil saturation of $S_{o,iw} = 0.83 \pm 0.05$.

The section was studied with a magnification of 10X zoom for 16 min. The image sequence was recorded after CO₂ had entered the matrix and had started displacing the fluids. Snap shots were taken every minute and the oil saturation was calculated in *Image J* for each image. The oil saturations were plotted against time in **Figure 5.5.4**. The initial oil saturation was calculated to be $S_o = 0.54 \pm 0.05$, and after 16 min the oil saturation was approximately 0.015. The oil was displaced rapidly at first, as can be seen from the graph, and then slowly displaced towards a complete recovery. The fast displacement was caused by piston events and gas expansion of snapped-off CO₂, as a stable CO₂ front advanced to in a radial pattern. The remaining fluids were slowly displaced through film flows, as the graph reflects. Given these flow conditions 100% recovery can be expected. Similar results were observed after tertiary CO₂ gas injections.

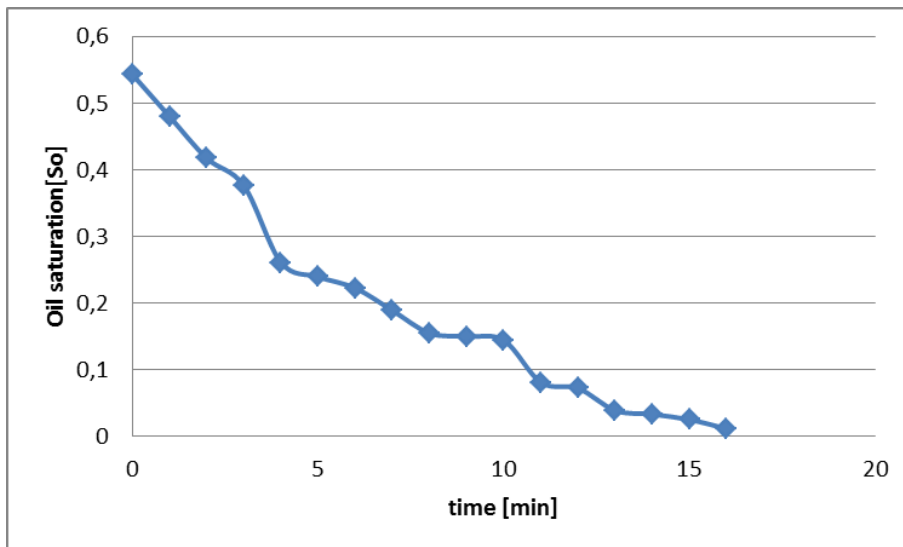


Figure 5.5.4: Oil saturation as a function of time during three-phase CO₂ gas injection

The result above was for a small section of the micromodel. Similar radial flow as well as fingers of CO₂ was observed throughout the model. Calculating the recovery for the entire micromodel over a short period of time was proved to be difficult. While sections close to the injection port had a good sweep, CO₂ fingering caused a poor sweep in selected sections of the micromodel. The average oil saturation of eight sections, were used to calculate the recovery after approximately 20 minutes of CO₂ gas injection. This gave a recovery of 73% with an estimated uncertainty of $\pm 5\%$ (see the appendix chapter). The injection of CO₂ was resumed and continued for 48 hours, resulting in a complete recovery.

Discussion Three-Phase CO₂ Gas Injection

The experiments with three-phase CO₂ gas injection on the low pressure micromodels were performed at a constant temperature of 23 °C at pressures not exceeding 2 bars. Under these conditions CO₂ gas is below the minimum miscibility pressure (*MMP*) and therefore immiscible with the oil phase. The CO₂ injection was therefore studied as an immiscible gas flood. Great recovery (73% ± 5%) was achieved for the low pressure micromodels starting at the irreducible water saturation. The threshold pressure was observed to be lower during CO₂ injection compared to water injection, as CO₂ instantaneously entered the matrix. This resulted in a much higher recovery from secondary CO₂ injection than from secondary water injection.

Through the experiments the displacement mechanism during gaseous CO₂ injection was studied. CO₂ was observed to preferably displace the oil phase, through piston displacement and snap-off events. CO₂ was observed to snap-off into both the oil and water phase, and displace the oil through gas expansion and piston events. From the ideal gas law[40] the volume is observed to increase as the pressure is decreased at constant temperature. The gas expansion was caused by a decrease in phase CO₂ pressure as the CO₂ became discontinuous. Both spreading layers of oil and water films were displaced through film flow. No observations of CO₂ displacing water were obtained as spreading layers of oil prevented contact, and the water was mainly observed to be displaced through multiple displacements.

Diffusion was considered to have a great effect on displacement and resulting in high recovery. Diffusion is a random movement of molecules from an area with high concentration to an area with low concentration[41]. Water and oil were displaced continuously, even in areas not in the flow direction's path, thereby indicating diffusive processes from the channels and capillary effects within the matrix.

The effect of film flow was observed to be greater than the effect of diffusive processes. Oil was observed to be present without water in areas completely swept by CO₂ gas. Water was only observed in films, being slowly displaced through film flow. The solubility of CO₂ in n-decane at 1 bar pressure and 25 °C was found in *The Journal of Chemical Thermodynamics* [42] and by combining the density of the CO₂[29], the solubility was calculated to be higher for CO₂ in n-decane than for CO₂ in water; 3.16g/L for CO₂ in n-decane and 1.45g/L for CO₂ in water. This indicated that spreading oil layers were displaced before the residual oil-filled pores through diffusive processes. The micromodels were completely drained of water and oil after more than 48 hours of injection, and CO₂ was therefore used to clean the models before initiating new experiments.

5.6 Contact Angle Measurements

The low pressure micromodels were manufactured with real rock properties. The micromodels the Department of Physics and Technology received from Stanford University were modeled after water-wet Berea sandstones. The wetting preference was identified visually at the fluid interface during water imbibition and primary drainage. By using contact angle measurements (section 1.6.1) the micromodels were concluded to be water-wet.

During the primary drainage and water imbibition qualitative measurements of the receding and advancing contact angle between the oil/water and water/CO₂, enabled the wettability of the micromodels to be estimated. The receding contact angle between the oil and water was measured during primary drainage. From **Figure 5.6.1** the receding contact angle is measured. The angle was measured to approximately 18°, thereby indicating a strongly water-wet model.

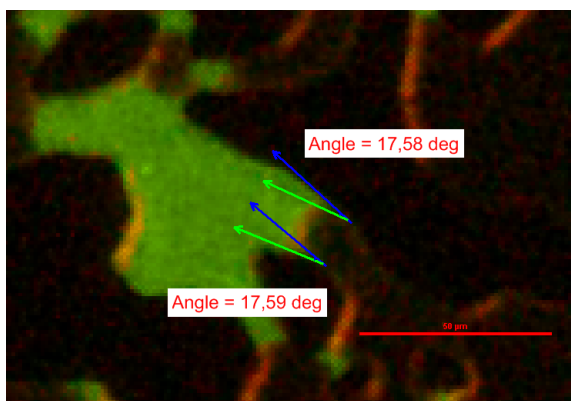


Figure 5.6.1: Receding oil-water contact angle measurements from primary drainage[28]

During spontaneous imbibition with Fluorescein water and CO₂, the advancing water-CO₂ interface was measured. From **Figure 5.6.2** the contact angles were measured to be approximately 78° and 73°. This indicated water being more wetting than CO₂.

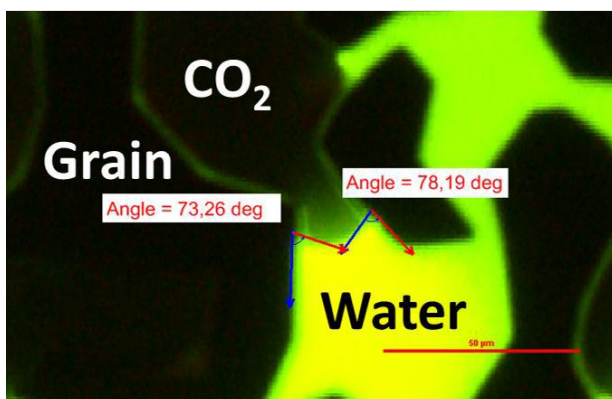


Figure 5.6.2: Advancing contact angle measurements during water imbibition in a CO₂-filled micromodel

6. High Pressure Silicon Wafer Micromodels

6.1 Permeability and Porosity

Permeability and porosity measurements and calculations were performed accordingly to the described procedure in section 4.3 and 4.4.

6.1.1 Permeability Measurements

Absolute permeability measurements for the high pressure micromodel B1 were done according to the procedure presented in chapter 4.3. **Figure 6.1.1** is a plot of the pressure for different injection rates as a function time. The rates used were 1.0, 2.5, 5.0 and 7.5ml/h, each over a period of 15 minutes.

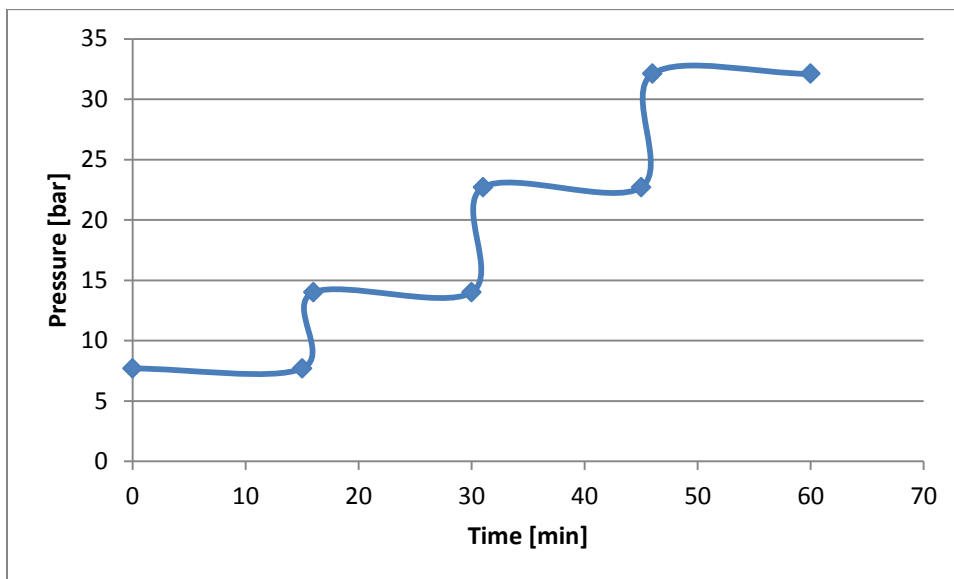


Figure 6.1.1: Pressure as a function of time at four different injection rates

After the different pressure for each injection rate was measured, the values were inserted in equation 1.2; Darcy's law. Table 6.1 displays the size measurements for the high pressure micromodel that were used to calculate the cross-section (A) and the length (L) in equation 1.2.

Table 6.1: Dimensions of the high pressure silicon wafer micromodel B1

Length [cm]	Width [cm]	Depth [cm]
3,6	1,3	0,002

SI units were used for the calculations, and the mean value provided a relatively accurate permeability value for the micromodel. The average permeability from the four rates resulted in absolute permeability of $847\text{mD} \approx 0.85 D \pm 0.05D$ for the high pressure micromodel B1.

Similar measurements were done for micromodel B3, with the rates of 10, 15 and 20ml/h. The permeability was calculated to be $877\text{mD} \approx 0.88D \pm 0.05D$. Micromodel B5-fracture was manufactured with a horizontal channel through the centre of the pore network, representing a fracture. The fracture would normally cause a much higher permeability, however this was not the case for model B5-fracture. The permeability calculation gave a similar permeability as other calculation and measurements done on the high pressure micromodels. This might be a result of the small scale of the model, providing an equal flow resistance throughout the model. In addition capillary forces in a water-wet model will drive water from the fracture to the matrix[43]. The pressures was measured at the same rates as model B3, giving a calculated permeability of $917\text{mD} \approx 0.92D \pm 0.05D$.

6.1.2 Porosity Measurements

The porosity measurements were done according to the descriptions in chapter 4.4. **Figure 6.1.2** displays a binary image converted from captured image of a fully water saturated micromodel. Four images was analysed using *Image J* and the mean porosity value of the pictures was used to determine the porosity of the micromodel.

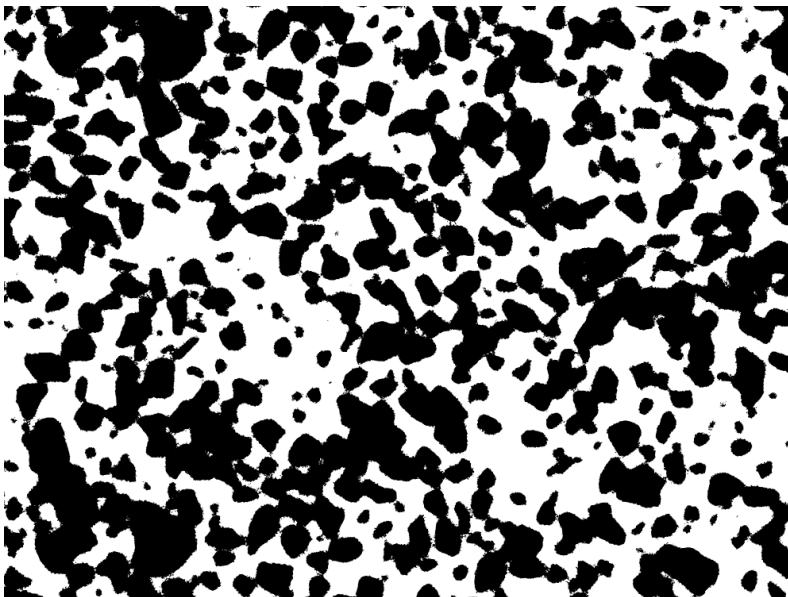


Figure 6.1.2: Binary image of micromodel B1 for porosity calculation in *Image J*

The porosity for the high pressure micromodel B1 was calculated to be 0.50 ± 0.05 . This was similar to the porosity of the low pressure micromodels. Both models were modelled after high resolution images of Berea sandstones, but did not have the same pattern. The high pressure micromodels were produced with a realistic pore network with rough grains (Figure 3.3.2b), while the low pressure models were produced with an idealized pore network with simplified, rounded grains (Figure 3.3.1a). From Figure 6.1.2 the binary conversion was observed to simplify the pore structure, which results in an uncertainty (see the appendix). Similar calculation on both model B3 and B5-fracture resulted in porosities of 0.52 ± 0.05 .

6.2 Primary Drainage

Primary drainage with oil/water was performed on the high pressure micromodels B1, B3 and B5-fracture. Displacement mechanisms were studied during the primary drainage process of model B1, while the irreducible water saturation (S_{iw}) was calculated for all the micromodels after the drainage processes were concluded. The upper right port was used as the injector and the lower left port as the producer, while the remaining two ports were closed. This boundary condition was used for all the experiments with the high pressure micromodels. The micromodel was initially saturated with 100% Fluorescein water. Due to photo bleaching green reflection was not observed through the blue light filter of the inverted microscope. The water appeared with a faded, brownish colour. N-decane with Nile Red was injected at the initial rate of 10ml/h. The oil reflected red light when visualized through the green filter and appeared yellow/orange through the blue filter.

When initiating the experiment the threshold pressure was observed to be higher, compared to the observed threshold pressure for the low pressure micromodels. This was expected due to the smaller dimension of the high pressure micromodels. The capillary, threshold pressure increases as the radius of the pores and pore throats are reduced. Oil was injected with a rate of 10ml/h and the pressure increased to 4.7 bars before decreasing to 2.3 bars, indicating a threshold pressure of 4.7 bars \pm 0.5 bars during primary drainage. No oil entered the pore network before the threshold pressure was reached.

Figure 6.2.1a and b displays two displacement mechanisms observed during primary drainage, film flow and piston displacement represented by Haines' jump. The increasing oil pressure forced the water to evacuate the pore through film flow. The Haines' jump event observed was of water displacing oil, thereby indicating two-phase, double displacement. Water was observed to displace the oil, even though the oil was the only fluid injected. The water was most likely trapped with no possible escape path for film flow. As the phase pressure of water increased, the oil was displaced through a piston-like displacement as the water imbibed into oil-filled pores.

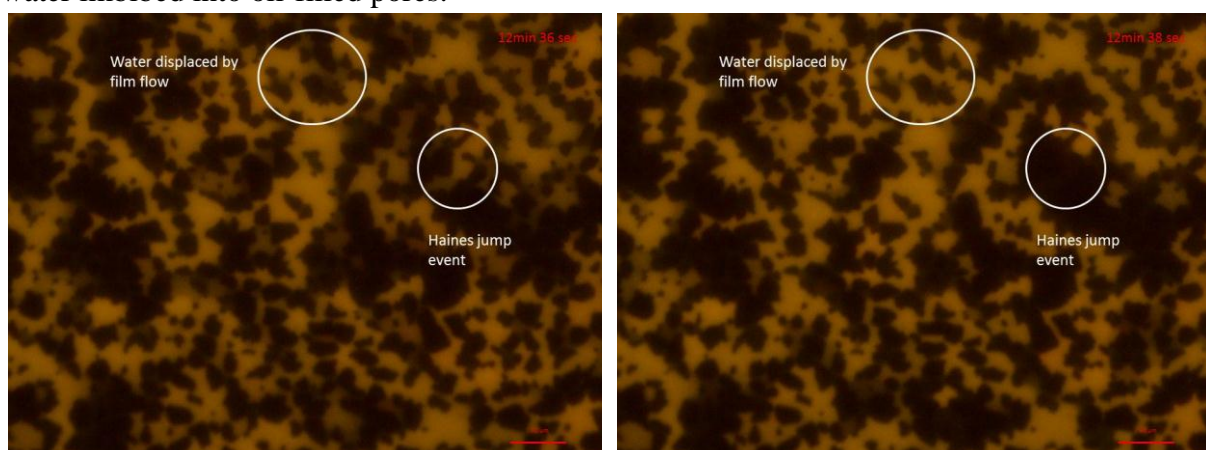


Figure 6.2.1a & b: Film flow and Haines' jump during primary drainage; (a) water within the oil phase is slowly drained through film flow in the upper circle, (b) oil is displaced by water (double displacement) resulting in a Haines' jump

Numerous piston-like displacement events were observed and captured, as can be seen in **Figure 6.2.2a and b**. Three circles mark displacement events where oil displaced water in a piston-like manner. The ellipse mark oil being redistributed after a Haines' jump in Figure 6.2.2b.

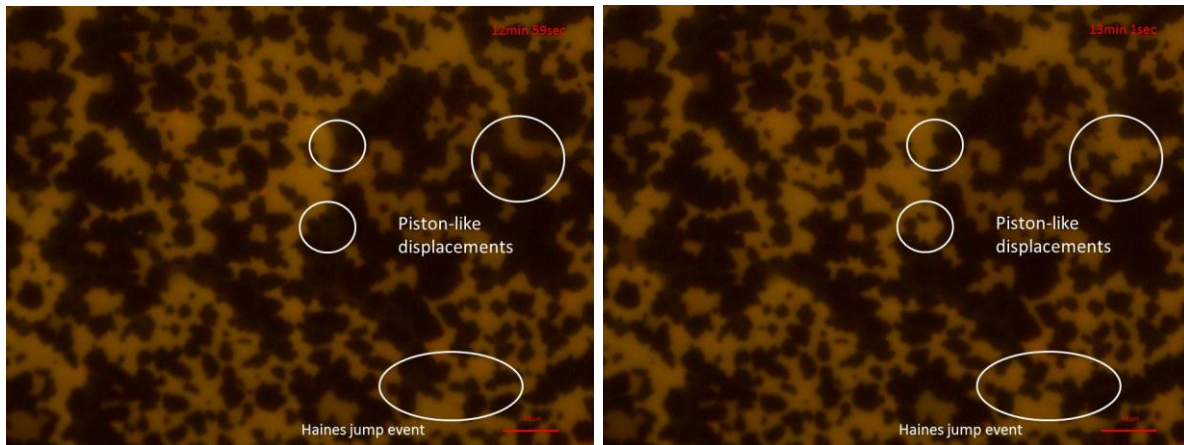


Figure 6.2.2a & b: Piston-like displacement and Haines' jump during primary drainage; three piston displacement where oil displaces water, and a Haines' jump resulting in a redistribution of fluids in the marked ellipse (b)

The flow was observed to be stable for the injection rate of 10ml/h. Similar to the results for the low pressure micromodel, the high rate resulted in a high differential pressure across the matrix and a stable flow. The high rate(10ml/h) was suspected to increase the viscous forces that were further balancing the effect of capillary forces, resulting in stable flow conditions. Increasing the injection rate further (25ml/h) resulted in more unstable flow. After the primary drainage processes the irreducible water saturation was calculated using the method described in section 4.4. This gave $S_{iw} = 0.08 \pm 0.05$ for model B1 and $S_{iw} = 0.07 \pm 0.05$ for model B3. The fractured model B5-fracture had a higher irreducible water saturation of $S_{iw} = 0.14 \pm 0.05$, caused by water accumulating on the left side of the micromodel.

Discussion Primary Drainage

The flow and displacement during primary drainage for the high pressure silicon wafer micromodels were observed to be similar to the low pressure micromodels. Regular piston displacement, Haines' jump, film flow and two-phase, double displacements were observed during the primary drainage experiments. The flow was observed to be initially stable at a low injection rate (10ml/h), and increasing unstable with an increased injection rate (25ml/h). After oil breakthrough in the production channel the displacement of water slowed down, increasing the injection rate kept the displacement of water going. The high pressure specifications of the high pressure micromodels enabled high injection rates and low water saturations values were therefore obtain after a period of time.

Water was observed to accumulate in the fracture close to the production port, as oil migrated through the pore network towards the producer without displacing the accumulated water. This resulted in the irreducible water saturation being higher for the fractured micromodel B5. Restarting the drainage process at the same injection rate did not displace more water, which was similar to the results for the low pressure micromodels, where no water was displaced after oil breakthrough.

Secondary Water Injection

After the primary drainage process on micromodel B1, secondary water injection was initiated. The experiment was conducted to evaluate if the pressure limitation was responsible for the low oil recovery during secondary water injection of the low pressure micromodels. The recovery was therefore expected to be higher for the high pressure model compared with the low pressure model.

Water with Fluorescein was injected at an initial rate of 10ml/h before being increased to 25ml/h. The saturation of oil after the primary drainage was 0.92 and the purpose of the water injection was to increase the recovery greater than 5%. Water was injected over a period of 47 minutes and saturation calculations were conducted through *Image J*. The average saturation calculations provided an oil saturation of $S_o = 0.73 \pm 0.05$ after secondary water injection. The recovery factor was calculated to be 21% ± 5% of the OOIP. The result supports the explanation given for the low pressure micromodels. Higher recovery was expected given a longer period of injection, as displacement of oil was observed even after water breakthrough. The recovery from water injection was expected to be improved given stable flow regimes at lower injection rates.

6.3 Three-Phase CO₂ Gas Injection

Secondary Three-Phase CO₂ Gas Injection B5-fracture

Three-phase CO₂ injection was conducted on the high pressure micromodel B5-fracture. CO₂ was injected after the primary drainage process, and a section including the fracture was studied at the magnification of 10X zoom. The experiment was performed as preparation for the liquid CO₂ experiment. The valve connecting the cylinders in the pump was closed and the gas flowed from cylinder A through the system and into cylinder B (Figure 3.1b). The system was pressurized gradually by the connected CO₂ tank, and the pressure was monitored through the pump software on the computer. Before the experiment the pump system was recalibrated, thereby enabling accurate differential pressure monitoring

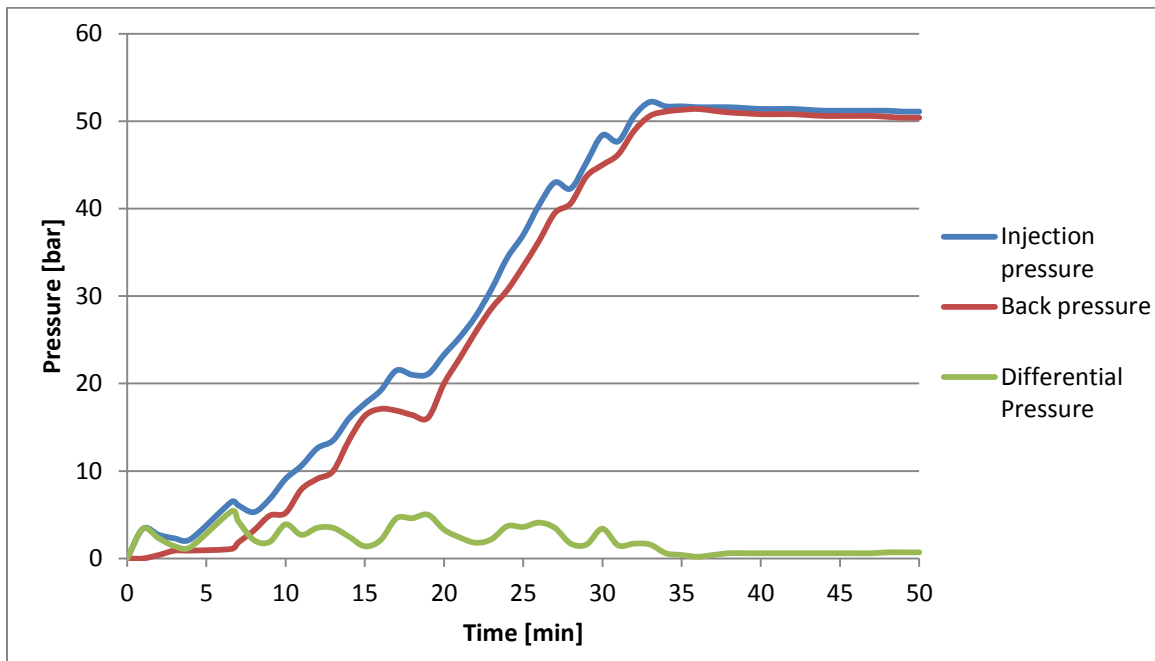


Figure 6.3.1: Pressure as a function of time during secondary CO₂ gas injection

Figure 6.3.1 displays the monitored pressure during the experiment, where the pressure differences indicate the differential pressure over the micromodel. The pressure was increased from ambient pressure to 50 bars, which was the maximum pressure the CO₂ tank could deliver. The differential pressure was kept below 5 bars during the pressure build-up, as can be seen from the green graph in Figure 6.3.1. Displacement mechanisms and flow were studied and similar observations as with the low pressure silicon wafer micromodels were made.

Initially the fracture was filled with oil, and the injected CO₂ displaced the oil through the fracture. The oil was visualized as both yellow and brownish, depending on the extent of illumination contributing to photo bleaching. The water was strongly affected by photo bleaching and appeared dark brown, which sometimes made it hard to distinguish the water phase from the CO₂ phase. A section to the right of the micromodel by the fracture (close to the injection port) was studied.

Capillary oil fingering was observed normal to the direction of flow, as can be seen from **Figure 6.3.2a**. The oil were displaced in a piston-like manner though the fracture before CO₂ breakthrough. **Figure 6.3.2b** displays the fracture flow after CO₂ breakthrough. The CO₂ flowed rapidly and straight through the fracture, as the oil flowed slower along the matrix and was displaced into the matrix.

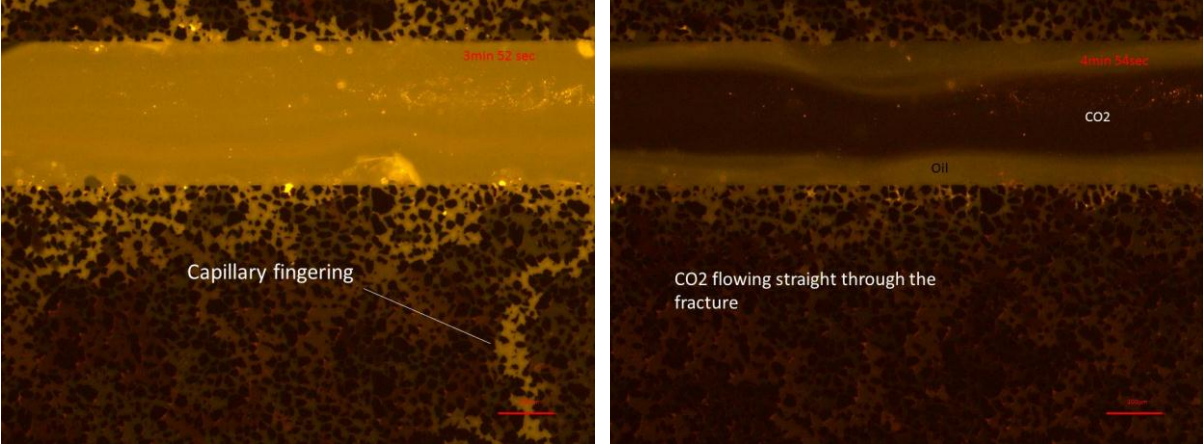


Figure 6.3.2a & b: Capillary finger and flow in the fracture; (a) a capillary oil finger enters the matrix from the fracture, normal to the direction of flow. (b) CO₂ flows straight through the fracture displacing oil towards the matrix

CO₂ eventually entered the matrix and displaced the oil. The oil was displaced both towards the fracture and towards the production port. Discontinues droplets of oils were observed to flow in the CO₂ phase in the fracture after approximately 7 minutes of injection (**Figure 6.3.3a**). As more oil was displaced into the fracture a spreading layer of oil on the fracture wall was observed (**Figure 6.3.3b**). The spreading oil layer was displaced slowly through film flow.

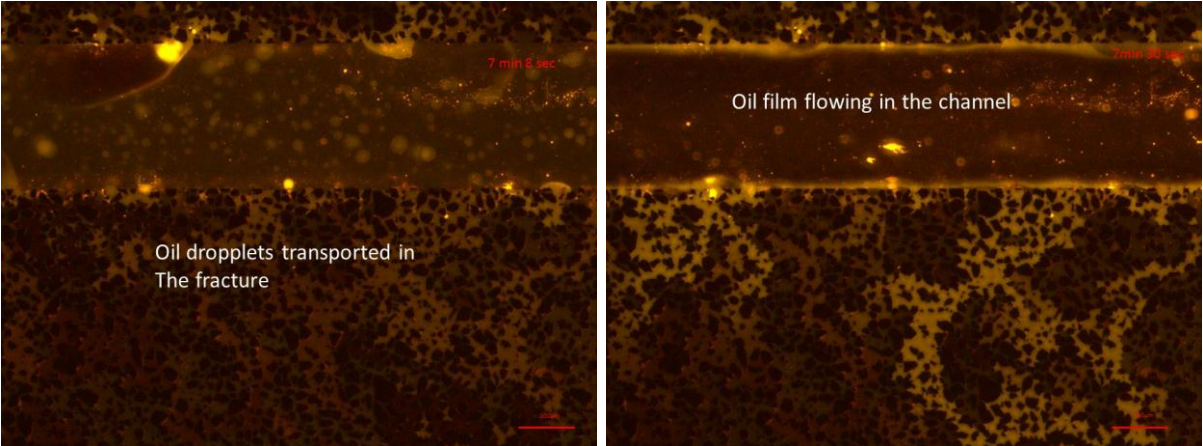


Figure 6.3.3a & b: Flow in fracture; (a) oil droplets were transported within the CO₂ in the fracture, (b) oil is displaced towards the fracture and flow through the fracture in films on the fracture wall

Multiple piston-like displacement events were observed throughout the matrix. Retention of Nile Red and Fluorescein was observed in the fracture, and accumulated in the fracture and on the matrix wall before slowly being displaced. From Figure 6.3.4a & b a large and small piston displacement were observed. The CO₂ displaced oil through a Haines' jump and the oil was redistributed in several pores (Figure 6.3.4b). To the right in Figure 6.3.4a and b a single oil-filled pore was gradually displaced by CO₂ through a piston-like displacement.

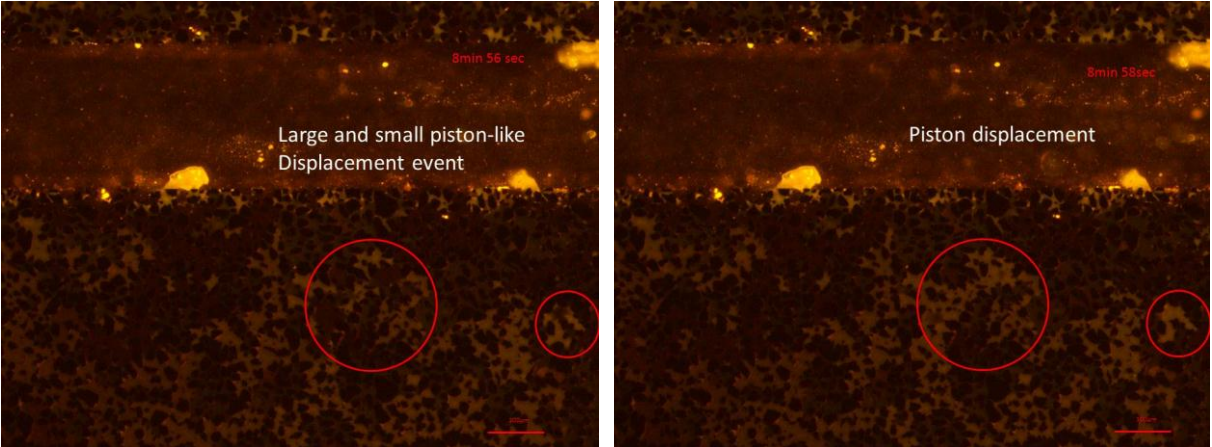


Figure 6.3.4a & b: Piston-like displacements; In the large circle oil is displaced through Haines' jumps(a) and redistributed in several pores(b), the small circle captures a piston-like displacement advancing in a single pore

After approximately 11 minutes of injection, oil was observed to be mobilized towards the fracture from the upper side of the fracture. The dominating phase flowing in the fracture changed from CO₂ to oil (Figure 6.3.5a). The mobilized oil were initially displaced through the fracture, before the more mobile and less viscous CO₂ gas broke through and displaced the oil through the matrix. From Figure 6.3.5b CO₂ breakthrough is observed as oil is displaced towards the fracture wall and into the matrix.

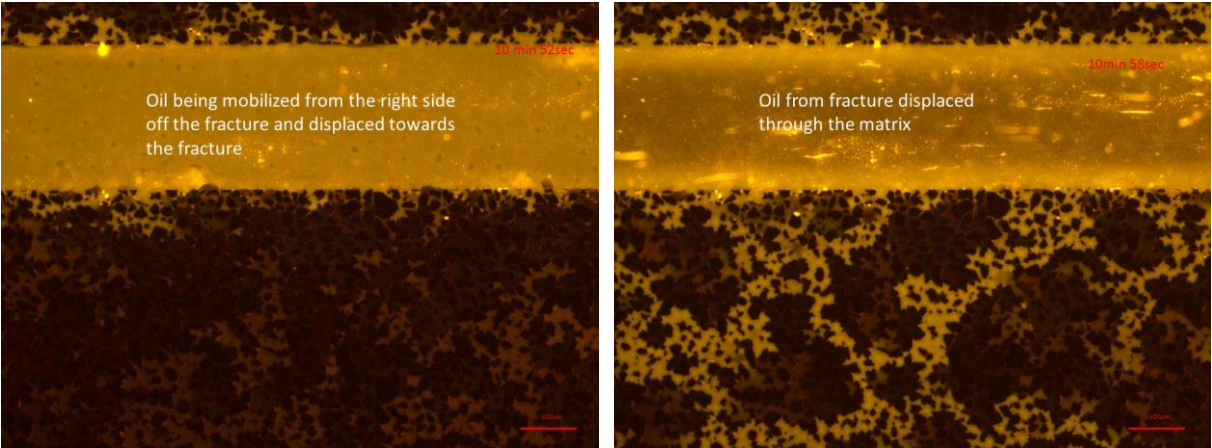


Figure 6.3.5a & b: Mobilization of residual oil; (a) oil is mobilized towards the fracture from the upper part of the micromodel, and is displaced through the fracture, (b) CO₂ breaks through the oil-filled fracture and oil is displaced into the matrix

Both film flow and Haines' jump were observed in the matrix. Spreading layers of oil was displaced by CO₂ and through film flow. From **Figure 6.3.6a and b** Haines' jump as CO₂ displaced oil, and water film flow within the oil phase was captured. Water being the wetting phase, was observed in a single pore surrounded by oil and on the pore walls in oil-filled pores (Figure 6.3.6a). The water was displaced slowly through film flow and fast through multiple displacements, where CO₂ displaced oil which in turn displaced water. Oil was observed to be displaced by both water and CO₂, while the water mainly was displaced by oil through multiple displacements.

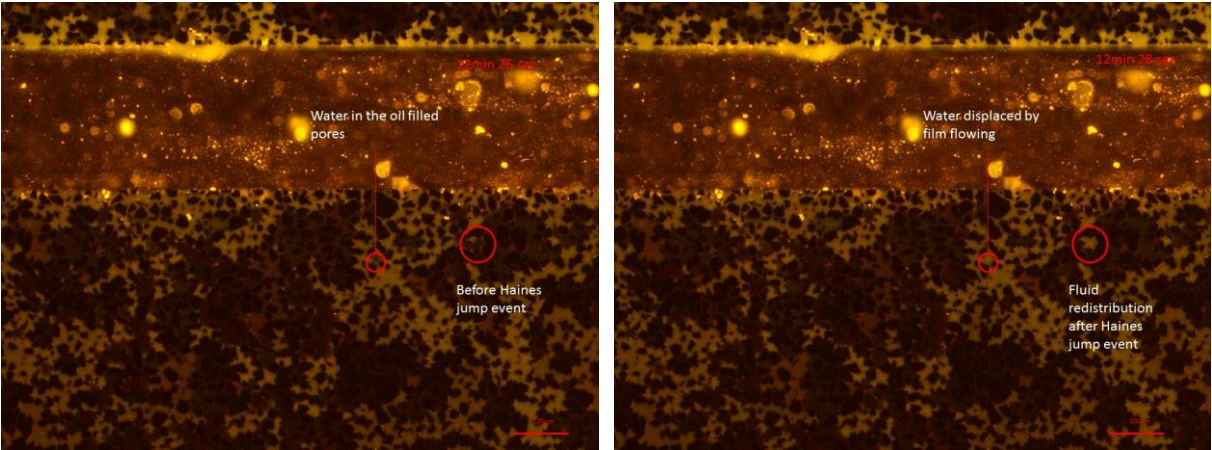


Figure 6.3.6a & b: Haines' jump and film flow; (a) water is observed in a pore surrounded by oil, (b) the water is gradually displaced through film flow. Oil is redistributed in the right circle after a Haines' jump

The oil was more rapidly displaced by the CO₂ throughout the matrix as the pressure increased. In **Figure 6.3.7a and b** a capillary oil finger is rapidly displaced by CO₂ and small piston events are observed. The images are captured every 2 seconds, and after two seconds most of the oil finger was displaced by CO₂ towards the production port in the lower left corner.

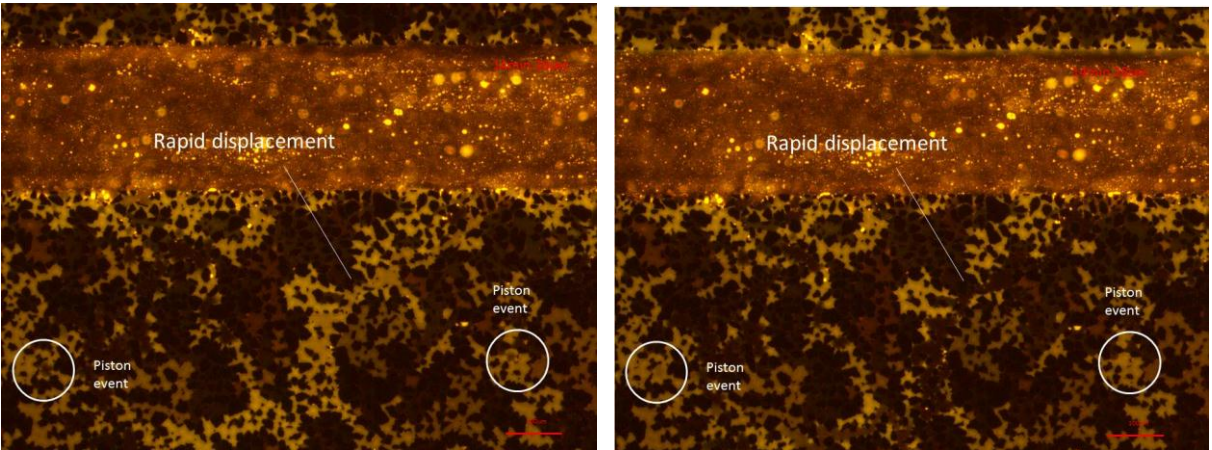


Figure 6.3.7a & b: Rapid displacement and Piston events; (a) oil is the displaced through piston displacement in the two circles, (b) a large oil finger is rapidly displaced

The pressure was increased until a pressure of 50 bars was reached. Images were captured from four sections in the model so that saturation calculations could provide an estimated recovery. The recovery was calculated to be $63\% \pm 5\%$ for three-phase CO₂ gas injection in the high pressure micromodel B5-fracture after 50 minutes of injection.

Discussion Three-Phase CO₂ Gas Injection

The experiment with secondary CO₂ gas injection in the high pressure micromodels was compared with the experiments on the low pressure models. The increase in pressure was still below the minimum miscibility pressure (*MMP*) for CO₂ and n-decane, and an immiscible displacement was therefore expected. Similar displacement mechanisms were observed for the high pressure micromodels as for the low pressure micromodels. Snap-off events, piston displacement, and film flow of water films and spreading layers of oil were observed. Small snap-off events were observed without great extent of gas expansion following. The magnification used to study the gas injection made it hard to identify small scale pore-filling and displacement mechanisms. Gas expansion was therefore expected to be present without being a dominating method of displacement.

By studying an area including both the fracture and the matrix, the effect of diffusive processes could be studied. Without the present of diffusive processes, at low differential pressure conditions, the gas would flow straight through the fracture and towards the producer, without mobilizing and producing oil and water. The production of water and oil resulting in lower oil saturation was therefore an indication of diffusion being present. The effect of diffusive processes was directly observed in Figure 6.3.2a and 6.3.7b. In the first figure high concentrations of oil was flowing through the fracture and being displaced through the matrix, and in the second figure CO₂ in the fracture rapidly displaced oil in the matrix. Spreading layers of oil were less observed than water films, as oil was mostly displaced instantaneous through piston-like displacements. The flow in the matrix appears chaotic with great variations of flow direction and displacement. Diffusive processes drove oil and CO₂ from the fracture and into the matrix. At the same time the presence of both displacement mechanisms and capillary forces, drove fluids towards the fracture.

The recovery was calculated from saturation measurements from captured images, taken after 50 bars pressure was reached. Retention of Nile Red and Fluorescein provide a great error when applying colour threshold to the images. From Figure 6.3.7a and b small accumulations of retention of Fluorescents were observed through the entire fracture. The fracture was assumed to be completely gas-filled, and images were captured in section with low accumulations of Fluorescents retention, to minimize the error. The residual oil saturation after the secondary CO₂ gas injection was calculated to be $S_o = 0.32 \pm 0.05$. This provided a recovery factor of $63\% \pm 5\%$. Greater recovery was expected giving a longer period of injection as displacement and flow were observed after the system reached a constant pressure of 50 bars.

6.4 Three-Phase Liquid CO₂ Injection

Tertiary Liquid CO₂ Injection Model B5-fracture

After the experience with secondary liquid CO₂ injection (chapter 6.5), the experimental setup was altered so that experiments with tertiary liquid CO₂ could be studied. An additional CO₂ tank and another Quizix pump system were connected to the SP-pump (see Figure 3.1b). The connection between cylinder A and B in the original pump system was closed, thereby permitting flow through the micromodel. This enabled us to monitor the differential pressure, given by the difference between the pressure in cylinder A and cylinder B (injection and back pressure). The additional pump system and CO₂ tank were used to build up the pressure, and the pressure was gradually increased while the differential pressure was kept under 5 bars. During the pressure build-up process, secondary CO₂ gas injection for the high pressure micromodel was studied, and the result was presented in the previous chapter (6.3). The pressure was increased to 50 bars by the CO₂ tank and an additional 5 bars by the extra CO₂ tank. Water was injected into the extra tank to increase the pressure to approximately 82.5 bars. **Figure 6.4.1** displays a graph where time is plotted against the injection pressure and back pressure during the experiment with liquid CO₂ injection. The differential pressure is reflected by the green graph.

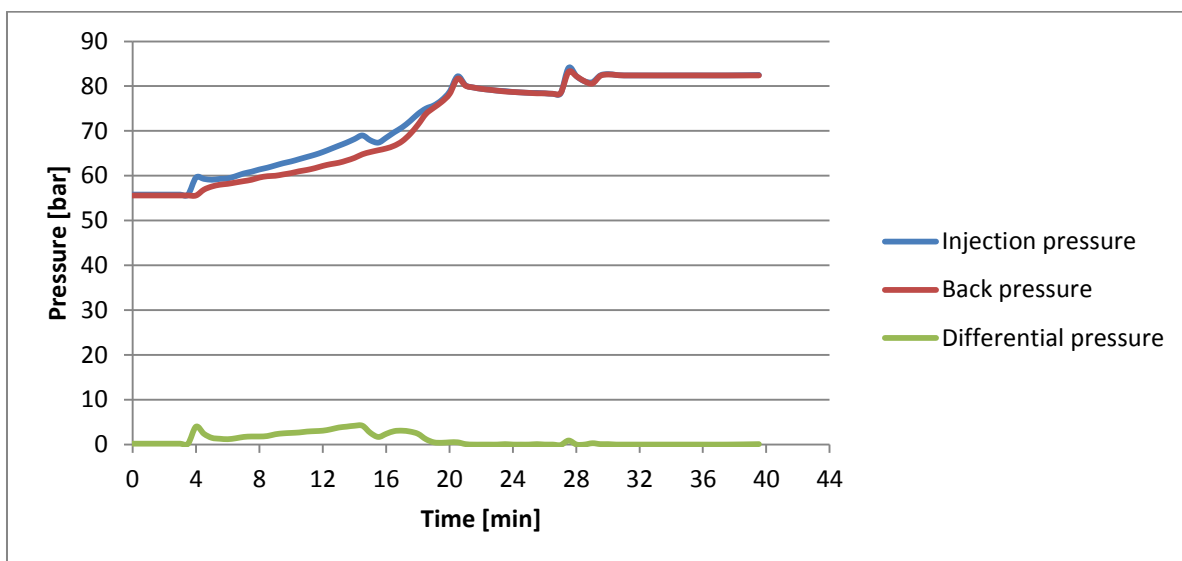


Figure 6.4.1: Pressure as a function of time during liquid CO₂ injection

At a constant temperature of 23 °C CO₂ gas turns to liquid at approximately 61.4bars[29], and recordings were therefore initiated at 60 bars pressure. To achieve and study miscibility, the pressure was increased to approximately 82.5 bars. From the graph in Figure 6.4.1 an increase in differential pressure is observed at approximately 60 bars. The change of state from gas injection to liquid injection causes the pressure to increase by the injection port, while the pressure at the production ports increases at a slower rate. At approximately 75 bars the system reaches equilibrium with low differential pressure over the micromodel, and liquid CO₂ is being produced.

No clear changes in flow were observed in the fracture when liquid CO₂ was injected, due to the retention of Nile Red and Fluorescein in the fracture. Initially a large viscous finger developed parallel to the direction of flow. **Figure 6.4.2a-d** displays oil being mobilized from the right side of the micromodels and developing into a viscous finger. The large viscous finger was gradually displaced by liquid CO₂ in the direction of flow.

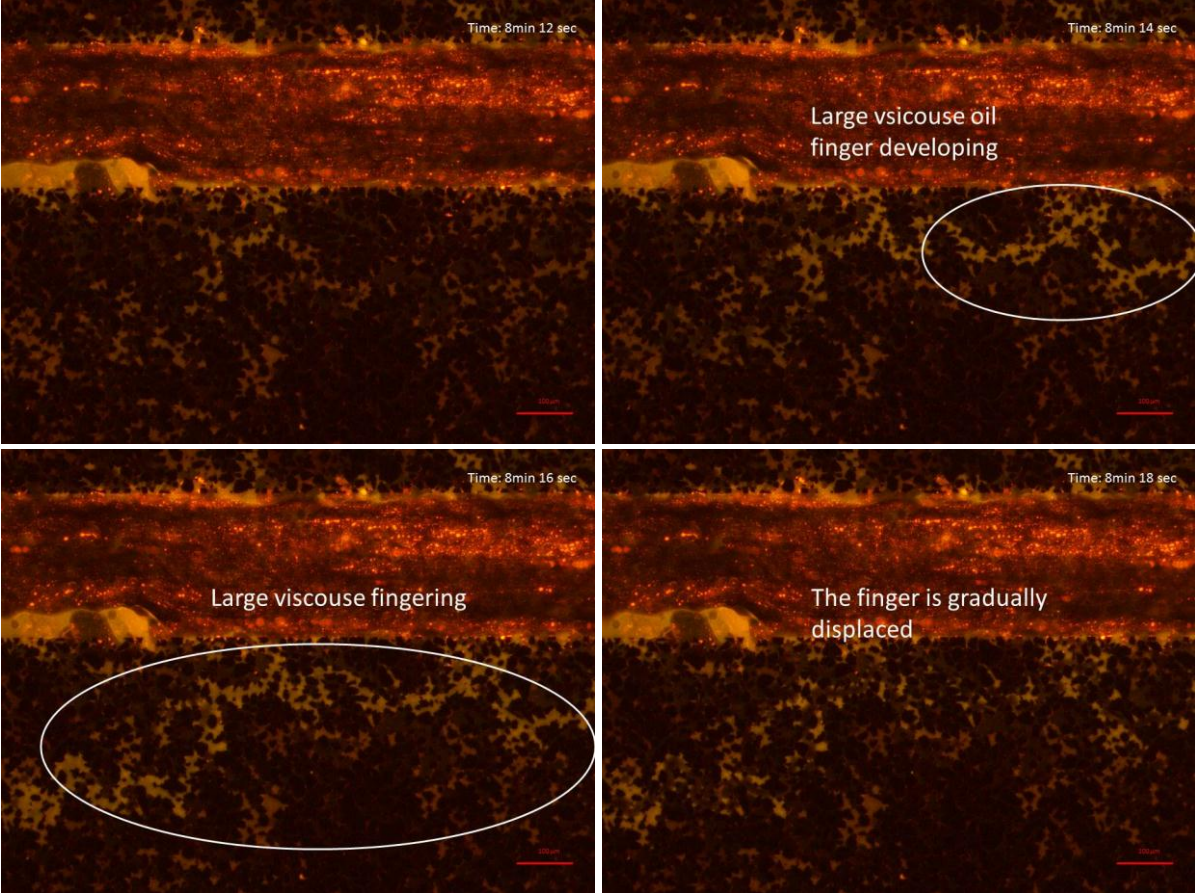


Figure 6.4.2a, b, c & d: Large viscous oil finger; a large viscous oil finger develops (b), parallel to the flow in the fracture and is displaced by liquid CO₂ through piston displacement (d).

As for the gaseous CO₂ injection into the fractured micromodel, a variation of flow was observed; both stable and unstable flow regimes. From the dotted white line in **Figure 6.4.3a** a stable interface between liquid CO₂ and the oil phase was observed. The CO₂ initially displaced the oil counter-currently with a stable radial front towards the fracture (**Figure 6.4.3b**), before the front became unstable and rapidly displaced the oil. Similar to CO₂ gas injection piston displacement, multiple displacements and film flow of both spreading oil layers and water films were observed before miscibility was achieved.

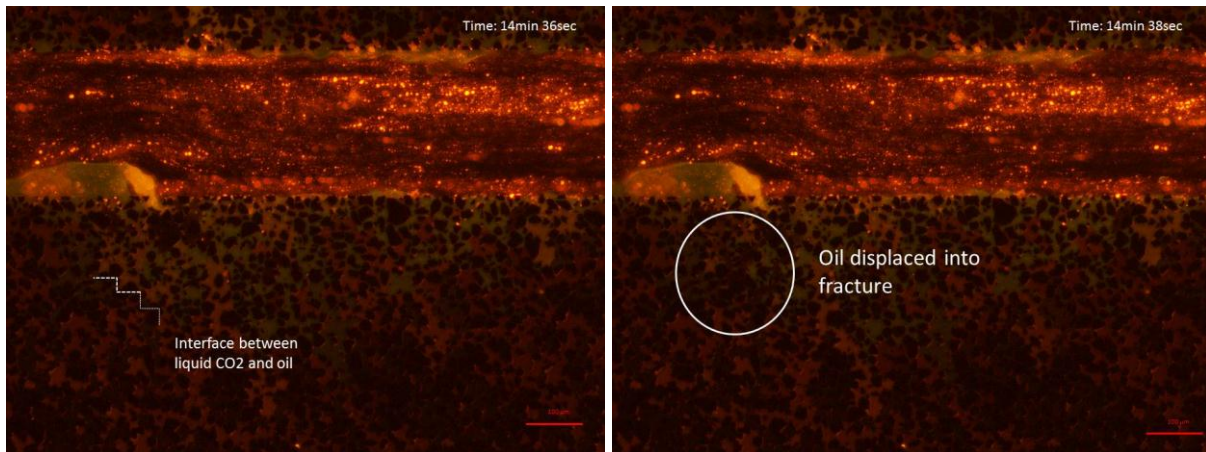


Figure 6.4.3a & b: CO₂ front displacing oil towards fracture; (a) a sharp interface between liquid CO₂ and oil is marked with dotted white lines, (b) the liquid CO₂ displace the oil towards the fracture

The liquid CO₂ was observed to mobilize and produce residual water. From **Figure 6.4.4** water with Fluorescein was observed. The liquid CO₂ mobilized water from far ends of the micromodel which had been less illuminated and the effects of photo bleaching were minor, indicated by a green phase flowing through the studied section. The liquid CO₂ was also observed to displace accumulations of both Nile Red and Fluorescein retentions on the pore walls in the matrix. The accumulated Fluorescents in the fracture were however not displaced, as can be viewed in the Figure 6.4.4.

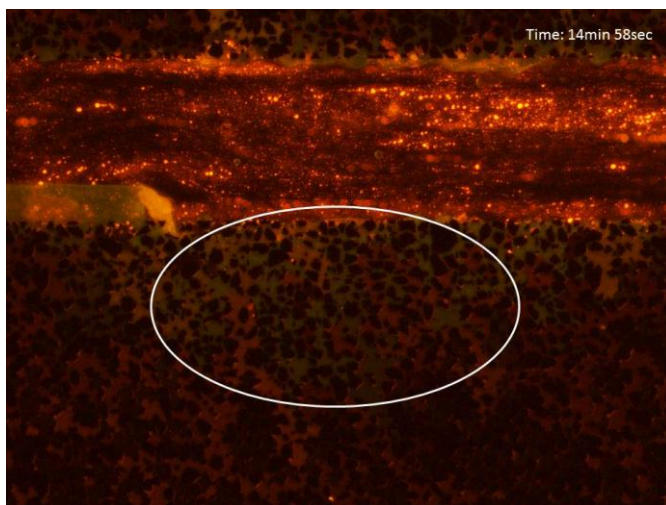


Figure 6.4.4: Mobilization of water and Fluorescein retention

Miscibility was observed when the pressures were increased to approximately 82 bars, resulting in a miscible phase of oil and CO₂. Small miscibility events were observed in **Figure 6.4.5a and b**, while a liquid CO₂ front displaced oil towards the fracture in the lower area of the figure. The miscible phase was observed to displace both oil and water through piston events and multiple displacements.

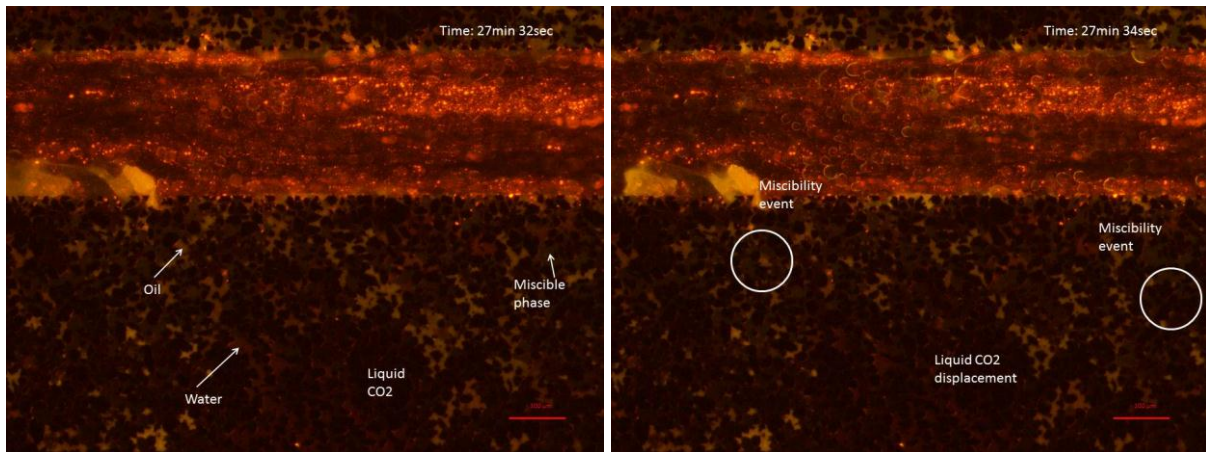


Figure 6.4.5a & b: Miscibility between oil and CO₂; miscibility between oil and CO₂ is observed in the two circles, while a front of liquid CO₂ displace oil towards the fracture

Identifying the miscible phase and distinguishing the miscible phase from the oil phase was often challenging. The blue light filter on the microscope enabled us to distinguish between the oil, water and CO₂ phase, while the miscible phase was difficult to observe. The magnification was increased to 20X zoom and the bright light filter was selected. Images were captured with the bright light filter, before the light filter was changed to the green light filter. **Figure 6.4.6a and b** displays an image taken at 20X zoom with the bright light filter, and an image taken with the green light filter 4 seconds later. The miscible phases were observed to have a dark interface often with small bubbles attached to the surface. In Figure 6.4.6a two minor and one large miscible phase were observed, and through the green light filter in Figure 6.4.6b the phase was observed to reflect red light thereby indicating the present of oil. The bright light filter was then applied again to observe the position of miscible phases and to ensure that the miscible phases were still present in the oil phase, thereby indicating miscibility. A section with relatively stagnate flow was selected to ensure accurate identification of the miscible phase.

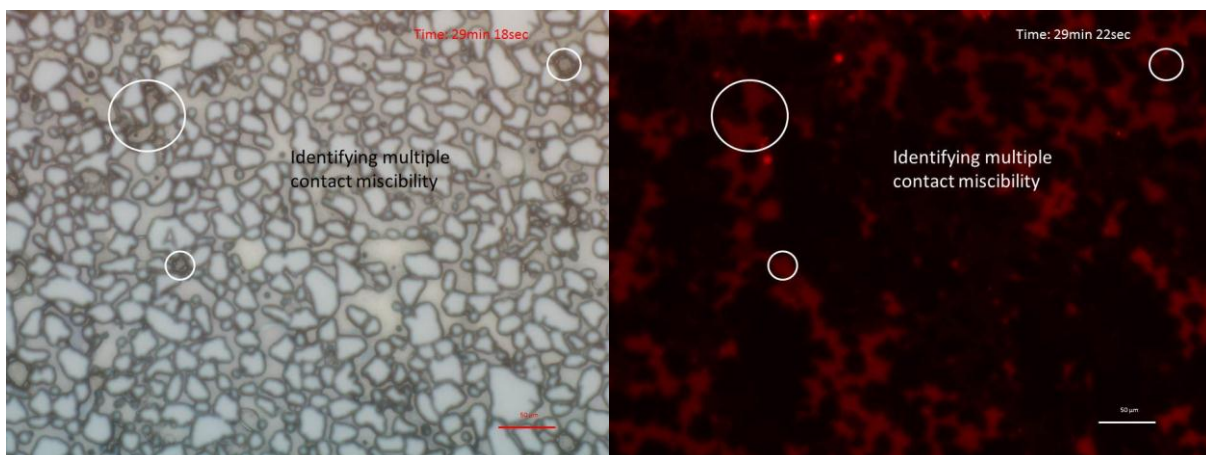


Figure 6.4.6a & b: Identifying the miscible phase; (a) two small and one larger miscible phase is observed through the bright light filter, (b) the same phases reflect red light when the green light filter is applied, indicating the present of oil.

With the selected light filter and magnification lens, liquid “bubbles” of CO₂ were observed to dissolve and mix in the oil phase. This was observed in **Figure 6.4.7a and b** where a small liquid CO₂ bubble shrinks and is gradually dissolved in the oil phase, creating a first contact miscible event. The interfacial tension between the oil and CO₂ phase is reduced towards zero, resulting in miscibility.

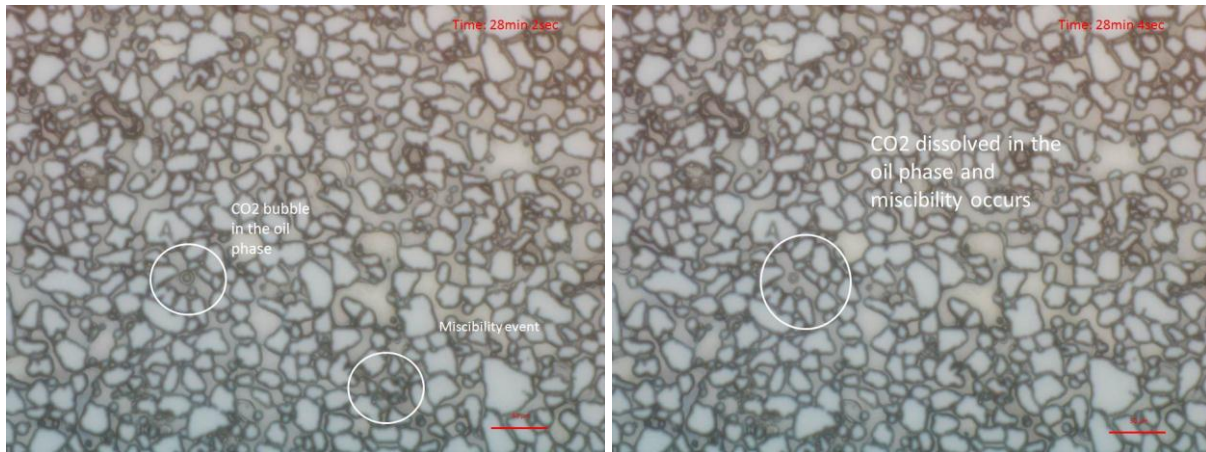
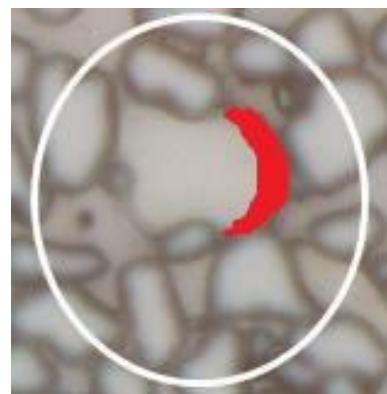


Figure 6.4.7a & b: CO₂ dissolving in the oil phase; (a) bubbles of liquid CO₂ is observed within the oil phase, (b) the bubbles dissolve in the oil phase, indicating miscibility

In **Figure 6.4.9a** the different fluid phases are labelled on an image captured through the bright light filter with 20X zoom magnification. The phases were labelled by applying both the green and the blue light filter to the same section. From **Figure 6.4.9b-d** swelling of the oil phase was observed. The sharp interface of the oil slowly advances, reflecting the increase in volume from the oil swelling. From the upper circle of figure b and c flow of the miscible phase was observed. In the same two figures Haines’ jump was observed in the lower left corner, as a stable miscible interface made a jump and completely displaced the oil before stabilizing. A miscible displacement event was observed from figure c to d. The miscible phase displaces oil in a piston-like manner through multiple displacements. The volume of the miscible phase was also observed to increase, thereby indicating first contact miscibility. **Figure 6.4.8** displays the swelling of the oil phase causing an increase in volume. The figure was made by combing Figure 6.4.9b and d, where the red marking represent the increase in volume from figure b to d.

Figure 6.4.8: Oil swelling; the red section represents the increase in volume of the oil phase marked to the left in Figure 6.4.9 b & d. Over a period of 4 seconds the volume is increased, thereby indicating oil swelling.



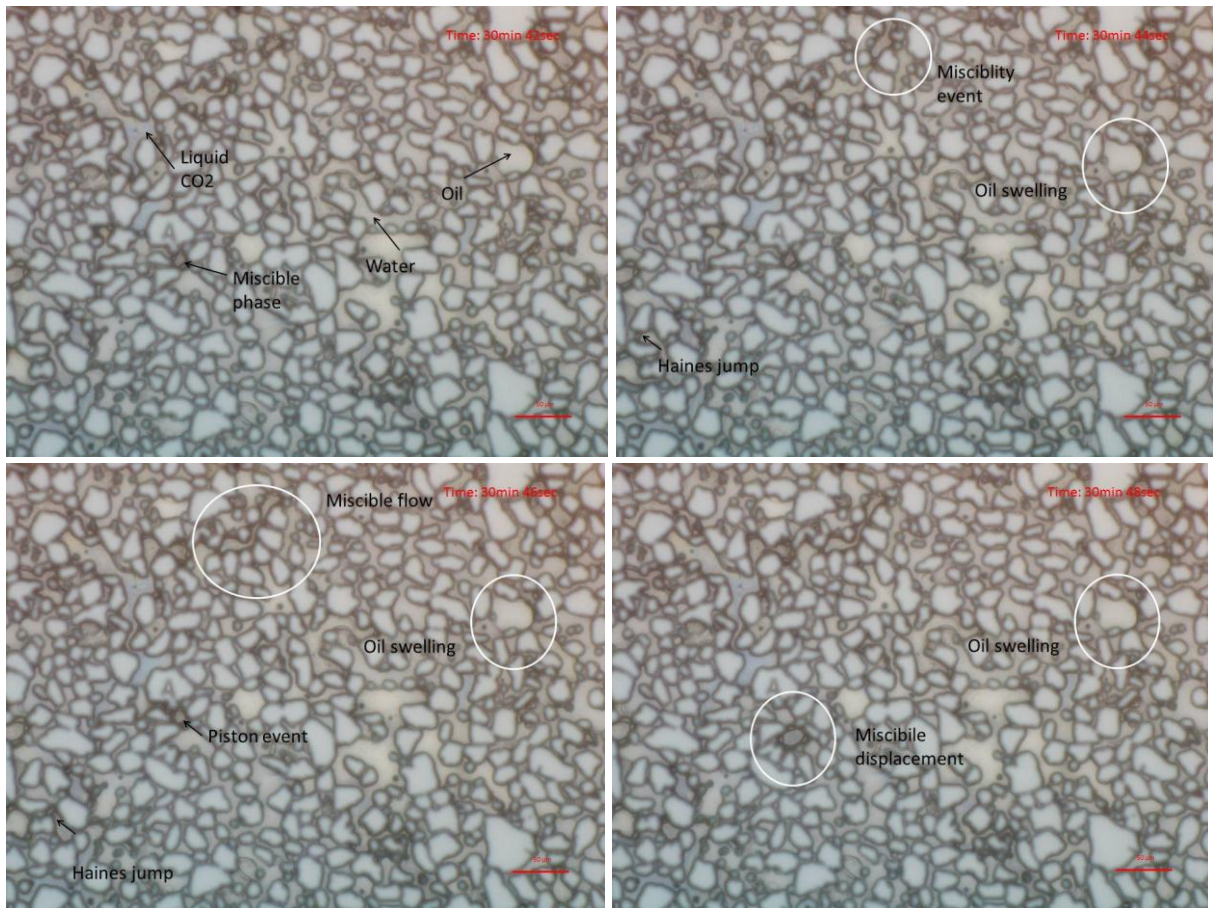


Figure 6.4.9a, b, c & d: Displacement and oil swelling; miscible displacement is observed from (b)-(c) in the upper circle and from (c)-(d) where a miscible phase displace oil through a piston-like displacement. Haines' jump is observed in the lower left corner from (b)-(c) where a miscible phase displaces water. Oil is observed to swell from (b)-(d).

Liquid CO₂ was injected over a period of approximately 40 minutes, before the pressure was safely decreased. Saturation calculations were performed after the pressure was reduced to ambient pressure, and the recovery was calculated from four sections in the micromodel. The average oil recovery was calculated to be $82\% \pm 5\%$, providing an increase in recovery of 19% from secondary CO₂ gas injection to tertiary liquid CO₂ injection.

Discussion Liquid CO₂ Injection Model B5-fracture

During liquid CO₂ injection increased oil recovery was observed and calculated (19%). Change of CO₂ state was observed in the pressure interval of 61-62 bars. As CO₂ becomes liquid the volume decreases, while the density and viscosity increases (Figure 6.6.1). From equation 1.7.1 the increase in viscosity will result in a reduced mobility and from equation 1.7.2 the mobility ratio will thereby be reduced. Reducing the mobility ratio towards and below unity ($M \leq 1$) will result in a more favourable mobility ratio and a stable front will thereby provide a good sweep[20]. The liquid CO₂ was observed to flow in the same manner as gaseous CO₂, being affected by diffusion and flowing from the fracture and into the matrix. The CO₂ displaced the oil through piston displacement and film flowing of spreading oil layers.

Miscibility was achieved as the pressure was increased to approximately 82 bars. Minimum miscibility pressure measurements on CO₂ and n-decane using slim tube and rising-bubble apparatus have provided a MMP of 88.3 bars at 37.7°C[44]. The MMP decreases with decreased temperature, and achieving miscibility at approximately 82 bars at 23 °C is therefore possible. The interfacial tension between oil and CO₂ is reduced towards zero, resulting in miscibility. Reducing the interfacial tension will increase the capillary number (equation 1.4.4 and Figure 1.4.3) and contribute to an improved microscopic sweep. The miscible CO₂ causes the oil to swell, increasing the oil density and volume, and reducing the oil viscosity[4]. First contact miscibility between oil and liquid CO₂ was observed through the bright light filter and confirmed through the green light filter. The miscible phase was observed to displace oil through piston displacement and multiple displacements.

The oil recovery was calculated to be 82% ± 5% and a higher recovery was expected given a longer period of injection. The recovery was calculated after depressurizing the experimental setup. Displacement and production of oil was observed during this process (see solution gas drive experiment) and the calculated recovery was therefore greater. The liquid CO₂ injection experiment was concluded before 100% recovery was achieved so that vaporization of CO₂ and possible solution gas drive could be observed. The result and discussion for that experiment is presented in the next two sections. The decrease in volume of swelled oil and continuous displacement during the vaporization process, results in a greater estimated recovery.

Solution Gas Drive during Depressurization of CO₂

After the experiment with liquid CO₂ was conducted, the experimental setup was pressurized at approximately 82 bars. The pressure was gradually reduced as solution gas drive was studied. The gradually decline in pressure is displayed from the graph in **Figure 6.4.10**. During the depressurization process both the liquid CO₂ phase and the miscible phase was studied at 20X zoom. This was done to investigate the change of state for CO₂ and the change in oil composition at declining pressure.

Using the different light filters on the microscope both the oil phase and the miscible phase could be identified at approximately 82 bars. The pressure was gradually lowered using the Quizix QX pump system to depressurize the experimental setup. A section on the lower right side of the micromodel was studied with the bright light filter. As the pressure decreased and came close to 60 bars, change of CO₂ state and change of oil composition was observed. From Figure 6.4.10 an increased differential pressure is observed between 70 and 60 bars, indicating change of CO₂ state and oil composition.

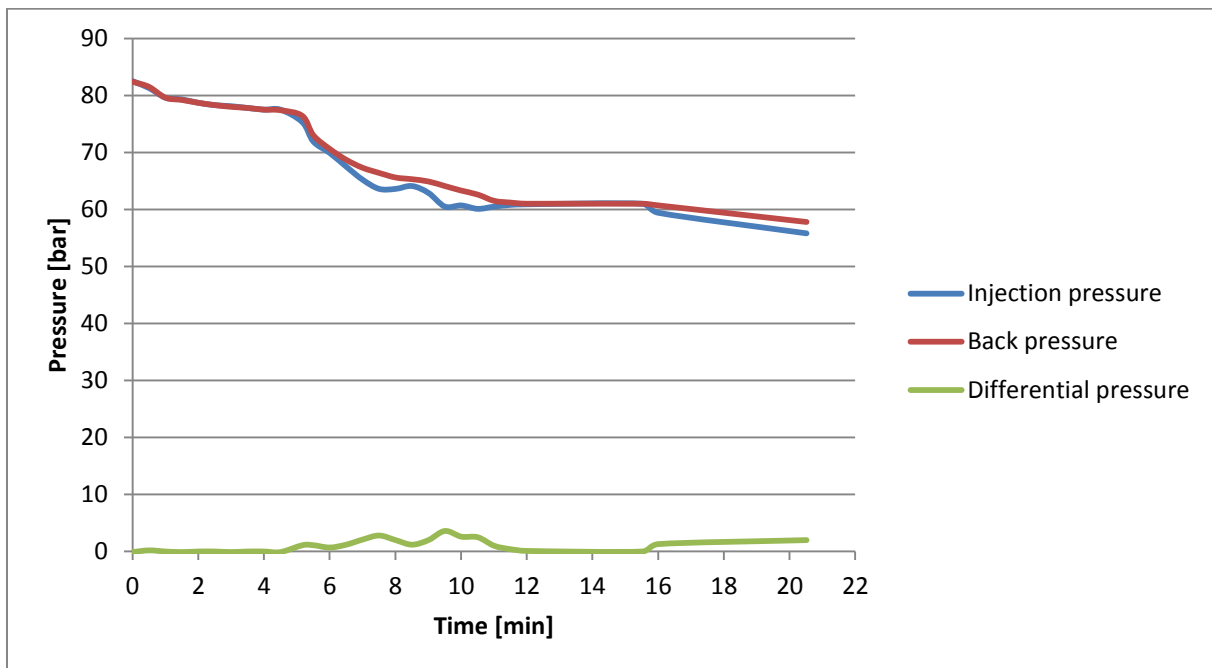


Figure 6.4.10: Pressure as a function of time during depressurization of CO₂

Images and data recording were captured in the pressure interval of 65 to 55 bars. Change of state was observed during the first ten seconds as the pressure decreased. This was captured in **Figure 6.4.11a, b & c**.

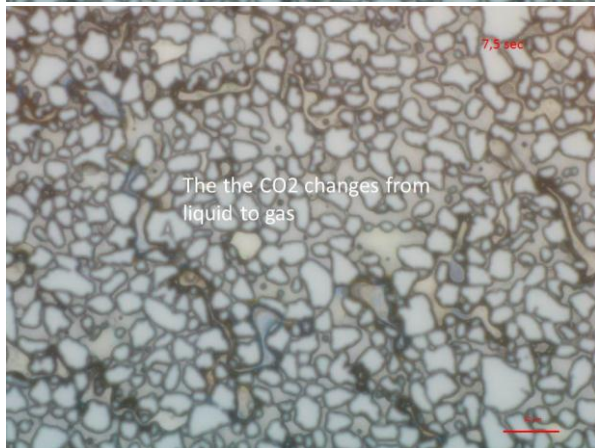
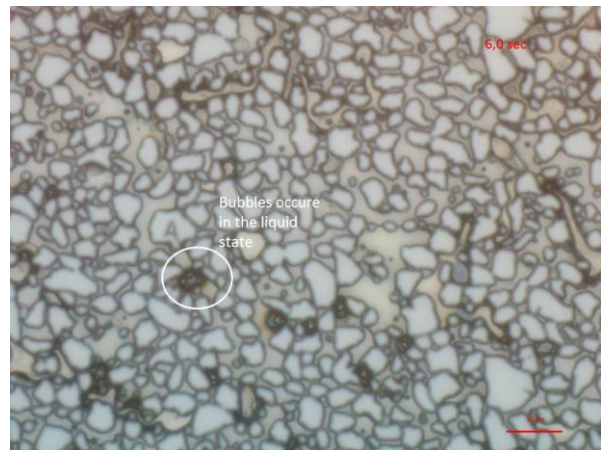
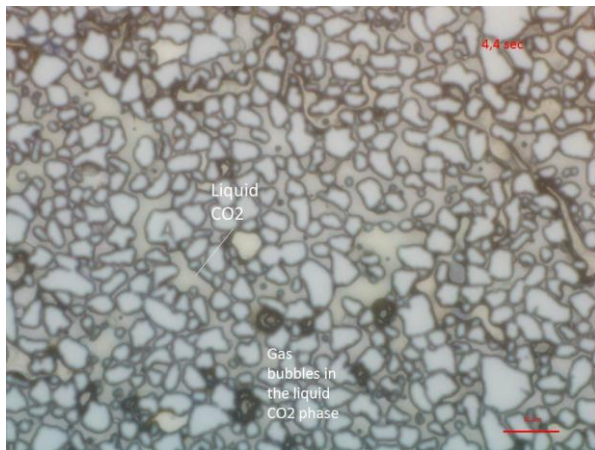


Figure 6.4.11a, b & c: CO₂ changes state from liquid to gaseous with decreasing pressure; (a) gas bubbles are observed in the liquid phase, (b) a new bubble immerge in the liquid phase, (c) the liquid phase vaporizes to gas

Several gas bubbles were observed in Figure 6.4.11A after 4.4 seconds. After 6.0 seconds a gas bubble was developed within the observed liquid CO₂ phase. Figure 6.4.11c displays the observed liquid CO₂ phase vaporizing into gas after 7.3 seconds. While the vaporization process was immediate when the pressure was in the range of 62-61 bars, it took time for gas expansion from swelled oil to be observed. After 2min and 18sec gas expansion was observed and captured.

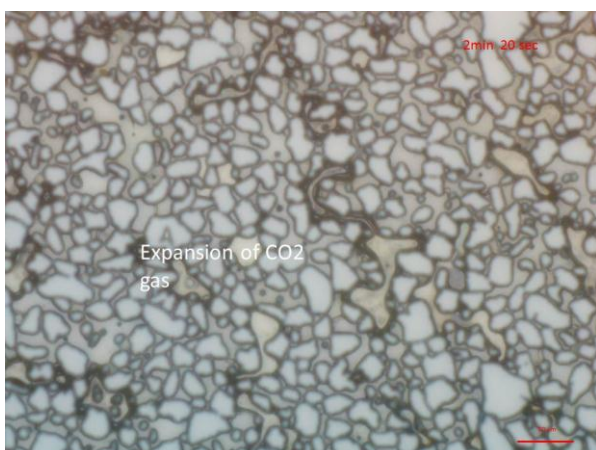
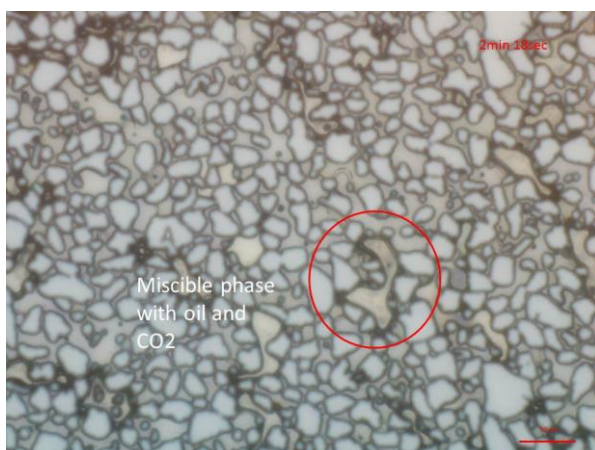


Figure 6.4.12a & b: Gas expansion from miscible phase: (a) a miscible phase with CO₂ and oil is marked, (b) CO₂ gas expands from the miscible phase

From **Figure 6.4.12a** a miscible phase consisting of oil and liquid CO₂ was observed. The phase was identified by the black borders and was confirmed to be in the oil phase by reflecting red light under the green filter. As the pressure decreased towards and below 60 bars, the volume of the red circled, miscible phase increased. Gas expansion was then observed as gas flowed from the miscible phase, which was captured in **Figure 6.4.12b**. CO₂ gas expansion continued as the pressure decreased, and flow of gas was observed throughout the micromodel.

Discussion Solution Gas Drive during Depressurization of CO₂

From the phase diagram in Figure 2.4 a sufficient decrease in pressure of liquid CO₂ will result in change of state from liquid to gaseous. The change of state at 23 °C was calculated to be approximately 61.4 bars[29]. Vaporization was observed as the liquid CO₂ changed into gas. As the CO₂ changed state the viscosity was decreased, resulting in an increase in CO₂ mobility (equation 1.7.1) and the gas was therefore observed to flow rapidly. This was caused by an uneven mobility ratio as a result of the increase in viscous forces. The gas flowed rapidly towards the fracture and production port, displacing oil on its way. The capillary number was increased as the viscous forces became more controlling (equation 1.4.3), contributing to a lower oil saturation (Figure 1.4.3).

Gas expansion was observed after 2 minutes and 20 seconds (Figure 6.4.12b). Gas expanded from the miscible phase of oil and CO₂ as the pressure was decreased below 61.4 bars. The volume of the oil shrunk as gas was released, and the volume of CO₂ was increased. The expanded gas was observed to flow in the same manner as the vaporized gas, displacing oil through solution gas drive[45]. Displacement of oil, leading to an increase in oil recovery was observed during the solution gas drive experiment. The oil recovery was calculated after the solution gas drive to be 82% ± 5%. The exact increase in oil recovery could not be calculated, as the recovery after the miscible, liquid CO₂ injection was not calculated. The increase in oil recovery was assumed to be low for the solution gas drive, due to an already high recovery from the liquid CO₂ injection.

6.5 Experimental Challenges

Delicate Equipment

After the water injection experiment for the high pressure micromodel B1, the experimental setup was altered and prepared for high pressure CO₂ injection. The system was pressurized slowly and a leakage in the injection port was discovered using *Snoop*® *Liquid Leak Detector*. Snoop is a chemical solution that bubbles in contact with CO₂. The solution was used to check for leakage throughout the experiments with CO₂. Fixing the leakage required investigation of the ferule on the injection port. The ferule was changed and the experimental setup was reassembled. Another leakage occurred when pressure testing was resumed. When fixing this leakage the ferule was tightened with extensive force. This caused the micromodel to crack when pressure was applied to the system. The cracking rendered the model useless for the next experiment, and saturation, primary drainage and initial calculations had to be performed on a new micromodel. During an initial primary drainage experiment on the low pressure micromodel Berea A, the pressure exceeded 2 bars, causing the model to crack. These experiences magnified the importance of precision when working with fragile equipment in the laboratory.

Failed Secondary Liquid CO₂ Injection Model B3

The high pressure micromodel B3 was used for this experiment, after being saturated with water and exposed to primary drainage towards the irreducible water saturation. The irreducible water saturation was calculated to be $S_{iw} = 0.08 \pm 0.05$. The injection port was connected to cylinder A of the Quizix pump system, and the producer was connected to cylinder B. Each cylinder had two valves; one fill valve and one deliver valve. Injecting CO₂ through both cylinders enabled us to build up pressure with gaseous CO₂ on both the injection and producing end of a closed system. The connected CO₂ tank gradually applied pressure to the system until a pressure of 50 bars was reached. The system was then closed off for approximately four hours so the injected CO₂ could reach thermal equilibrium. The pressure build-up was resumed after the four hours. Cylinder B injected CO₂ gas, causing the pressure to rise. The selected setup enabled pressure to be built up equally on both sides without much gas entering the model. The pressure building process was monitored through the Quizix software on the computer, and **Figure 6.5.1** is a graph displaying pressure as a function of time. The orange graph is the pressure measured at the inlet side (cylinder A), and the blue graph represents the measured pressure at the outlet side (cylinder B). The difference in pressure during the thermal equilibrium process was caused by the pressure transducers of the cylinders being calibrated differently.

After five hours the injection with cylinder B was initiated. The pressure fall of the blue graph represent the time interval where the piston in cylinder B was retracted and refilled. When the pressure reached the interval of 59 to 60 bars, the model started emitting vapour and a loud cracking-like sound was heard. The pressure fell rapidly on the injection side of the system, as can be observed from the graph. Cylinder B was closed to prevent further high pressure gas leakages. After decreasing the pressure in cylinder B gradually, the setup was disconnected. A large crack, originating from the injection port, was observed on the model.

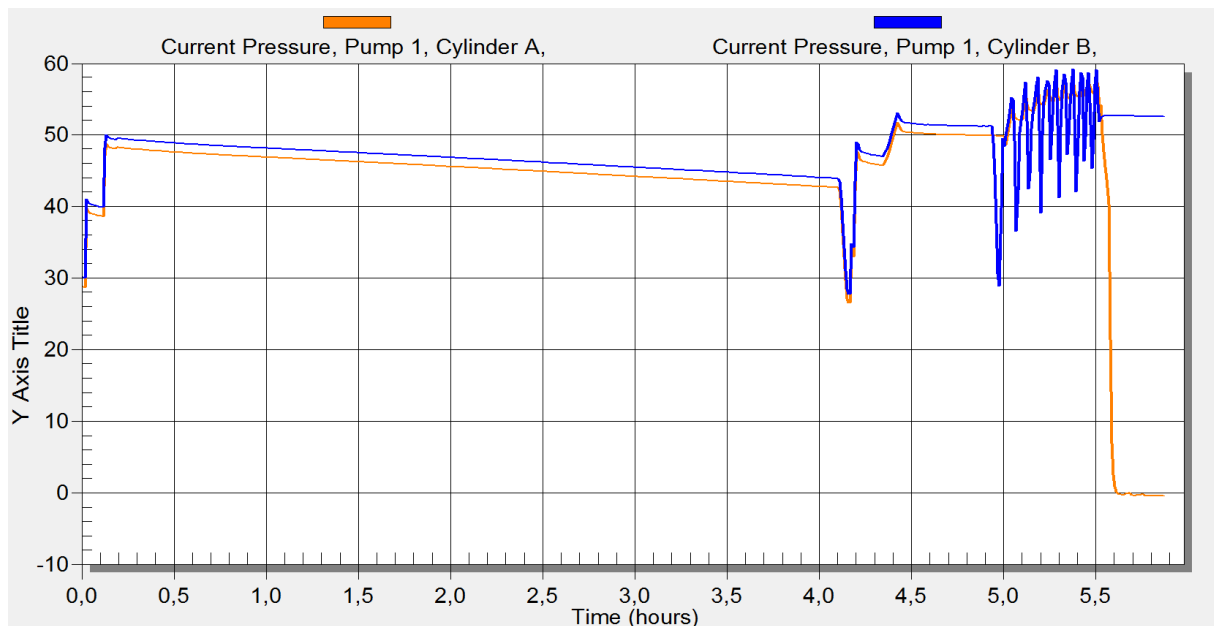


Figure 6.5.1: Graph of pressure build-up during failed secondary liquid CO₂ experiment; Pressure (y-axis) as a function of time during secondary liquid CO₂ injection (screenshot from PumpWorks)

Discussion Failed Liquid CO₂ Injection Model B3

This was the second high pressure silicon wafer model to crack, and while the first model was a “victim of human error”, the cracking of the second model was initially presumed to be a manufacturing error. Model B1 was pressure tested with CO₂ up to 90 bars, before the fundamental experiments with the high pressure silicon wafer models were initiated. The specification provided by the manufacture listed a pressure limitation of 100 bars. Successful pressure test result was later provided from model B5-fractured, and manufacturing error was ruled out as the most likely cause of destruction. A know problem with CO₂ in the petroleum industry is corrosion. In a relative slow reaction, CO₂ can hydrate in water and become a corrosive carbonic acid[46]. Corrosion might have an effect on the experimental equipment, while the effect of corrosion was considered to be minor on the tubings and micromodel connections. The crack originating from the tubing connected to injection port indicated corrosion being an unlikely cause.

The experimental setup and procedure was later re-evaluated. The setup allowed pressure to be build-up from both sides, limiting the injection of CO₂ into the model. This caused the differential pressure over the model to be equal to the systems pressure. The micromodel had close to ambient pressure conditions while the differential pressure was close to 60 bars causing the model to crack. This experience forced us to alter the setup (see Figure 3.1b) and amplified the importance of limiting the differential pressure over the model.

6.6 Summarized Discussion CO₂ Injection

Comparing gaseous CO₂ flooding with liquid CO₂ flooding was one of the main objectives of this thesis. From the phase diagram (Figure 2.4) the different states are presented as functions of temperature and pressure. The experiments were conducted at a constant temperature of $23.0^{\circ}\text{C} \pm 0.5^{\circ}\text{C}$. Changing the state from gaseous to liquid therefore required an increase in pressure. Liquid CO₂ was obtained when the pressure was increased to above $61.4 \text{ bars} \pm 0.5 \text{ bar}$. Liquid CO₂ has a higher density and viscosity than gaseous CO₂, as can be seen from Figure 6.6.1.

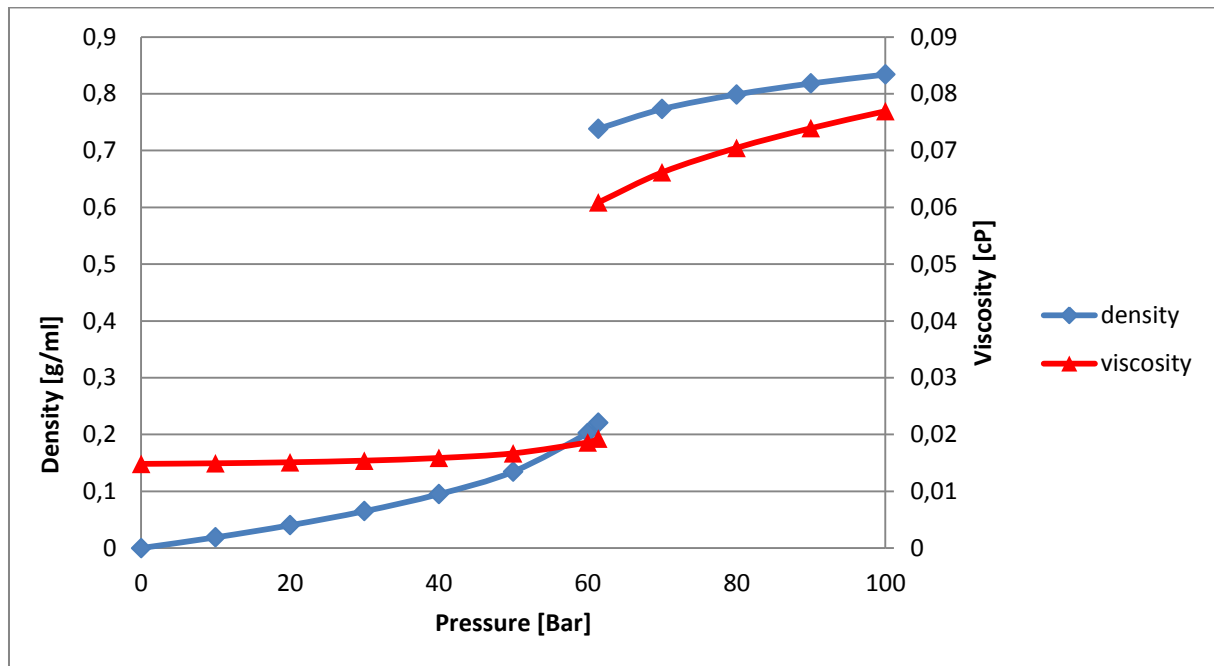


Figure 6.6.1: CO₂ density and viscosity as a function of pressure[29]: the low values to the left are for gaseous CO₂, while the increased values to the right are for liquid CO₂

During CO₂ gas injection snap-off events, piston displacement, film flow and multiple displacement were observed at the pore scale. The same displacement mechanisms were observed during liquid CO₂ injection, except snap-off events that were only observed during CO₂ gas injection. The flow was observed to be stable and controlled by capillary forces at low injection rates for the low pressure silicon wafer micromodel, while the increase in injection rate resulted in a more unstable flow controlled by increasing viscous forces. CO₂ usually flow straight through fractures and high permeability zones, but the effect of diffusion made CO₂ in the fracture enter the matrix. The oil recovery was increased and most of the pores were swept given sufficient time and injected volume. The same unstable flow conditions were observed for the liquid CO₂ injection. Viscous fingering were observed, however the effect of viscous forces where consider to be less due to more favourable mobility ratios for the liquid CO₂. Diffusion of CO₂ from the fracture and channels provided an efficient sweep in the high pressure silicon wafer micromodels. The injections provided relatively similar observations and results, before miscibility was achieved.

Miscibility during liquid CO₂ injection was observed at 82.0 bars ± 0.5 bar pressure, while the gaseous CO₂ injection was immiscible with oil in the applied pressure range. When two fluids are immiscible there exist an interfacial tension between them caused by capillary pressure effects[47]. Immiscible CO₂ injection increases oil recovery by raising the capillary number due to the low interfacial tension between CO₂ and oil[48]. Miscible CO₂ flooding reduces the interfacial tension between oil and CO₂ to zero, resulting in an infinite capillary number. The CO₂ causes the oil to swell and expand. The dissolution of CO₂ in oil (swelling) reduces the oils viscosity[49] and can increase the oil volume 10-50%[50]. The mobility ratio is improved and a better sweep efficiency can be achieved[20]. From **Figure 6.6.2** miscibility between oil and CO₂ is illustrated.

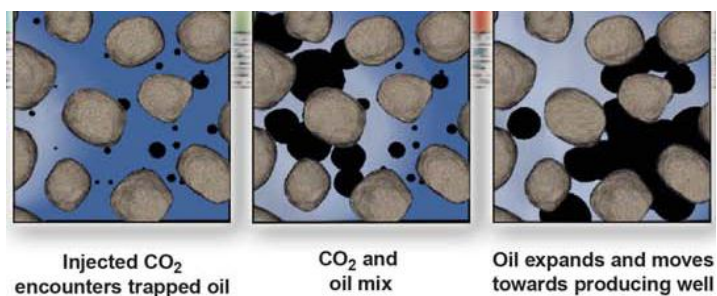


Figure 6.6.2: Miscibility between oil and CO₂[51], injected CO₂ mixes with oil, swelling the trapped oil and mobilizing the oil towards the production well

The experiments with miscible CO₂ were also influenced by diffusive process due to the fracture and channels. Viscous fingering was still observed as liquid CO₂ displaced oil, while the miscible displacement appeared more stable. The miscible phase displaced oil through piston-like events and multiple displacements. The first contact miscibility mobilized previously trapped oil, and increased the swept area. Diffusive process was considered to be the main source of mobilizations, as increased pressure increases the diffusion[5]. Closes to complete recovery is possible given sufficient time and injected CO₂ volume. The injection pressure was reduced so the effect of vaporization and solution gas drive could be observed. The viscous forces increased as the liquid CO₂ vaporized into gas. The recovery increased as the vaporized gas displaced oil and the previously swelled oil reduced its volume. The flow and features for the different experiments with CO₂ are summarized in table 6.6.1.

Table 6.6.1: Summary of experiments with CO₂ injection

Displacement process	Model	Flow conditions	Flow regime	Characteristic features
Secondary CO ₂ gas injection	Berea D	Low flow rate and low Δp	Mostly stable with occasionally capillary fingering	Film flow dominating Good sweep Low production rate
Secondary CO ₂ gas injection	B5-fracture	High flow rate and low Δp	Unstable capillary and viscous fingering	Diffusion dominating =>improved sweep. High initial production rate
Immiscible liquid CO ₂ injection	-	High flow rate and high Δp	Partially stable with viscous fingering	Diffusion and film flow Improved mobility=>good sweep Low production rate
Miscible liquid CO ₂ injection	-	High flow rate and low Δp	Mostly stable with occasionally viscous fingering	Miscibility, swelling, diffusion => good sweep Fluids mobilized Improved recovery
Solution CO ₂ gas drive	-	High flow rate and high Δp	Unstable viscous fingering	Poor sweep Minor increase in recovery

The recovery values for the different experiments are summarized in table 6.6.2. The low pressure silicon wafer micromodels are represented by *LPMm*, while the high pressure micromodels are represented by *HPMm*. The S_{or} -column gives the respective residual oil saturation, and the recoveries are given as percentage of the original oil in place (*OOIP*). Production of oil stopped after water breakthrough for the low pressure micromodel, while the production after water breakthrough continued at a reduced rate for the high pressure micromodel. The star (*) indicates that increased recovery is expected given sufficient time and injection volume. Because observing and comparing flow and displacement mechanisms were the main objectives, optimizing the recovery was not prioritized. All the saturation and recovery values have an uncertainty of $\pm 5\%$ while residual oil saturations have an uncertainty of ± 0.05 , which is discussed in the appendix.

Table 6.6.2: Summary of residual oil saturation and recovery

Process	Model	S_{or}	Recovery [%]
Secondary water injection	LPMm - Berea G	0.84	5 %
-	HPMm - B1	0.73	21 %
Three-phase CO ₂ gas injection	LPMm - Berea D	0.24	*73 %
-	HPMm - B5-fracture	0.32	*63 %
Three-phase liquid CO ₂ injection	HPMm - B5-fracture	0.15	*82 %

IV. Conclusions and Future Work

7. Conclusions

The following conclusions were made after spontaneous imbibition, primary drainage, secondary water injection, three-phase gaseous CO₂ injection and three-phase liquid CO₂ injection in silicon wafer micromodels:

General Conclusions

- Experimental setups were built where flow and displacement could be visualized at the pore scale for fluid and gas in both low and high pressure silicon wafer micromodels.
- By using an inverted microscope with a variety of light filters and adding Fluorescent additives to the fluids, the fluids were distinguished and visualized.
- Images were captured on the computer, where image software enabled porosity, saturations and recovery to be estimated.
- The micromodels were manufactured with real reservoir rock properties, which enabled 2D visualization of pore scale displacement similar to real reservoirs.
- Controlling the injection rate and pressure enabled a variety of displacement mechanisms and flow to be studied.
- The specifications of the high pressure micromodels enabled sufficient pressure conditions for phase change and miscibility to be obtained for CO₂.
- Immiscible liquid and gaseous CO₂ injection was studied and compared to liquid first contact miscible CO₂.

Spontaneous Imbibition

- Stable and unstable flow regimes were observed during water imbibition in the low pressure silicon wafer micromodels.
- The stable flow advanced slowly and provided a good sweep, while the unstable flow was observed through capillary fingering events resulting in a poor sweep efficiency.
- The stability of the flow was controlled by the injection rate and the differential pressure. Stable flow was achieved at low rates and pressure, while unstable capillary fingers advanced with increased pressure and injection rate.
- Dissolution of CO₂ in the water phase, end-effects, capillary fingering and counter current displacement were observed during the water imbibition experiments.

Primary Drainage

- Both stable and unstable flows were observed during primary drainage experiments.
- Stable flow was observed at high injection rates and significant differential pressure, resulting in a good sweep and saturations close to the irreducible water saturation could be achieved.
- Unstable flow regimes occurred at low rates causing capillary fingers to advance rapidly, resulting in early breakthrough and a poor sweep.
- Film flow, double displacement and both stable and unstable (Haines' jump) piston displacements were observed during the primary drainage experiments.

Three-phase CO₂ Gas Injection

- Spreading layers of oil were observed during three-phase CO₂ gas injection, and prevented the CO₂ to contact the water phase.
- The CO₂ displaced the water through multiple displacement mechanisms, while oil was displaced through piston displacements and snap-off event followed by expansion of the gas.
- CO₂ preferably displaced oil in large pores through bulk flow towards the production channels, while the spreading layers of oil were produced slowly through film flow.
- Diffusive process caused the CO₂ to flow through different paths in pore network, thereby mobilizing more residual oil and improving the sweep efficiency.

Three-phase Liquid CO₂ Injection

- Gaseous CO₂ was observed to change into liquid state when the pressure was increased to 61.4 bars \pm 0.5 bar.
- Mostly stable flow regimes were observed as the liquid CO₂ displaced oil through piston and multiple displacements, while spreading layers of oil and water films were displaced through film flow. The increased viscosity of the CO₂ improved the mobility and reduced the effect of viscous forces.
- The fracture in the model lead to diffusion being controlling, and residual fluids were mobilized thereby contributing to a good sweep.
- Miscibility between oil and liquid CO₂ were observed when the pressure was increased to 82.0 bars \pm 0.5 bar. Oil swelling and miscible displacement was observed. The oil swelling reduced the oils viscosity and made the oil more mobile, contributing to an increased recovery.
- Mostly stable flow and mobilization of fluids were observed under miscible conditions.
- Vaporization of CO₂ was observed as the pressure was reduced. The vaporizations caused the volume of CO₂ to expand and advance through viscous fingers. CO₂ gas expanded from the miscible phase and the swelled oil, displacing oil through solution gas drive.

8. Future Works

In this thesis displacement, flow and selected properties of CO₂ is studied on the pore scale by using both low pressure and high pressure silicon wafer micromodels. Fundamental displacement mechanisms are investigated for spontaneous imbibition, primary drainage and CO₂ injection, both liquid and gaseous. The experiments are conducted on micromodels based on the structures of Berea sandstone. The microfluidic laboratory at the Department of Physics and Technology at University of Bergen was opened a few months before the experimental work in this thesis were initiated, and has been under constant development since. Further experiments and investigation using the Berea sandstone micromodels are required, including:

- Development of an experimental setup that allows secondary injection of liquid CO₂ to be investigated.
- Acquiring accurate data for estimating parameters like capillary number, mobility ratios and relative permeability.
- Up scaling both current and future results to be applied in numeric simulations and investigations of core samples.
- Replace n-decane with oils with different oil composition, relevant for future and current production on the Norwegian Continental Shelf.
- Develop a technology that allows different thermal conditions to be investigated. This will enable investigation of flow at reservoir conditions and allow CO₂ at a supercritical level to be studied.
- Investigate different methods of enhanced oil recovery including; water alternate gas (WAG), foam injection, solvents and polymers.

The suggestions above are for the current water-wet, high pressure, silicon wafer, Berea sandstone micromodels. The opportunities for further experimental work are great, and in the future development of new micromodels will expand the field of study. New micromodels can be manufactured and modelled after different reservoir rocks, from chalk to limestone. Reservoir parameters can be varied by constructing models with different wettability, from water-wet to oil-wet. High definition images of thin-sections of reservoir rocks will enable the construction of accurate and complex models. The development of technology and further experimental work will enable us to visually study displacement, flow and the effect of various reservoir parameters, for most types of reservoir rock on the pore scale.

9. Notations

EOR = Enhanced Oil Recovery

NCS = Norwegian Continental Shelf

STOIIP = Stock-Tank Oil Initially In Place

MMP = Minimum Miscibility Pressure

g = Gas

o = Oil

w = Water

V_b = Total volume of porous rock

V_p = Pore volume of porous rock

ϕ = Porosity

p = Pressure

p_i = Phase pressure of fluid i

p_c = Capillary pressure

Δp = Differential pressure

S_i = Saturation of fluid i

S_{wi} = Irreducible water saturation

S_{or} = Residual oil saturation

θ = Wetting angle

μ = Viscosity

v = Fluid velocity

σ = Interfacial tension

q = Fluid flow rate

A = Cross sectional area

L = Length

r = Radius

k_{eff} = Effective permeability

k_r = Relative permeability

K = Absolute permeability

V = Volume

λ = Mobility

M = Mobility ratio

Nc = Capillary number

I = Amott-Harvey wettability index

W = USBM wettability index

N_p = Produced oil volumes

N = Total oil reserves

E_R = Recovery factor

REV = Representative elementary volume

10. References

1. Fenwick, D.H. and M.J. Blunt, *Three-dimensional modeling of three phase imbibition and drainage*. 1998.
2. Lenormand, R., C. Zaccaro, and A. Sarr, *Mechanisms of displacement of one fluid by another in a network of capillary ducts*. 1983.
3. Blunt, M.J., *Effects of heterogeneity and wetting on relative permeability using pore level modeling*. 1997.
4. Skjærveland, S.M. and J. Kleppe, *SPOR - Recent Advances in Improved Oil Recovery Methods For North Sea Sandstone Reservoirs*. 1992.
5. Renner, T.A., *Measurement and Correlation of Diffusion Coefficients for CO₂ and Rich-Gas Applications*. 1988.
6. Murray, J. and D. King, *Climate policy: Oil's tipping point has passed, in nature - International weekly journal of science* 2012.
7. Mathiassen, O.M., *CO₂ as Injection Gas for Enhanced Oil Recovery and Estimation of the Potential on the Norwegian Continental Shelf*. 2003.
8. Selly, R.C., *Elements of Petroleum Geology*. 1998.
9. Lien, J.R., *Reservoarteknikk I*. 2007.
10. Zolothukhin, A.B. and J.R. Ursin, *Introduction to petroleum reservoir engineering*. 2000.
11. *Capillary Pressure Curve*. Available from:
<http://www2.ggl.ulaval.ca/personnel/paglover/CD%20Contents/Formation%20Evaluation%20English/Chapter%208.PDF>.
12. Brown, K.I., M.L. Porter, and D. Wildenschild, *Comparing Pore-scale and Macro-scale Capillary Pressure Measurements Using a Two-dimensional Micromodel*. 2007.
13. Lake, L.W., *Enhanced Oil Recovery*. 1989.
14. Melrose, J.C., *Wettability as Related to Capillary Action in Porous Media*. 1965.
15. Morrow, N.R., *Physics and thermodynamics of capillary actions in porous media*. 1970.
16. Lien, J.R., *PTEK211 - Grunnleggende reservoar fysikk (kjerneanalyse og logging)*. 2004.
17. Anderson, W.G., *Wettability Literature Survey - Part 1: Rock/Oil/Brine Interactions and the Effect of Core Handling on Wettability*. 1986.
18. Donaldson, E.C., R.D. Thomas, and P.B. Lorenz, *Wettability Determination and Its Effect on Recovery Efficiency*. 1969.
19. Amotte, E., *Observations Relating to the Wettability of Porous Rock*. 1959.
20. Skarestad, M. and A. Skauge, *Reservoarteknikk II, PTEK 213*. 2009.
21. Craig, F.F., *The reservoir engineering aspects of waterflooding*. 1971.
22. Bear, J., *Dynamics of Fluids in Porous Media*. 1988.
23. Torvund, T. and O. Nipen, *The Oseberg Field; Potential for Increased Oil Recovery by Gas Injection in a High Permeability Environment, in North Sea Oil and Gas Reservoirs Seminars 1*. 1987, Graham & Trotman: London. p. 61-74.
24. Klins, M.A., *Carbon Dioxide Flooding*. 1984.
25. Schlumberger. *Oilfield Glossary - MMP*. Available from:
<http://www.glossary.oilfield.slb.com/Display.cfm?Term=minimum%20miscibility%20pressure>.
26. Al-Marri, S.S., *SPE 126078: Minimum Miscibility Pressure Determination for Systems Carbon Dioxide + Heavy Hydrocarbon (N-Eicosane) + Light Gas (Ethane or Propane) Using Peng-Robinson Equation of State*. 2009.
27. Picha, M.S., *SPE 105425: Enhanced Oil Recovery by Hot CO₂ Flooding*. 2007.
28. Follesø, H.N., *Fluid Displacements during Multiphase Flow Visualized at the Pore Scale using Micromodels*. 2012.
29. *Thermophysical Properties of Fluid Systems*. Available from:
<http://webbook.nist.gov/chemistry/fluid/>.

30. *Micronite Chip Holder*. Available from: <http://www.micronit.com/research-products/microfluidic-products/chip-holders/>.
31. *Quizix SP-5200 pump system* Available from: <http://vindum.com/wp/wp-content/uploads/Q-SP5000-Manual031306.pdf>.
32. *Nikon*. Available from: http://www.nis-elements.com/pdfs/Digital_Sight_Series.pdf. .
33. Kenneth, G.R., *Fluorescein. Physicochemical factors affecting its fluorescence. Survey of Ophthalmology*. 1982.
34. Fowler, S.D., *Spectrofluorometric studies of the lipid probe, Nile red*. 1985.
35. Hornbrook, J.W., L.M. Castanier, and P.A. Pettit, *Observation of Foam/Oil Interactions in a New, High-Resolution Micromodel*. 1991.
36. *Micronite Microchip*. Available from: <http://www.micronit.com/assets/Downloads/Research-Products.pdf>.
37. Hadley, G.F. and L.L. Handy, *A Theoretical and Experimental Study of the Steady State Capillary End Effect*. 1956.
38. Lenormand, R., *Liquids in porous media*. 1990.
39. Thomas, L.K., *Threshold Pressure Phenomena in Porous Media*. 1968.
40. *Ideal gas law*. Available from: http://chemwiki.ucdavis.edu/Physical_Chemistry/Physical_Properties_of_Matter/Gases/The_Ideal_Gas_Law.
41. *Definition Diffusion*. 2011; Available from: <http://www.mn.uio.no/bio/tjenester/kunnskap/plantefys/leksikon/d/diffusjon.html>.
42. WILCOCK, R.J., et al., *Solubilities of gases in liquids II. The solubilities of He, Ne, Ar, Kr, O₂, N₂, CO, CO₂, CH₄, CF₄, and SF₆ in n-octane 1-octanol, n-decane, and 1-decanol*. 1978.
43. Hughes, R.G. and M.J. Blunt, *Pore-Scale Modeling of Multiphase Flow in Fractures and Matrix/Fracture Transfer*. 2001.
44. Elsharkawy, A.M., F.H. Poettmann, and R.L. Christiansen, *Measuring Minimum Miscibility Pressure: Slim-Tube or Rising-Bubble Method?* 1992.
45. *Solution gas drive*. Available from: <http://www.oilfield-dictionary.com/solution-gas-drive-reservoirs/>.
46. International, A., *Corrosion in the Petrochemical Industry*. 1994.
47. Al-Jarba, M., *A Comparison Study of the CO₂-Oil Physical Properties Literature Correlations Accuracy Using Visual Basic Modelling Technique*. 2009.
48. Kulkarni, M.M., *IMMISCIBLE AND MISCIBLE GAS-OIL DISPLACEMENTS IN POROUS MEDIA*. 2003.
49. Holm, L.W. and V.A. Josendel, *Mechanisms of Oil Displacement by Carbon Dioxide*. 1974.
50. Klins, M.A. and S.M. Farouq Ali, *Oil Production in Shallow Reservoirs by Carbon Dioxide Injection*. 1981.
51. UDE, N.E.T.L., *Carbon Dioxide Enhanced Oil Recovery - Untapped Domestic Energy Supply and Long Term Carbon Storage Solution*. 2010.

Appendix I – Uncertainty Estimations

There are always some uncertainties when conducting experimental work and making calculations. In this thesis most of the calculations were porosity, saturation and recovery calculations. The calculations were done by using image software and were explained in details in chapter 4. The quality and resolution of the photo will affect the accuracy when measuring the pixels. Higher quality and high resolution will give a more accurate pixel conversion. **Figure A.1a** is a binary image of the pore network for the high pressure micromodel B1. The models were manufactured with realistic, rough grains, with no closed pores. From Figure A.1a several closed pores are marked, and the grains are observed to be smoother and rounder compared to **Figure A.1b**. This will cause an error when calculating the porosity. The uncertainty was estimated to be in the range of $\pm 5\%$. The uncertainty was calculated by applying colour threshold, finding the average porosity and using the maximum and minimum value as the uncertainty. The porosities were calculated to be in the range of 50 to 52%, which is high for Berea sandstones. The high porosity values are due to the micromodels being manufactured in 2D with an optimized flow pattern, with no closed pores, and continuous flow path.

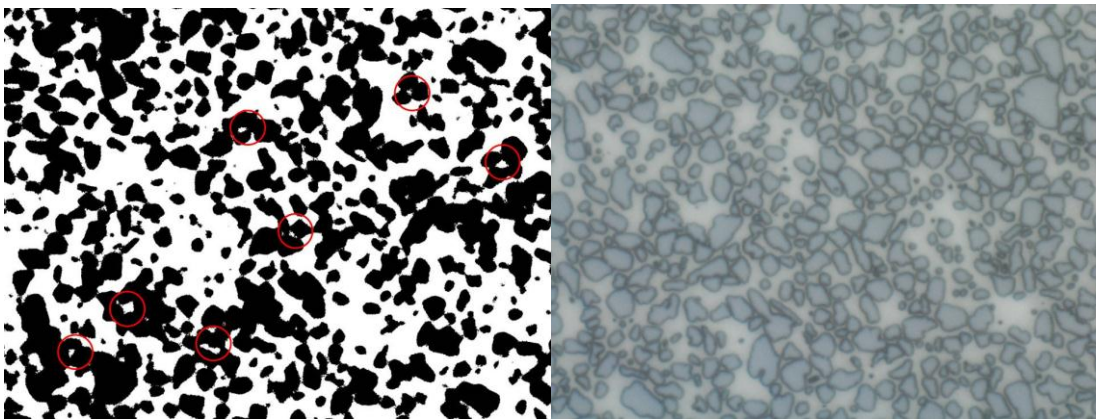


Figure A.1a & b: Binary image and image through the bright light filter of the pore network in model B1; (a) closed pores and rounded grains are observed, (b) no closed pores and rougher grains are observed

When calculating the saturation the main uncertainty will be from applying “colour threshold” to the images. When the Fluorescein is illuminated over a period time, the solution will be affected by photo bleaching. The effect of photo bleaching makes it harder to distinguish between the phases, and will make it hard to manually separate the phases. In some cases it is observed that thin films on the pore walls, is not selected when applying “colour threshold”, resulting in an inaccurate saturation calculation. From **Figure A.2** the oil phase in an image of a three-phase process is marked by applying colour threshold. Some grains and pore walls within the oil phase were marked with red, resulting in higher calculated oil saturation. Other times photo bleached oil were not marked when applying colour threshold, resulting in lower calculated oil saturation. The uncertainty was calculated by dividing the difference between the high and low saturation values by two, resulting in an estimated uncertainty of approximately $\pm 5\%$.

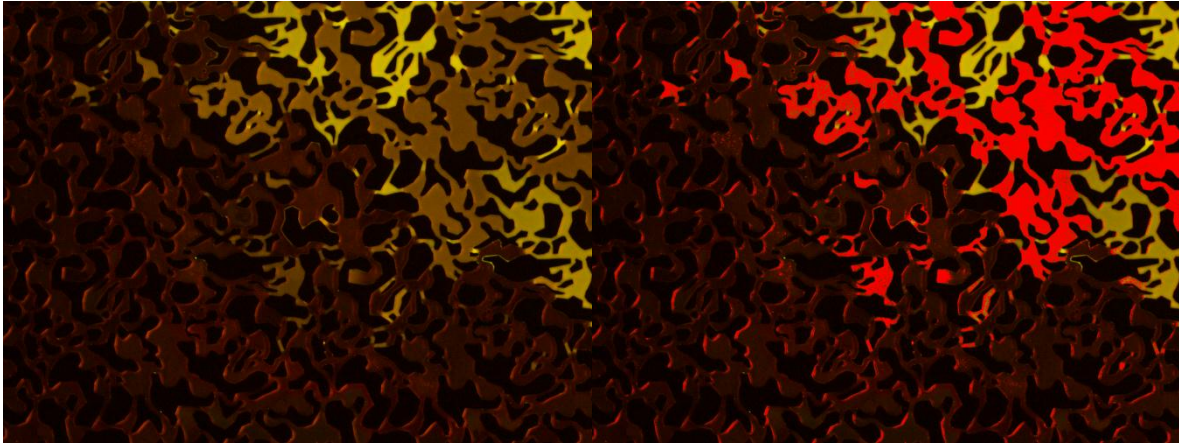


Figure A.2: Oil phase marked by colour threshold in an image of three-phase flow

The uncertainty for the permeability values were estimated in a similar manner, by dividing the difference between the highest and lowest calculated value by two. The uncertainties were relatively similar for all the micromodels and were estimated to be approximately $\pm 50\text{mD} = 0.05\text{D}$.

In addition there were some uncertainty in the pressure and temperature, which were in the range of ± 0.5 bar and ± 0.5 °C.

